NAVAL POSTGRADUATE SCHOOL

MONTEREY, CALIFORNIA

DISSERTATION

AEROSOL OPTICAL DEPTH RETRIEVALS FROM HIGH-RESOLUTION COMMERCIAL SATELLITE IMAGERY OVER AREAS OF HIGH SURFACE REFLECTANCE

by

Dominick A. Vincent

June 2006

Dissertation Supervisor: P. A. Durkee

Approved for public release; distribution is unlimited.

THIS PAGE INTENTIONALLY LEFT BLANK

REPORT DOCUMENTATION PAGE	*Form Approved OMB No. 0704-0188*

1. AGENCY USE ONLY (*Leave blank*)	2. REPORT DATE June 2006	3. REPORT TYPE AND DATES COVERED Dissertation	
4. TITLE AND SUBTITLE: Aerosol Optical Depth Retrievals from High-Resolution Commercial Imagery Over Areas of High Surface Reflectance			**5. FUNDING NUMBERS**
6. AUTHOR(S)			
7. PERFORMING ORGANIZATION NAME(S) AND ADDRESS(ES) Naval Postgraduate School Monterey, CA 93943-5000			**8. PERFORMING ORGANIZATION REPORT NUMBER**
9. SPONSORING / MONITORING AGENCY NAME(S) AND ADDRESS(ES) N/A			**10. SPONSORING / MONITORING AGENCY REPORT NUMBER**
11. SUPPLEMENTARY NOTES The views expressed in this thesis are those of the author and do not reflect the official policy or position of the Department of Defense or the U.S. Government.			
12a. DISTRIBUTION / AVAILABILITY STATEMENT Approved for public release; distribution is unlimited.			**12b. DISTRIBUTION CODE**

13. ABSTRACT (*maximum 200 words*)

The advancement and proliferation of high-resolution commercial imaging satellites presents a new opportunity for overland aerosol characterization. Current aerosol optical depth retrieval methods typically fail over areas with high surface reflectance, such as urban areas and deserts, since the upwelling radiance due to scattering by aerosols is small compared to the radiance resulting from surface reflection. The method proposed here uses shadows cast on the surface to exploit the differences between radiance from the adjacent shaded and unshaded areas of the scene. Given uniform surface reflectance for the shaded and unshaded areas, the difference in reflected radiance measured by a satellite sensor is related to the direct transmission of solar radiation and inversely proportional to total optical depth. Using an iterative approach, surface reflectance and mean aerosol reflectance can be partitioned to refine the retrieved total optical depth and, ultimately, determine the aerosol optical depth. Initial results based on QuickBird imagery and AERONET data collected during the UAE^2 campaign, as well as archive imagery and AERONET data for four other cities, indicate that aerosol optical depth retrievals are possible in the visible and near-infrared region with an uncertainty of ±0.04 for areas with surface reflectance values of 0.15 (15%) or greater.

14. SUBJECT TERMS			15. NUMBER OF PAGES
Aerosol, Satellite Observations, Aerosol Optical Depth Retrieval, Over Land, Shadow, High-Resolution Commercial Satellite Imagery, QuickBird, Desert, Urban, Grass, High Surface Reflectance			197
			16. PRICE CODE

17. SECURITY CLASSIFICATION OF REPORT Unclassified	18. SECURITY CLASSIFICATION OF THIS PAGE Unclassified	19. SECURITY CLASSIFICATION OF ABSTRACT Unclassified	20. LIMITATION OF ABSTRACT UL

NSN 7540-01-280-5500

Standard Form 298 (Rev. 2-89)
Prescribed by ANSI Std. 239-18

i

THIS PAGE INTENTIONALLY LEFT BLANK

AEROSOL OPTICAL DEPTH RETRIEVALS FROM HIGH-RESOLUTION COMMERCIAL SATELLITE IMAGERY OVER AREAS OF HIGH SURFACE REFLECTANCE

Dominick A. Vincent
Lieutenant Commander, United States Navy
B.S., Texas A&M University, 1994
M.S., Naval Postgraduate School, 2003

Submitted in partial fulfillment of the
requirements for the degree of

DOCTOR OF PHILOSOPHY IN METEOROLOGY

from the

NAVAL POSTGRADUATE SCHOOL
June 2006

Author: _____
                            Dominick A. Vincent

Approved by:

_____   _____
Philip A. Durkee   Carlyle H. Wash
Professor of Meteorology   Professor of Meteorology
Dissertation Supervisor/
Committee Chair

_____   _____
Kenneth Davidson   Richard C. Olsen
Professor of Meteorology   Professor of Physics

_____
Jeffery S. Reid
Naval Research Lab, Monterey, CA

Approved by: _____
                             Philip A. Durkee, Chair, Department of Meteorology

Approved by: _____
                             Julie Filizetti, Associate Provost for Academic Affairs

THIS PAGE INTENTIONALLY LEFT BLANK

ABSTRACT

The advancement and proliferation of high-resolution commercial imaging satellites presents a new opportunity for overland aerosol characterization. Current aerosol optical depth retrieval methods typically fail over areas with high surface reflectance, such as urban areas and deserts, since the upwelling radiance due to scattering by aerosols is small compared to the radiance resulting from surface reflection. The method proposed here exploits the difference between radiances from the adjacent shaded and unshaded areas of a scene. Shaded areas of the scene are primarily illuminated by diffuse irradiance that is scattered downward from the atmosphere, while unshaded areas are illuminated by both diffuse and direct solar irradiance. The first-order difference between the shaded and unshaded areas is the direct solar component. Given uniform surface reflectance for the shaded and unshaded areas, the difference in reflected radiance measured by a satellite sensor is related to the direct transmission of solar radiation and inversely proportional to total optical depth. Using an iterative approach, surface reflectance and mean aerosol reflectance can be partitioned to refine the retrieved total optical depth. Aerosol optical depth can then be determined from its contribution to the total atmospheric optical depth following correction for molecular Rayleigh scattering. Initial results based on QuickBird imagery and AERONET data collected during the United Arab Emirates Unified Aerosol Experiment (UAE^2), as well as archive imagery and AERONET data for four other cities, indicate that aerosol optical depth retrievals are possible in the visible and near-infrared region with an uncertainty of ±0.04 optical depth units for areas with surface reflectance values of 0.15, or 15%, and greater.

THIS PAGE INTENTIONALLY LEFT BLANK

TABLE OF CONTENTS

LIST OF FIGURES

xvi

THIS PAGE INTENTIONALLY LEFT BLANK

LIST OF TABLES

THIS PAGE INTENTIONALLY LEFT BLANK

LIST OF SYMBOLS

F_0	Spectral solar radiant flux density or irradiance
$F_{diff}^{\uparrow}$	Upward diffuse flux density or irradiance
$F_{diff}^{\downarrow}$	Downward diffuse flux density irradiance
g	Asymmetry parameter
H	Height
J	Scattering source function
L_0	Solar radiance at top of the atmosphere
L_R	Diffuse reflected radiance
L_s^r	Surface-leaving radiance reflected by the atmosphere
L_{shaded}	Radiance measured within a shaded or shadowed area
L_t	Diffuse transmitted radiance
$L_{unshaded}$	Radiance measured outside of a shaded or shadowed area
L^*	Total radiance transmitted to the ground
P	Scattering phase function
p	Atmospheric pressure
p_0	Atmospheric reference pressure
R	Reflection function
r	Reflectance
r_s	Surface reflectance
$\overline{r}$	Mean aerosol reflectance
T	Transmission function
t	Transmittance
Δ	Dirac delta
δ	Optical depth
δ_0	Optical depth of the atmosphere
δ_a	Aerosol optical depth
δ_r	Rayleigh (molecular) scattering optical
δ'	Optical depth of a discreet layer of the atmosphere
Θ	Scattering angle
λ	Wavelength
μ	Cosine of the viewing or sensor zenith angle
μ'	Cosine of the source scattering zenith angle
μ''	Cosine of the resultant scattering zenith angle
μ_0	Cosine of the solar zenith angle
ϕ	Viewing or sensor azimuth
ϕ_0	Solar azimuth
ϕ'	Source scattering azimuth
ϕ''	Resultant scattering azimuth
$\tilde{\omega}$	Single scatter albedo

THIS PAGE INTENTIONALLY LEFT BLANK

LIST OF ACRONYMS

AERONET	Aerosol Robotic Network
AOD	Aerosol optical depth
ATSR-2	Along Track Scanning Radiometer 2
CSIL	Commercial Satellite Imagery Library
ETM+	Enhanced Thematic Mapper (aboard Landsat 7)
JACIE	Joint Agency Commercial Imagery Evaluation Team
MAARCO	Mobile Atmospheric Aerosol and Radiation Characterization Observatory
MISR	Multi-angle Imaging SpectroRadiometer
MODIS	Moderate Resolution Imaging Spectroradiometer
NGA	National Geospatial Intelligence Agency
POI	Principles of Invariance
QB	QuickBird commercial satellite
TOA	Top of the atmosphere
TOD	Total optical depth

THIS PAGE INTENTIONALLY LEFT BLANK

ACKNOWLEDGMENTS

I would like to thank my Committee Chairman and friend, Prof. Philip A. Durkee, for the small sketch that spawned this work and for all of his patience and guidance during the process that converted that sketch into the following dissertation. I would like to thank my committee, Prof. Carlyle H. Wash, Prof. Ken Davidson, Prof. Chris Olsen, and Dr. Jeff Reid, for their assistance and guidance though this process. I must also include special thanks to Dr. Jeff Reid for his mentorship and assistance in navigating the world of scientific research. He never failed to ask the hard questions and never settled for anything less than the complete answer.

While the following work bears my name, it would not have been possible without the assistance from many people. Dr. Jianglong Zhang provided an unbiased sounding board throughout the research process, readily sharing wisdom beyond his years. Mr. Kurt Nielsen has provided friendship, a sympathetic ear, and technical expertise over the last five years whose value cannot be measured. I must thank Mr. Bob Creasey for his unique ability to get just the right data at just the right time. Without people like him, science would surely have ground to a halt. Finally, Ms. Annette Walker of the Naval Research Laboratory provided editorial and technical assistance with the synoptic discussion at the end of this work. Thank you one and all.

To my fellow PhD students, both past and present, I thank you for your camaraderie. CDR Dan Eleuterio helped to shepard me through the process as I began and I am eternally grateful. I have also shared the journey with LT Jodie Beattie, MAJ Bob Stenger, and CDR Tony Miller. Their friendship and unique understanding of life as a PhD student have helped to ease the journey.

I thank my family for their understanding and support. The unconditional love and patience of my wife, Gwen, my daughter, Marissa, and my son, Connor, make all things possible.

Finally, I dedicate this work to my father. Without his encouragement, I would not be where I am today. While he is no longer with us, his love lives on.

THIS PAGE INTENTIONALLY LEFT BLANK

I. INTRODUCTION

Atmospheric aerosol particles impact the Earth's energy budget through reflection and absorption of solar radiation (known as the aerosol direct effect) and modification of cloud properties (known as the aerosol indirect effect). The scattering of incoming solar radiation back to space, the direct effect, results in a net decrease in heating at the Earth's surface. The absorption of solar energy alters the atmospheric heating rate, which influences atmospheric thermodynamics and circulation. The indirect effect works to increase cloud albedo at solar wavelengths by providing additional cloud condensation nuclei that often produce more and smaller drops that subsequently result in brighter clouds. Again, this reduces heating of the atmosphere and at the Earth's surface.

When compared to the global heating caused by anthropogenic greenhouse gases, cooling due to aerosols has the potential to offset greenhouse gas warming by approximately 25 to 50% (IPCC 2001, Twomey *et al.* 1984, Charlson *et al.* 1992, Kiehl and Briegleb 1993). The effects of aerosol particles are much harder to characterize and quantify than those of greenhouse gases. Greenhouse gases have a relatively homogeneous global distribution and a lifetime of up to 100 years or more (IPCC 2001, Prather *et al.* 1996, Smith and Wigley 2000). Aerosol particles have heterogeneous spatial and temporal distributions with life spans on the order of days to weeks (IPCC 2001). Recent climate research efforts, especially using remote sensing and modeling, have focused on characterizing the effects of sources and distributions of natural and anthropogenic aerosols.

Characterization of aerosol particles is important to military operations. Aerosol particles can deter the transfer of radiance at wavelengths ranging from visible to infrared. This can result in visibility reductions that can severely impact safety of flight, electro-optical sensor effectiveness, and ground operations. The increasing reliance on electro-optical weapons for precision strike has demanded an increased ability to quantify aerosol distributions both spatially and temporally. Hostile forces often control the regions of interest to the Department of Defense preventing *in situ* environmental measurements.

Much effort has been focused on aerosol characterization using satellite observations due to the extensive area covered by satellites combined with temporal resolutions usually on the order of a day or better. Over water aerosol characterization efforts have been successful and are well documented (Brown 1997, Durkee *et al.* 2000, Kuciauskas 2002, Martin 2004, Abdou *et al.* 2005, Kahn *et al.* 2005, Remer *et al.* 2005). Product development over land has proven much more difficult due to the complexity added by the variability of the land surface characteristics (Odell and Weinman 1975, Tanre *et al.* 1981, Kaufman and Joseph 1982, Kaufman and Fraser 1984, Kaufman and Sendra 1988, Tanre *et al.* 1988, Tanre and Legrand 1991, Remer *et al.* 2005). Current satellite techniques for characterizing aerosol particles over land are highly background dependent and require stable dark bodies of water or vegetation. The Department of Defense, however, is often interested in areas where such limitations cannot be accommodated (e.g., desert, coastal, or urban regions). For this reason, alternative methods for characterizing aerosol particles over land using satellite observations must be explored.

The advancement and proliferation of commercial high-spatial resolution imaging satellites presents a new opportunity for overland aerosol characterization. Methods employing high-spatial resolution satellite imagery have been developed for aerosol optical depth retrievals to include extension of the dark object method and contrast reduction methods (Kaufman and Sendra 1988, Tanre and Legrand 1991). Many of these efforts have met with difficulty due to surface characterization issues. With increased spatial resolution, enhanced surface complexity introduces further variability into aerosol optical depth estimations. The QuickBird satellite has a maximum spatial resolution of 2.44 meters for multi-spectral imagery and 0.61 meters for panchromatic imagery (DigitalGlobe 2005a). This introduces a level of surface complexity not seen from lower-resolution sensors. However, high-spatial resolution imagery presents an opportunity to resolve individual image features, such as shadows, that contain aerosol information.

Exploiting shadows in high-resolution imagery has the potential to provide accurate aerosol information. Liou (2002) presents a principles-of-invariance method (hence forth POI) of radiative transfer that includes surface reflection. Separate photon

budgets can be further developed using the POI method for the specific case of comparing the observed radiance found within and outside of shadow regions in high-spatial resolution imagery. Taking the difference between shaded and unshaded photon budgets, one is left with the difference in observed radiance as a function of surface reflectance, mean aerosol reflectance, solar and viewing zenith angles, solar irradiance, and total optical depth. Total optical depth is unitless and provides a measure of extinction above a vertical point in the atmosphere . A retrieval of total optical depth is possible by solving this relationship if all other parameters are known or measured.

The total optical depth can be partitioned into effects from ozone, water vapor, molecular Rayleigh scattering and aerosol effects. Current commercial high-spatial resolution imagery only covers the visible and near-infrared portions of the spectrum. This portion of the spectrum is subject to little or no influence from ozone and water vapor absorption. Molecular Rayleigh scattering and absorption can be calculated for each spectral band. The remainder of the total optical depth is due to aerosol particle content. In this work, total optical depth (TOD) and aerosol optical depth (AOD) values will be shown without units. Additionally, the reflectance values will be presented in decimal form versus percentage form unless otherwise stated.

This dissertation will outline the development of the shadow-based AOD retrieval method, test the method over desert, urban and grass backgrounds, and explore potential sources of error. Chapter II will review current methods for retrieving aerosol optical depth over land and introduce the shadow method. Chapter III provides a rigorous theoretical development of the shadow method. Chapter IV provides a sensitivity analysis of the major terms of the governing equation developed for the proposed shadow AOD retrieval method. Chapter V provides an uncertainty analysis for the retrieved AOD based on uncertainty in the individual terms of the governing equation based on the uncertainties inherent in the QuickBird satellite data. Chapter VI provides an overview of the AOD retrieval methodology. Chapter VII provides and overview of the observational data used in the investigations. Chapters VIII, IX, and X provide the results from the investigations of the desert, urban, and grass backgrounds respectively.

Chapter XI discusses strengths, limitations, and prospects for the shadow-based AOD retrieval method. Chapter XII provides conclusions and recommendations for future research.

II. BACKGROUND

A. RELATED RESEARCH

Several aerosol optical depth (AOD) retrieval methods have been proposed and tested over land areas; yet none can be applied consistently to all background or aerosol types. Three basic problems exist with AOD retrieval methodologies over land surfaces: background types that saturate in key channels; surface complexity too great to characterize surface properties consistently; and a sufficient number of channels available at the right wavelengths to overcome the first two problems. Below is a brief description of three major areas of research into these problems. This list is by no means comprehensive, but does represent the most successful and accepted methods used today.

1. Contrast Reduction Methods

One of the first methods for characterizing aerosol effects over land started as an attempt to correct imagery degraded by the presence of aerosols (Odell and Weinman 1975, Tanre *et al.* 1981). Odell and Weinman (1975) used the adding method for radiative transfer to develop a relationship between the aerosol optical depth and the measured radiances from two surface objects of differing albedo. This method relied heavily on a contrast transmission function that depends on aerosol optical depth, mean surface reflectance, and sun-sensor geometry and was computed for a model aerosol distribution only. This method can become computationally very expensive in the presence of a complex aerosol regime. Tanre *et al.* (1981) initially characterized background influence on the space-based ground reflectance measurements by partitioning the signal between the target pixels and the background pixels using a single scatter approximation and deriving a simple correction algorithm.

Kaufman and Joseph (1982) extended the contrast reduction method with an automated procedure to calculate atmospheric extinction characteristics in visible satellite imagery that contained a step-like discontinuity in surface albedo. This approach proved useful for "two-halves" fields where the image could be divided into two markedly

different albedo values and it worked well for high-spatial resolution imagery (e.g. Landsat ~30 m resolution). It also proved relatively insensitive to errors in measured radiance, but very sensitive to single scatter albedo and aerosol optical depth. Kaufman and Fraser (1984) looked further at the interdependencies between sizes of the contrast fields, their albedo, mean background reflectance and optical thickness. This study showed that the horizontal extent of the contrast fields is important because the contrast reduction due to the "adjacency effect," or the brightening of dark pixels by adjacent bright pixels, is proportional to the aerosol scale height (generally taken as ~ 1 kilometer) and a uniform surface cannot be assumed.

Finally, Tanre *et al.* (1988) and Tanre and Legrand (1991) matured the contrast reduction technique and applied the process to overland Saharan dust cases. Tanre *et al.* (1988) developed a method to use the variance of the histogram of the surface reflectance to characterize contrast reduction assuming a constant ground reflectance. This method showed promise in the Saharan environment when applied to Landsat Thematic Mapper data, but the authors demonstrated a sensitivity to registration errors between scenes, especially in an urban environment. While successful in the Saharan cases, these methods still require the use of direct and diffuse transmission functions, which are based on assumptions about the aerosol species and size distribution.

2. Dark Object Method

Kaufman and Sendra (1988) developed an algorithm to automate atmospheric corrections to visible and near-infrared satellite imagery based on the presence of dense dark vegetation within the image. This approach used an assumed reflectance for dense dark vegetation and was applicable over a wide range of spatial resolutions ranging from 10-meter resolution to one kilometer or larger. The algorithm assumed that radiance beyond what is reflected by dark surface objects was due to path radiance attributed to aerosol scattering. While this method is sensitive to the assumed reflectance of the vegetation, Kaufman and Sendra (1988) contend that it is relatively insensitive to

assumed aerosol characteristics, accuracy of satellite calibration, or exact characterization of the specific fraction of vegetation.

Similar techniques have been applied to inland bodies of water using red and near-infrared channels. Like the vegetation technique, water is assumed to have negligible surface reflectance (given sufficiently deep water) such that any additional radiance is due to path radiance attributed to aerosol scattering (Kidder and Vonder Haar 1999). The "dark object" approach remains the most resilient approach to overland AOD retrievals, but it breaks down rapidly over urban or arid regions, which tend to have high surface reflectance and a significant absence of both vegetation and large, deep bodies of water.

Kaufman *et al.* (1997a, 1997b) describe a dark object method that takes advantage of the correlation between surface reflectance in the mid-infrared wavelengths and the visible wavelengths. Developed for automated operational retrievals using the MODIS sensor, this method sought to use the low aerosol optical thickness in the mid-infrared (2.1 and 3.8 µm) wavelengths to identify dark pixels and then estimate the reflectance of those pixels in the visible wavelengths (0.47 and 0.66 µm). The 2.1-µm channel on MODIS, while largely unaffected by most aerosols, is affected by dust. Likewise, the 3.8-µm channel can become contaminated by emission. These problems, along with the assumption of average view geometry across the scene, lead to variations in the correlation between the mid-infrared and visible wavelengths resulting in the frequent need to update the surface reflectance database. Extension of this method to brighter, non-vegetated areas has been subject to the same difficulties.

Hsu *et al.* (2004) developed an additional dark-object method, called "Deep Blue," to address aerosol optical depth retrievals in areas where the surface brightness overwhelms any signal from the aerosol content such as semi-arid, arid, and urban areas. In these areas, the surface reflectance is typically bright in the red and near-infrared, but considerably darker in the blue end of the spectrum. This method uses combinations of blue bands (i.e., 412 and 490 nm for SeaWiFS; 412 and 470 nm for MODIS) and relies on the fact that surface reflectance is below the critical value, approximately 0.15 or 15%,

for dust at 412 nm. The blue wavelengths allow the satellite to detect lower aerosol loading as compared to more traditional methods using channels at 600 nm or above where the surface reflectance is greater than 0.15. However, the variability of the optical properties of dust is much greater in the blue region of the spectrum. For this reason, the proposed method also includes the use of a red band for heavy-loading cases. Uncertainties in this method derive from the use of a 0.1° by 0.1° database of surface reflectance, assumptions in the vertical profile, and approximations of particle shape. Finally, while two blue channels are available from MODIS and SeaWiFS imagery, current high-spatial resolution commercial imagery satellites only have one blue channel and cannot accommodate this technique.

3.   Multi-angle Method

The multi-angle method of overland AOD retrieval, described by Veefkind *et al.* (1998) for the Along Track Scanning Radiometer 2 (ATSR-2) and Martonchik *et al.* (2004) for the Multi-angle Imaging SpectroRadiometer (MISR), is unique to multi-view sensors. ATSR-2 has two views with seven channels. MISR has nine views with four channels. Multiple radiance values for the same surface from these multi-view sensors allow the characterization of surface reflectance, while the atmosphere component is modeled for various aerosol types and concentrations. The combination of these various modeled atmospheric reflectances and the surface reflectance are compared to the top of the atmosphere reflectance to determine the appropriate combination.

Both Veefkind *et al.* (1998) and Martonchik *et al.* (2004) report much success using multi-angle methods, however, such methods are highly dependent on the sensor's multi-view capabilities and the modeled aerosols. While current high-resolution satellites are pointable, multi-angle collections of a single point are typically difficult and expensive. Additionally, extensive look-up tables are required for the modeled aerosols. Such look-up tables are sensitive to aerosol phase function choices as well as aerosol size distributions. For these reasons, a multi-angle approach is ill-suited to real-time, operational AOD retrievals over land using high-resolution satellite imagery.

B.   SHADOW METHOD

While some of the above techniques and sensors are capable of AOD retrievals over bright surfaces, the resultant area-averaging significantly reduces the applicability to smaller scale phenomena that can affect military operations. Therefore, this dissertation describes an alternative approach to AOD retrieval that is applicable to commercial high-spatial resolution imagery and compliments the above approaches. Today's commercial high-spatial resolution satellite imagery is now capable of resolving individual ground features such as buildings, roadways, waterways, etc. Also resolvable are the shadows cast by vertically extended ground features as depicted in Fig. 1.
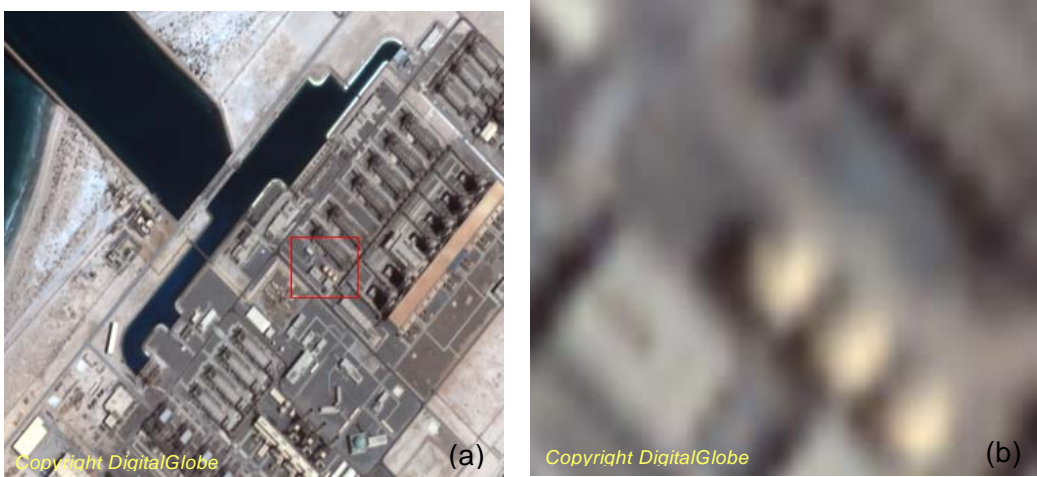
Figure 1.   An example of a QuickBird RGB image of a water desalinization plant northwest of Abu Dhabi, UAE taken 16 September 2004: (a) general overview of the area and (b) a zoom showing shadowed areas (courtesy of DigitalGlobe).

The subset of a QuickBird image shown in Fig. 1(a) depicts a water treatment facility where building, holding tanks, and other industrial infrastructure cast shadows over relatively homogeneous backgrounds. The image in Fig. 1(b) shows the type of shadows available for analysis using the proposed method. When a shadow falls over an area of constant surface reflectance (a condition verifiable by inspection at this resolution), the difference in observed radiance inside and outside of the shadow contains

information on the properties of the intervening aerosol. Area-averaged optical depths can be derived from an image with multiple shadow features.

In the next chapter, a formal theoretical development of this technique is presented and a governing equation is derived. The major components of the downward-directed irradiance are described in Fig. 2. One can see in Fig. 2 that the downward-directed irradiance in the outside of the shadow region is composed of direct transmission, diffuse transmission, and diffuse reflection back to the surface. Inside the shadow region, the downward-directed irradiance is composed only of the diffuse transmission and diffuse reflection back to the surface. Therefore, a difference between the unshaded and shaded region is a function of the direct transmission and contains information about the optical depth.
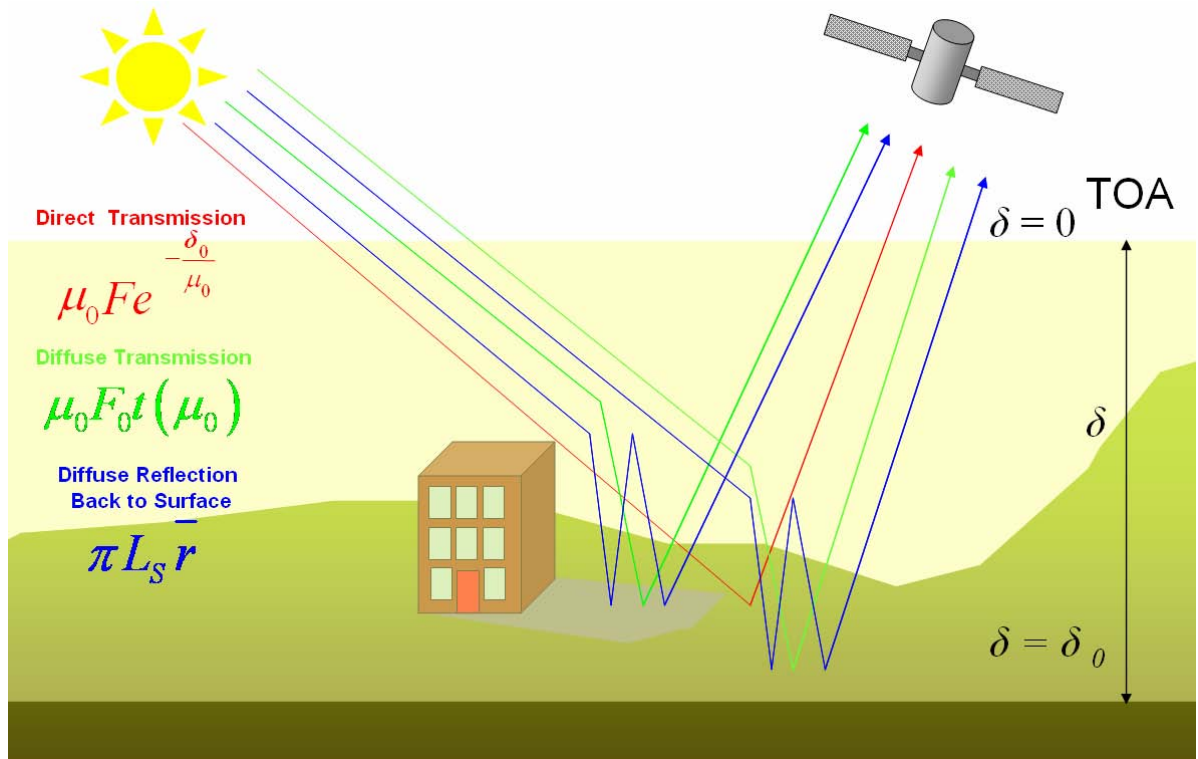
Figure 2.   The shadow method uses the difference between the radiances within and outside of the shadowed area to quantify the direct transmission and the total optical depth. Optical depth is defined as the sum of extinction above a vertical position in the atmosphere (therefore equals zero at the top of the atmosphere).

II. THEORETICAL DEVELOPMENT

A. PRINCIPLES OF INVARIANCE

A principles-of-invariance (POI) method of radiative transfer was chosen for this study and is based on physical statements and mathematical formulations of the reflection and transmission of light as proposed by Ambartzumian (1958) and developed by Liou (2002). POI provides intuitive partitioning of the pathways of radiative effects contributing to satellite measured radiances. This is useful when comparing the resulting radiance fields for shaded and unshaded regions in high-spatial resolution imagery and allows one to selectively omit source terms where appropriate.

1. Diffuse and Reflected Radiance Fields

Following Liou's (2002) development of the POI method to solving the multiple-scattering problem, one must first express the resulting diffuse radiance field in terms of a reflection function, R, and a transmission function, T. The reflected and transmitted radiance fields can be described as:

$$L_r\left(0;\mu,\phi\right)=\frac{1}{\pi}\int_0^{2\pi}\int_0^1 R\left(\mu,\phi;\mu',\phi'\right)L_0\left(-\mu',\phi'\right)\mu'd\mu'd\phi',\qquad(1)$$

$$L_t\left(\delta_0;-\mu,\phi\right)=\frac{1}{\pi}\int_0^{2\pi}\int_0^1 T\left(\mu,\phi;\mu',\phi'\right)L_0\left(-\mu',\phi'\right)\mu'd\mu'd\phi',\qquad(2)$$

where μ is the cosine of the viewing zenith angle (the minus sign indicating downward directed radiance), ϕ is the viewing azimuth in radians, and the primed values represent the angles from which diffuse radiance is scattered. The convention of listing the geometry to which the photon is reflected or transmitted first and the geometry from which the photon is reflected or transmitted second is used throughout. L_r represents the reflected diffuse radiance field integrated over the hemisphere at the top of the atmosphere (i.e. $\delta = 0$) and L_t represents the transmitted diffuse radiance field integrated over the hemisphere at the surface (i.e. $\delta = \delta_0$). L_0 represents the intensity of solar

radiation incident at the top of the scattering layer and, as a practical matter, may be approximated to the monodirectional form:

$$L_0(-\mu,\phi) = \Delta(\mu-\mu_0)\Delta(\phi-\phi_0)F_0, \tag{3}$$

where Δ is the Dirac delta function, F_0 is the solar flux density, or irradiance, in the direction of the incident beam, and (μ_0,ϕ_0) represent the solar geometry. The minus sign in the geometry notation indicates downward directed radiance.

Reflection and transmission functions may now be defined from Eqs. (1) and (2):

$$R(\delta_0;\mu,\phi;\mu_0,\phi_0) = \pi L_r(0;\mu,\phi)/(\mu_0 F_0), \tag{4}$$

$$T(\delta_0;\mu,\phi;\mu_0,\phi_0) = \pi L_t(\delta_0;-\mu,\phi)/(\mu_0 F_0). \tag{5}$$

It is important to note here that the diffuse radiance, L_t, does not contain the directly transmitted component of solar radiance. The reflectance function, R, when applied to satellite remote sensing, is termed bi-directional reflectance, and is given by:

$$R(\delta_0;\mu,\phi;\mu_0,\phi_0) = \pi L(0;\mu,\phi)/(\mu_0 F_0) \tag{6}$$

$$= \frac{\pi\tilde{\omega}}{(\mu+\mu_0)}\left(\frac{P(\mu,\phi;-\mu_0,\phi_0)}{4\pi}\right)\left\{1 - e^{\left(-\delta\left(\frac{1}{\mu}+\frac{1}{\mu_0}\right)\right)}\right\}, \tag{7}$$

where $\tilde{\omega}$ is the single scatter albedo of the aerosol particles, P is the scattering phase function, or probability of scatter based on solar and viewing geometry, and δ is the optical depth of the atmosphere. For sufficiently small optical depths, Eq. (7) can be simplified by linearization to:

$$R_L(\delta_0;\mu,\phi;\mu_0,\phi_0) = \frac{\pi\tilde{\omega}\delta}{(\mu\mu_0)}\left(\frac{P(\mu,\phi;-\mu_0,\phi_0)}{4\pi}\right). \tag{8}$$

Bi-directional reflectance is now directly proportional to optical depth and scattering phase function for single-scatter approximations in low optical depth atmospheres.

Using Eqs. (4) and (5), one may now define reflection, r, and diffuse transmission, t, for the reflected and transmitted flux densities, or irradiances, as:

$$r(\mu_0) = \frac{F_{dif}^{\uparrow}(0)}{\mu_0 F_0} = \frac{1}{\pi} \int_0^{2\pi} \int_0^1 R(\mu, \phi; \mu_0, \phi_0) \mu d\mu d\phi, \text{ and} \qquad (9)$$

$$t(\delta_0, \mu_0) = \frac{F_{dif}^{\downarrow}(\delta_0)}{\mu_0 F_0} = \frac{1}{\pi} \int_0^{2\pi} \int_0^1 T(\delta_0; \mu, \phi; \mu_0, \phi_0) \mu d\mu d\phi, \qquad (10)$$

where $F_{dif}^{\uparrow}$ and $F_{dif}^{\downarrow}$ represents the upward and downward diffuse flux densities at the top of the atmosphere and the surface respectively. These and the preceding relationships will be used to build a flux density balance in order to characterize the top of the atmosphere radiance viewed by the satellite.

2. Flux Density (Irradiance) Balance

A simple flux density, or irradiance, balance must be established between the upward and downward flux density. When surface reflectance is considered, this becomes:

Upward Flux Density (W/m²)= Surface Reflectance · Downward Density (W/m²).

If the ground is considered to reflect according to Lambert's Law (e.g. independent of both view azimuth and zenith angles), then upward intensity, or radiance, can be described by

$$L(\delta_0; \mu, \phi) = L_s = const, \qquad (11)$$

where L_s is surface radiance, δ_0 is total optical depth, μ is the cosine of the viewing zenith angle, and ϕ is the viewing azimuth. If total reflected intensity, or radiance, to space, including the contribution from surface reflection, is represented by $L*(0;\mu,\phi)$, then

$$L*(0; \mu, \phi) = L(0; \mu, \phi) + \frac{1}{\pi} \int_0^{2\pi} \int_0^1 T(\delta_0; \mu, \phi; \mu_0, \phi_0) L_s \mu' d\mu' d\phi' + L_s e^{-\delta_0/\mu}, \quad (12)$$

where L^* represents the reflected radiance, $T\left(\delta_0;\mu,\phi;\mu_0,\phi_0\right)$ is the transmission function as defined by Eq. (5), μ' is the cosine of the surface source zenith angle, and ϕ' is the surface source azimuth. Reciprocity is assumed here such that the transmission function defined in Eq. (5) for incoming solar radiation is the same for surface reflected radiation. The terms on the RHS of Eq. (12) are the radiance at the top of the atmosphere due to reflection by the atmosphere, the diffuse transmission of isotropic intensity from the surface, and direct transmission of isotropic intensity from the surface. Physical depictions of the various components of Eq. (12) are shown in Fig. 3(a).
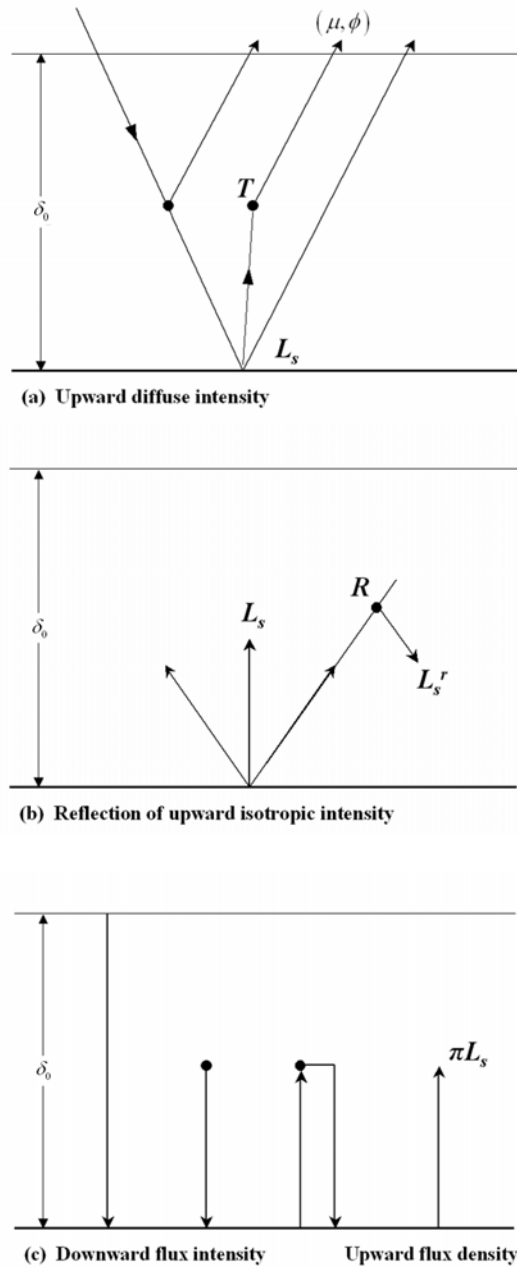
Figure 3.   Scattering configuration based on principles of invariance with the inclusion of surface reflection: (a) upward diffuse intensity; (b) reflection of upward isotropic intensity; and (c) downward flux density and upward flux density. (adapted from Liou 2002)

The first term on the RHS of Eq. (12), the radiance due to reflection at the top of the atmosphere, can be defined as

$$L(0; \mu, \phi) = \mu_0 F_0 R(\delta_0; \mu, \phi; \mu_0, \phi_0) , \qquad (13)$$

where F_0 is the incoming spectral solar irradiance and $R(\delta_0; \mu, \phi; \mu_0, \phi_0)$ is the reflection function as defined in Eq. (4). The second term on the RHS, the diffuse transmission of isotropic intensity from the surface, can be rewritten as

$$t(\delta_0, \mu) L_s = \frac{L_s}{\pi} \int_0^{2\pi} \int_0^1 T(\delta_0; \mu, \phi; \mu_0, \phi_0) \mu' d\mu' d\phi' , \qquad (14)$$

where $t(\delta_0, \mu)$ represents the diffuse transmission as defined by Eq. (10). Diffuse transmission represents that portion of the transmitted radiation not due to direct transmission of incident solar radiation as defined by $F_0 e^{-\delta_0/\mu_0}$.

At this point, radiation at the sensor due to reflection by the atmosphere, diffuse transmission of surface radiance, and direct transmission of the surface radiance have been taken into account. However, some portion of the isotropic intensity from the surface will also be reflected by the atmosphere and add to the downward intensity. This can be characterized by

$$L_s^r(-\mu) = \frac{1}{\pi} \int_0^{2\pi} \int_0^1 R(\delta_0; \mu, \phi; \mu', \phi') L_s \mu' d\mu' d\phi' = L_s r(\mu) , \qquad (15)$$

where $r(\mu)$ represents the albedo of the aerosol and is based on the principle of reciprocity, $R(\mu, \phi; \mu', \phi') = R(\mu', \phi'; \mu, \phi)$. On the LHS of Eq. (15), $-\mu$ again denotes contribution to downward intensity (see Fig. 3(b)).

The total intensity transmitted to the ground, including the ground contribution due to reflection by the atmosphere, as described in Eq. (15), can be written as:

$$L * (\delta_0; -\mu, \phi) = \mu_0 F_0 T(\delta_0; \mu, \phi; \mu_0, \phi_0) + L_s r(\mu) . \qquad (16)$$

Referring back the to the initial flux density balance, one must now solve for the upward flux density, or surface radiance.

The upward flux density due to a Lambertian surface is balanced by the surface reflection of the downward flux density such that,

$$\pi L_s = r_s \times \textit{downward flux density.}$$

The downward flux density can be partitioned into three components based on the development above. Fig. 3(c) shows a schematic of the three components; direct transmission, diffuse transmission, and the component of surface radiance reflected by the atmosphere. The direct transmission component can be described the most simply by,

$$\mu_0 F_0 e^{-\delta_0/\mu_0} . \tag{17}$$

The diffuse transmission component can be written as

$$\int_0^{2\pi}\int_0^1 L(\delta_0;-\mu,\phi)\mu d\mu d\phi = \int_0^{2\pi}\int_0^1 (\mu_o F_0/\pi)T(\delta_0;\mu,\phi;\mu_0,\phi_0)\mu d\mu d\phi$$

$$= \mu_0 F_0 t(\delta_0,\mu_0) . \tag{18}$$

The final component of the downward flux density is that which is due to the surface radiance reflected by the atmosphere back to the surface, and can be written as

$$\int_0^{2\pi}\int_0^1 L_s^r(-\mu)\mu d\mu d\phi = \pi L_s \bar{r} , \tag{19}$$

where $\bar{r}$, the average hemispheric albedo of the aerosol particles, or mean aerosol reflectance, over the area of consideration. Mean aerosol reflectance is defined as:

$$\bar{r} = \frac{1}{\pi}\int_0^{2\pi}\int_0^1\int_0^{2\pi}\int_0^1 R\left(\delta_0;\mu',\phi';\mu'',\phi''\right)\mu'\mu''d\mu'd\phi'd\mu''d\phi'' , \tag{20}$$

where (μ',ϕ') represents the geometry of the surface leaving radiance and (μ'',ϕ'') represents the geometry for the direction from which the photon is scattered.

3.   Derivation of Mean Aerosol Reflectance

The mean aerosol reflectance represents the percentage of the reflected radiant energy from the aerosol layer in either the upper or low hemisphere. In this context, the mean aerosol reflectance is determined for the lower hemisphere with surface leaving radiance as a Lambertian source. The derivation of the mean aerosol reflectance follows.

The basic equation for radiative transfer for plane parallel atmospheres as adapted from Liou (2002) for diffuse intensity is:

$$\mu\frac{dL(\delta;\mu,\phi)}{d\delta} = L(\delta;\mu,\phi) - J(\delta;\mu,\phi), \tag{21}$$

where J is the source function representing contributions from both the diffuse beam multiple scattering and the direct solar beam scattering. The source function, J, is given by:

$$J(\delta;\mu,\phi) = \frac{\tilde{\omega}}{4\pi}\int_0^{2\pi}\int_{-1}^1 L(\delta;\mu',\phi')P(\mu,\phi;\mu',\phi')d\mu'd\phi' +$$

$$\frac{\tilde{\omega}}{4\pi}F_0 P(\mu,\phi;-\mu_0,\phi_0)e^{-\delta/\mu_0}, \tag{22}$$

where P is the scattering phase function based on incident and resultant angles, F_0 is the incoming spectral solar irradiance at the top of the atmosphere, and $\tilde{\omega}$ is the single scatter albedo, or the ratio of scattering to total extinction.

Now, Eq. (21) must be solved with the assumption that there are no diffuse intensities at the top or bottom of the atmosphere. As such, the solution in integral form becomes:

$$L(0;\mu,\phi) = \int_0^\delta J(\delta';\mu,\phi)e^{-\delta/\mu}\frac{d\delta'}{\mu},$$

$$= \frac{\mu_0 F_0 \tilde{\omega}}{(\mu_0+\mu)}\left(\frac{P(\mu,\phi;\mu_0,\phi_0)}{4\pi}\right)\left\{1-e^{\left(-\delta\left(\frac{1}{\mu}+\frac{1}{\mu_0}\right)\right)}\right\} \tag{23}$$

18

where δ' is the optical depth of a discreet layer of the atmosphere. The bi-directional reflectance, as introduced as Eqs. (6) and (7), can be taken as:

$$R\left(\delta;\mu,\phi;\mu_0,\phi_0\right)=\pi L\left(0;\mu,\phi\right)/\left(\mu_0 F_0\right),\text{ or} \qquad (24)$$

$$=\frac{\pi\tilde{\omega}}{\left(\mu_0+\mu\right)}\left(\frac{P\left(\mu,\phi;\mu_0,\phi_0\right)}{4\pi}\right)\left\{1-e^{\left(-\delta\left(\frac{1}{\mu}+\frac{1}{\mu_0}\right)\right)}\right\}, \qquad (25)$$

where, bi-directional reflectance is a function of the single scatter albedo, $\tilde{\omega}$, the scattering phase function, P, and the optical depth, δ. The reflectance, r, can be determined from the bi-directional reflectance by integrating over all zenith and azimuth angles and goes as:

$$r\left(\delta,\mu_0\right)=\frac{1}{\pi}\int_0^{2\pi}\int_0^1 R\left(\delta;\mu,\phi;\mu_0,\phi_0\right)\mu d\mu d\phi . \qquad (26)$$

The resulting reflectance is a function of incident angle. Changing the radiant source from the sun to the surface leaving radiance, the angle variables are now changed to $\left(\mu',\phi'\right)$ and $\left(\mu'',\phi''\right)$ to represent the cosine of the incident and resultant zenith angle and azimuth angle respectively.

The bi-directional reflectance is then integrated over all zenith and azimuth angles. This integration, with Eq. (7) substituted into Eq. (26) and using the new notation, becomes:

$$\overline{r}=\frac{1}{\pi}\int_0^{2\pi}\int_0^1\int_0^{2\pi}\int_0^1\frac{\tilde{\omega}\mu'\mu''}{\left(\mu'+\mu''\right)}\left(\frac{P(\Theta)}{4\pi}\right)\left(1-e^{-\delta\left(\frac{1}{\mu'}+\frac{1}{\mu''}\right)}\right)d\mu'd\phi'd\mu''d\phi'', \qquad (27)$$

where Θ represents the scattering angle based on the source and resultant zenith and azimuth angles. The mean aerosol reflectance is now a function of single scatter albedo, $\tilde{\omega}$, scattering phase function, P, and the optical depth, δ. The scattering phase function, which varies greatly with different types of aerosols, is approximated by the Henyey-Greenstein phase function for practical purposes and is defined as:

$$P(\Theta) = \frac{1 - g^2}{\left(1 + g^2 - 2g\cos\Theta\right)^{3/2}}, \tag{28}$$

where Θ represents the scattering angle and g is the asymmetry parameter varying between 1 for fully forward scattering conditions, –1 for fully backscattering conditions, and 0 for isotropic conditions (Henyey and Greenstein, 1941). The mean aerosol reflectance is now a function of single scatter albedo, $\tilde{\omega}$, optical depth, δ, and the asymmetry parameter, g. Single scatter albedo and the asymmetry parameter can be assumed based on expected aerosol type, however, only one aerosol species can be represented. In cases where two or more aerosol types with distinctly different characteristics are present, such assumptions may break down unless the optical properties can be represented by an appropriate averaging of the characteristics of individual aerosol types.

4.   Development of the Governing Equation

The flux density balance may now be described using Eqs. (17), (18) and (19) as

$$\pi L_s = r_s \left(\mu_0 F_0 e^{-\delta_0/\mu_0} + \mu_0 F_0 t(\delta_0, \mu_0) + \pi L_s \bar{r} \right). \tag{29}$$

Eq. (29) can be solved for L_s, surface intensity, or radiance, as

$$L_s = \frac{r_s}{1 - r_s \bar{r}} \frac{\mu_0 F_0}{\pi} \left(e^{-\delta_0/\mu_0} + t(\delta_0, \mu_0) \right). \tag{30}$$

Eq. (30) represents the radiance as measured at the surface. When viewed from the satellite, the directly transmitted radiance is again subject to attenuation as measured by the optical depth of the atmosphere. As such, Eq. (30) then becomes:

$$L_s = \left[\frac{r_s}{1 - r_s \bar{r}} \frac{\mu_0 F_0}{\pi} \left(e^{-\delta_0/\mu_0} + t(\delta_0, \mu_0) \right) \right] e^{(-\delta_0/\mu)}, \tag{31}$$

where the additional extinction term is a function of μ, the cosine of the viewing zenith angle, representing the path loss due to the optical depth from the surface to the satellite sensor.

20

Eq. (31) provides a convenient way to quickly determine all factors affecting the observed surface radiance. Applying this equation to our original problem of characterizing aerosol optical depth from high-spatial resolution imagery, one can use Eq. (31) unaltered to represent that radiance we would observe outside of shaded areas within the image.

A slight adjustment to Eq. (31) must be made when considering shaded areas. By definition, a shaded region lacks the direct transmission term described by Eq. (17). Removing this term, but retaining the contributions due to diffuse transmission and atmosphere reflected surface radiance, one gets

$$L_s^{shaded} = \left[\frac{r_s}{1 - r_s \bar{r}} \frac{\mu_0 F_0}{\pi} t(\delta_0, \mu_0) \right] e^{(-\delta_0 / \mu)} . \tag{32}$$

At the high spatial resolutions found in QuickBird imagery, one can easily observe the top of the atmosphere radiance both within and outside of shaded areas. The unshaded/shaded radiance difference at the at the top of the atmosphere can be equated to surface unshaded/shaded radiance difference since both the unshaded and shaded radiances are subject to the same losses and the the relative difference in radiance values is preserved. If an area adjacent, but just outside of the shaded area is chosen such that the surface reflectance of the shaded and unshaded areas is the same, then the difference between Eqs. (31) and (32) can be used to characterize the observed difference in intensities as

$$L_s^{unshaded} - L_s^{shaded} = L_d = \frac{r_s}{1 - r_s \bar{r}} \frac{\mu_0 F_0}{\pi} e^{-\delta_0 \left(\frac{1}{\mu_0} + \frac{1}{\mu} \right)} . \tag{33}$$

Solving Eq. (33) for total optical depth, δ_0, yields:

$$\delta_0 = \left(\frac{\mu_0 \mu}{\mu + \mu_0} \right) \ln \left[\left(\frac{r_s}{1 - r_s \bar{r}} \right) \left(\frac{\mu_0 F_0}{\pi L_d} \right) \right] . \tag{34}$$

21

Eq. (34) now becomes the governing equation for retrieving total optical depth from the difference in satellite measured radiances using a known spectral solar irradiance specific to the channel considered and viewing and solar geometries.

5.   Optical Depth due to Molecular Rayleigh Scattering

The molecular Rayleigh optical depth is determined using wavelength, pressure, and height dependent relationship introduced by Russell *et al.* (1993) as:

$$\delta_R(\lambda) = \left(0.00864 + 6.5 \times 10^{-6} H\right)\lambda^{-b(\lambda)}\left(p / p_0\right), \qquad (35)$$

$$b(\lambda) = 3.916 + 0.074\lambda + 0.050 / \lambda,$$

where λ is the wavelength in micrometers, H is height above sea level of the radiometer in kilometers, p is the atmospheric pressure at the altitude of the radiometer in hPa, and p_0 is the sea-level reference pressure, taken as 1013.25 hPa. Russel *et al.* (1993) used the wavelength and altitude dependence of molecular Rayleigh optical depth best fit data of Frolich and Shaw (1980) as well as the recommendation of Young (1980) for the depolarization factor (0.00864 in Eq. (35)). Table 1 shows the molecular Rayleigh optical depths calculated for the QuickBird channels assuming the center effective wavelength, a radiometer height of zero kilometers, and an atmospheric pressure at the radiometer of 1013.25 hPa.

Table 1. Molecular Rayleigh optical depths for each of the QuickBird channels based on Eq. (35) assuming a radiometer height of 0 kilometers and atmospheric pressure of 1013.25 hPa.

Band	Center Effective Wavelength (micrometers)	Molecular Rayleigh Optical Depth
Blue	0.482	0.170
Green	0.556	0.092
Red	0.658	0.047
Near-Infrared	0.816	0.019
Panchromatic	0.673	0.049

The mean aerosol reflectance is intended to approximate the effects of the diffuse sky radiance by scaling aerosol reflectance by total optical depth. While the diffuse field consists of not only aerosol particle effects, but also molecular Rayleigh scattering effects, it is assumed that at all but the lowest optical depths, that the aerosol particle component will dominate. As such, the asymmetry parameter used is for the aerosol particles vice a combination of asymmetry parameters for both the aerosol particles (~0.6-0.7) and the molecular Rayleigh scattering (~ 0). Such a combination would cause a lowering of the effective asymmetry parameter and result in a slight increase in the mean aerosol optical depth. Due to the process proposed in Chapter IV, a systematic high bias in mean aerosol reflectance results from the overestimation of initial total optical depth. Mean aerosol reflectance is then used to partition top of the atmosphere reflectance, resulting in a low bias to surface reflectance. The inclusion of an asymmetry parameter for molecular Rayleigh scattering in the mean aerosol reflectance calculation would increase this bias by increasing mean aerosol reflectance. For these reasons, molecular Rayleigh scattering effects are neglected in the determination of mean aerosol reflectance and handled explicitly in partitioning the final total optical depth.

6.   Molecular Absorption due to Atmospheric Gases

As described in Liou (2002), gaseous molecules in motion can store various forms of energy at descrete (i.e., quantum) values. The first type of enegry, translational energy, results from the molecule's movement through space. The second type, rotational energy, results from a molecule's rotation about an axis through its center of gravity. The third type, vibrational energy, results from the oscillation of individual atoms about their equilibrium positions relative to one another. Finally, changes in the energy state of the electrons within the molecule result in electronic energy. Absorption and emission of radiation result when molecules, or their individual atoms, transition from one energy state to another.

Liou (2002) further discusses the radiative transitions in which molecules must couple with an electromagnetic field, creating an electric dipole moment, so that an exchange of energy can take place. The dipole moment exists when the positive and negative charge of the molecule has a nonzero separation. Some gases, such as water vapor and ozone, have a permanent electric dipole moment due to the asymmetrical charge distribution that results from their structure. These molecules are very radiatively active. Other molecules, such as diatomic nitrogen and oxygen, are largely inactive in the infrared due to their linear structure and symmetrical charge distributions, however weak magnetic dipole moments can allow transitions in the ultraviolet and visible regions of the spectrum.

Continuing with the discussion of Liou (2002), vibrational energy changes are typically much larger than rotational energy changes. Pure rotational changes are rarely seen in the visible and near-infrared region, however, the energy involved in vibrational changes is large enough that simultaneous rotational transitions occur. These vibrational-rotational bands are largely found in the intermediate infrared spectrum, although some effect also seen in the near-infrared. Finally, electronic transitions require a high-energy photon, limiting these changes to the ultraviolet and visible portion of the spectrum (Liou 2002).

Electronic transitions associated with ozone occur in the ultraviolet region while molecular oxygen causes in a narrow band centered at 0.77 µm (Kidder and Vonder Haar 1995). The vibrational transitions discussed above are typically associated with carbon

dioxide (CO_2) and water vapor (H_2O_v) and are limited to wavelengths in the near infrared and longer (Kidder and Vonder Haar 1995). The transmittance spectra of the main atmospheric gases as well as the Rayleigh molecular scattering spectrum are shown for a mid-latitude, summer atmosphere with the QuickBird spectral response function in Fig. 4. Notice that the spectral response of the QuickBird channels either avoids or minimizes the impact of the absorption features. This is typical of most high-resolution commercial satellites. For this reason, the effects of molecular absorption are initially assumed to be negligible. This assumption will be revisited in the discussion of possible sources of error in Chapters VII, VIII, and IX.
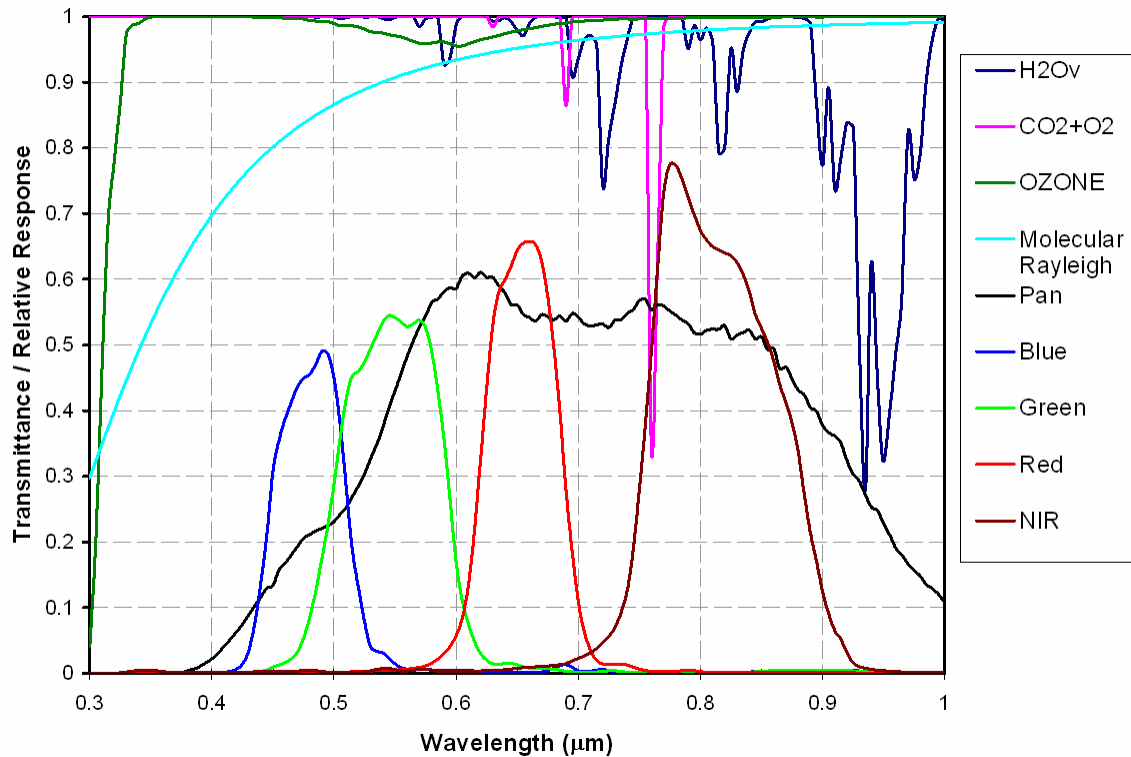
Figure 4. Atmospheric transmittance for water vapor, carbon dioxide, oxygen, ozone and molecular Rayleigh scattering based on a mid-latitude, summer atmosphere as compared to the relative spectral response functions for the each of the QuickBird channels (after DigitalGlobe 2005a).

B.   APPLICATION OF THE GOVERNING EQUATION

The application of the governing equation, as proposed here, leaves only one free variable for the user to manipulate in the AOD retrieval process. Solar and sensor zenith angles, surface reflectance determined from the unshaded radiance, and the unshaded/shaded radiance difference are determined from the imagery.   The solar irradiance is taken as a constant. Only the mean aerosol reflectance can be modified by the user through the choice of aerosol phase function and single scatter albedo. As such, the mean aerosol reflectance is the only "free" parameter in the application of the governing equation.

A corrective step is used for all cases when retrieving total optical depth with Eq. (34) since no *a priori* knowledge of surface reflectance or mean aerosol reflectance is typically available. Initially, mean aerosol reflectance is assumed to be much smaller than surface reflectance such that the product of surface reflectance and mean aerosol reflectance is much less than one. Top of the atmosphere reflectance is used as surface reflectance in this first step. A total optical depth is retrieved and subsequently used to determine a mean aerosol reflectance as outlined above. This mean aerosol reflectance is subtracted from the top of the atmosphere reflectance determined from the unshaded region, effectively partitioning top of the atmosphere reflectance into surface and mean aerosol reflectance, and total optical depth is again retrieved using Eq. (34).   This retrieved total optical depth is then corrected for molecular Rayleigh scattering to produce an aerosol optical depth.

IV. SENSITIVITY ANALYSIS

A. GOVERNING EQUATION

The governing equation for retrieving total optical depth, δ_0, from satellite-measured radiances was introduced as Eq. (34) in Chapter III. A sensitivity analysis is described here using the techniques of Taylor (1997) which look at the rate of change of total optical depth as each parameter is varied independently. The functional form of this analysis is the partial differentiation of Eq. (34) with respect to each of the key parameters. For this analysis, the focus will be L_d, the difference in shaded and unshaded radiance, r_s, the surface reflectance, $\bar{r}$, the mean aerosol reflectance, and μ, the cosine of the viewing zenith angle and the effect of the variation of each of these variables on total optical depth. Extraterrestrial spectral (solar) irradiance, F_0, will be taken as a constant for the channels being considered. The cosine of the solar zenith angle, μ_0, will be taken as a constant since the satellites being considered have a consistent local crossing time. However, the variation of solar zenith angle with season and latitude will be addressed separately at the end of this section. Molecular Rayleigh scattering corrections are made to the total optical depth based on the molecular Rayleigh optical depth as described in the previous chapter.

B. TERMS OF THE GOVERNING EQUATION

1. Difference in Unshaded and Shaded Measured Radiance

The aerosol optical depth as determined by Eq. (34), with corrections for molecular Rayleigh scattering, is inversely proportional to the difference in unshaded and shaded radiance, L_d, for all channels. It is useful, where possible, to recast Eq. (34) by combining multiple constants into one single constant prior to carrying out the partial differentiation. As such, Eq. (34) will be recast into the following:

$$\delta = c_1 \ln\left[c_2\left(\frac{1}{L_d}\right) \right] \qquad (36)$$

where the constants c_1 and c_2 represent:

$$c_1 = \frac{\mu_0 \mu}{\mu_0 + \mu} \tag{37a}$$

$$c_2 = \left(\frac{r_s}{1 - r_s \overline{r}}\right)\left(\frac{\mu_0 F_0}{\pi}\right). \tag{37b}$$

Using the power and chain rules for differentiation, the partial differential of optical depth with respect to the difference in observed radiance between unshaded and shaded areas is:

$$\frac{\partial \delta}{\partial L_d} = -\frac{c_1}{L_d}, \text{ or}$$

$$\frac{\partial \delta}{\partial L_d} = -\frac{\mu_0 \mu}{L_d (\mu_0 + \mu)}. \tag{38}$$

Fig. 5 shows Eq. (38) evaluated at solar zenith angles of (a) 0° and (b) 30° for a range of radiance differences and sensor zenith angles. It can be seen that sensitivity decreases with increasing sensor zenith angle or decreasing values of the cosine of the zenith angle. Likewise, the same can be said for solar zenith angle as its role is numerically identical to that of the sensor zenith angle.

(a)

(b)
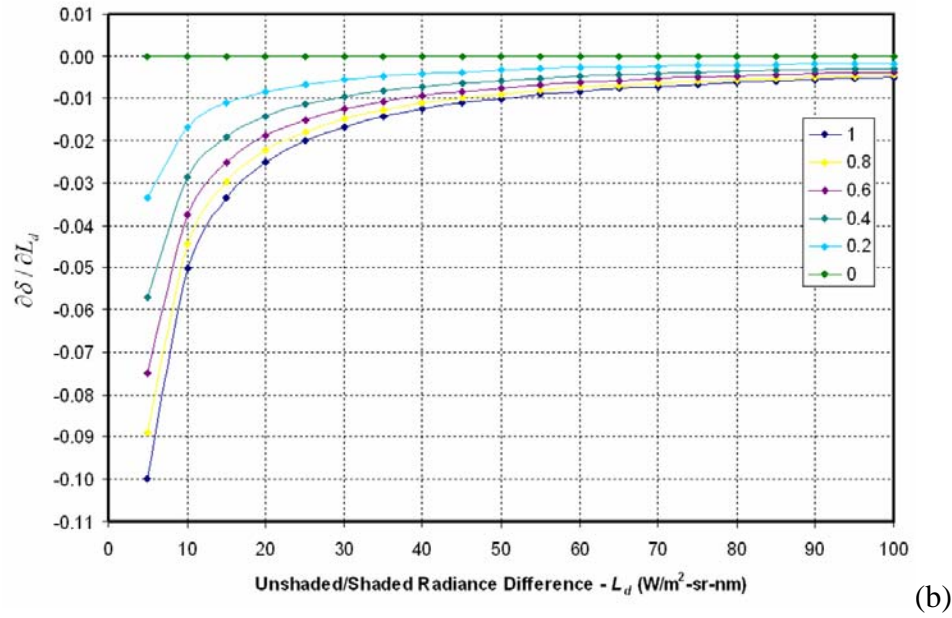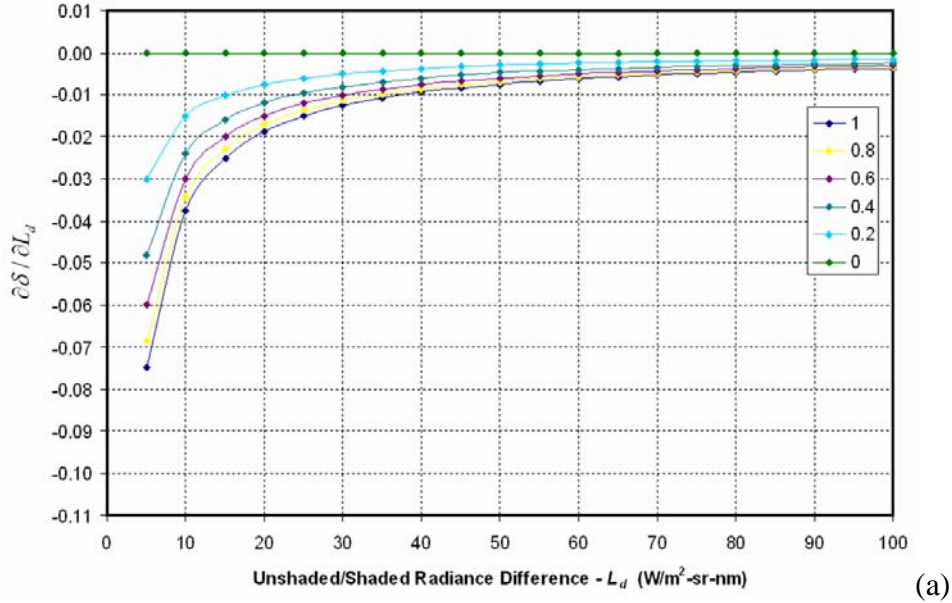
Figure 5.   The change in AOD with a change of 1 W m^{-2} sr^{-1} nm^{-1} in unshaded/shaded radiance difference as a function of unshaded/shaded radiance difference for a solar zenith angle of (a) 0° and (b) 30° and sensor zenith angle curves ranging from 0° to 90° (cosine values 1 to 0).

The goal here is to capture the coarsest sensitivity associated with each parameter by maximizing the value of Eq. (38). As such, the maximum rate of change in AOD with respect to values of 10 W m^{-2} sr^{-1} nm^{-1} for unshaded/shaded radiance difference, a solar zenith angle of 0°, and a senor zenith angle of 0° (the curve labeled 1) respectively from

Fig. 5(a). These values represent a high optical depth regime with both the sun and sensor directly overhead and result in a change of -0.05 per 1 W m^{-2} sr^{-1} nm^{-1} change in the radiance difference. Fig. 5(b) represents the same situation but at a solar zenith angle of 30°, a typical value encountered by the QuickBird sensor, and results in a sensitivity of -0.04 change in AOD per 1 W m^{-2} sr^{-1} nm^{-1} change in the radiance difference. The rate of change in AOD with changes in unshaded/shaded radiance difference increase rapidly below differences of 10 W m^{-2} sr^{-1} nm^{-1} with the lowest sensor zenith angles (higher cosine values). This can results in larger errors in retrieved AOD due to errors in unshaded/shaded radiance difference at the lowest sensor zenith angles.

2.   Surface Reflectance

The aerosol optical depth as determined by Eq. (34), with corrections for molecular Rayleigh scattering, is proportional the surface reflectance for all channels. Again, it is useful to recast Eq. (34) by combining multiple constants into one single constant where possible prior to carrying out the partial differentiation. As such, Eq. (34) will be recast into the following:

$$\delta = c_1 \ln\left[c_3 \left(\frac{r_s}{1 - r_s \bar{r}} \right) \right],$$
(39)

where c_1 remains the same as defined in Eq. (37a) and c_3 is defined as:

$$c_3 = \left(\frac{\mu_0 F_0}{\pi} \right).$$
(40)

Using the quotient, product and chain rules for differentiation, the partial differential of optical depth with respect to surface reflectance is:

$$\frac{\partial \delta}{\partial r_s} = \frac{c_1}{r_s \left(1 - r_s \bar{r} \right)}, \text{ or}$$

$$\frac{\partial \delta}{\partial r_s} = \left(\frac{\mu_0 \mu}{\mu_0 + \mu} \right) \frac{1}{r_s \left(1 - r_s \bar{r} \right)}.$$
(41)

Figure 6 shows Eq. (41) evaluated at solar zenith angles of (a) 0° and (b) 30° for a range of radiance differences and sensor zenith angles. It can be seen that sensitivity decreases with increasing sensor zenith angle or decreasing values of the cosine of the zenith angle. Likewise, the same can be said for solar zenith angle as its role is numerically identical to that of the sensor zenith angle. It must be noted that the values shown in Fig. 6 represent a change in AOD for a 100% change is surface reflectance. These values will be divided by 100 to determine the change in AOD for a 1% change in surface reflectance and will be discussed as such.
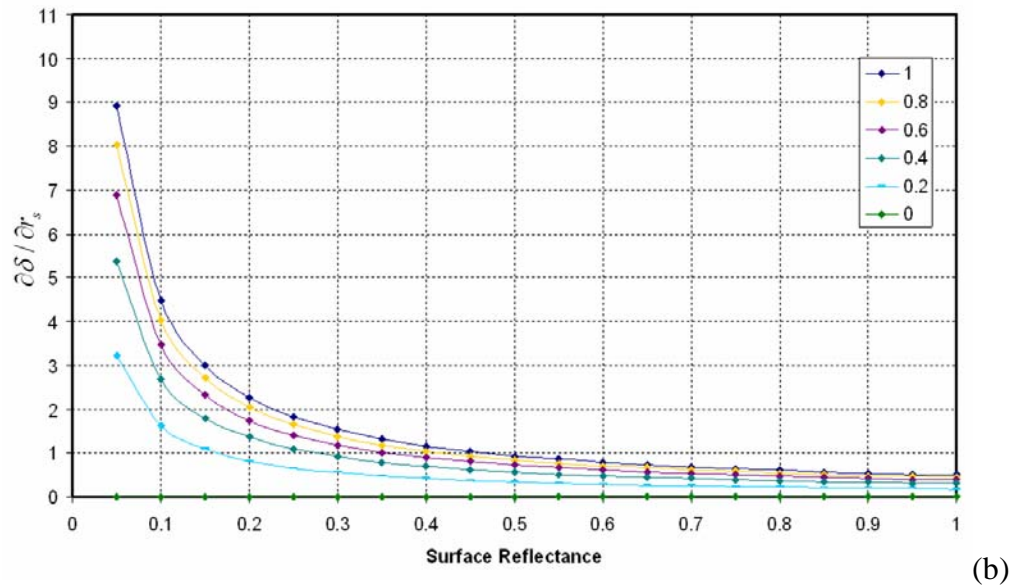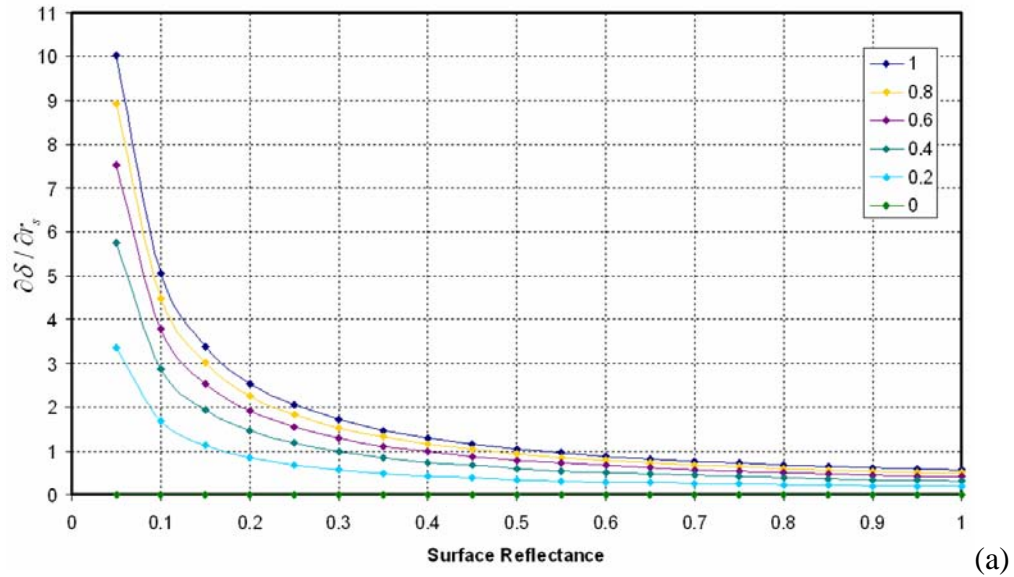
Figure 6.   The change in AOD with a change of 100% in surface reflectance as a
            function of surface reflectance for a solar zenith angle of (a) 0° and (b) 30°,
            a mean aerosol reflectance of 0.1 and sensor zenith angle curves ranging
            from 0° to 90° (cosine values 1 to 0).

    Again, the goal is to capture the coarsest sensitivity associated with each
parameter by maximizing the value of Eq. (41). As such, a maximum value of mean
aerosol reflectance and minimum values of solar/sensor zenith angles were chosen as 0.1,
0°, and 0° respectively from Fig. 6(a). These values represent a high optical depth
regime with both the sun and sensor directly overhead and result in a change in AOD of

0.05 per 1% change in surface reflectance. Fig. 6(b) represents the same situation but at a solar zenith angle of 30°, a typical value encountered by the QuickBird sensor, and results in a sensitivity of 0.04 change in AOD per 1% change in surface reflectance. One can readily see in Fig. 6 that the sensitivity to surface reflectance degrades rapidly below surface reflectance values of 0.15 at the lowest sensor zenith angles. Based on this, a minimum surface reflectance of 0.15 is suggested.

3.   Mean Aerosol Reflectance

The mean aerosol reflectance term in Eq. (34) acts to modify the influence of the surface reflectance, but only moderately so. To quantify this influence, again, it is useful to recast Eq. (34) by combining multiple constants into one single constant where possible prior to carrying out the partial differentiation. As such, Eq. (34) is recast into the following:

$$\delta = c_1 \ln \left[c_3 \left(\frac{r_s}{1 - r_s \bar{r}} \right) \right],$$
(42)

where c_1 and c_3 remain the same as defined in Eqs. (37a) and (40), respectively. Using the quotient, power and chain rules for differentiation, the partial differential of optical depth with respect to mean aerosol reflectance is:

$$\frac{\partial \delta}{\partial \bar{r}} = \frac{c_1 r_s}{\left(1 - r_s \bar{r} \right)}, \text{ or}$$

$$\frac{\partial \delta}{\partial \bar{r}} = \left(\frac{\mu_0 \mu}{\mu_0 + \mu} \right) \frac{r_s}{\left(1 - r_s \bar{r} \right)}.$$
(43)

Figure 7 shows Eq. (43) evaluated at solar zenith angles of (a) 0° and (b) 30° for a range of mean aerosol and surface reflectances. It can be seen that the rate of change in AOD with a 100% change in mean aerosol reflectance increases with increasing mean aerosol reflectance and increasing surface reflectance. An increase in solar or sensor zenith angle results in a decrease in the rate of change in AOD with a 100% change in mean aerosol reflectance as can be seen in the difference between Fig. 7(a) and 7(b). It

must be noted that the values shown in Fig. 7 represent a change in AOD for a 100% change in mean aerosol reflectance. These values will be divided by 100 to determine the change in AOD for a 1% change in mean aerosol reflectance and will be discussed as such.

(a)

(b)
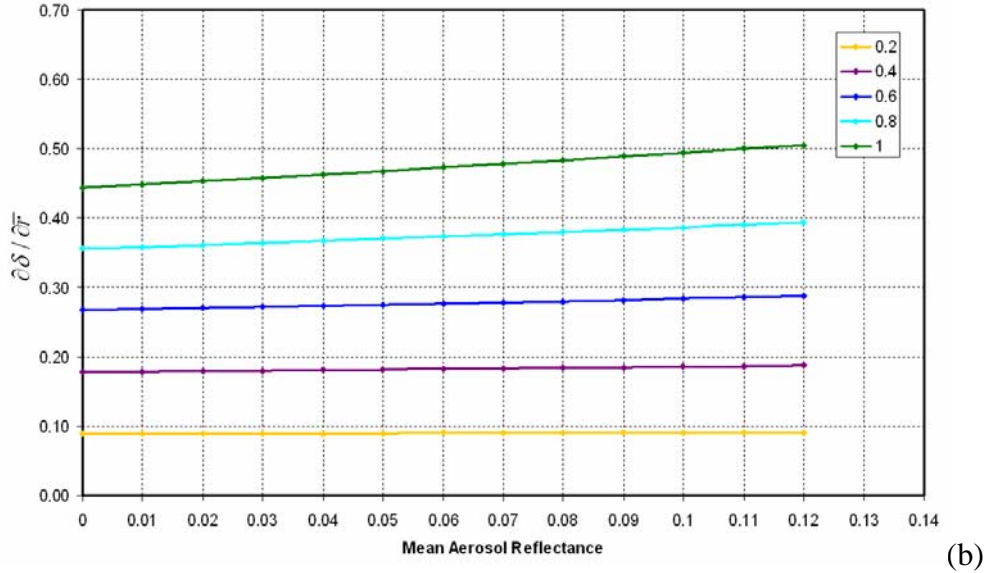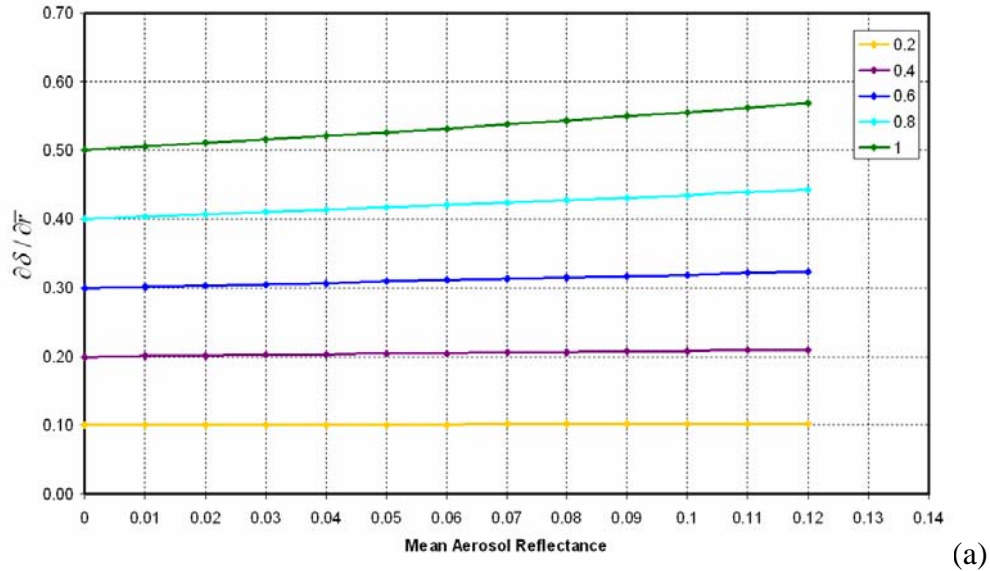
Figure 7.   The change in AOD with a change of 100% in mean aerosol reflectance as a function of mean aerosol reflectance for a solar zenith angle of (a) 0° and (b) 30°, for a sensor zenith angle 0° and surface reflectance curves for values ranging from 0.2 to 1.0.

Again, the goal is to capture the coarsest sensitivity associated with each parameter by maximizing the value of Eq. (43). As such, a maximum value of mean aerosol reflectance and minimum values of solar/sensor zenith angles were chosen as 0.12, 0°, and 0° respectively from Fig. 7(a). Fig. 7 also shows a slight linear increase in the rate of increase in AOD with a 1% increase in mean aerosol reflectance with respect to increasing mean aerosol reflectance as well as a linear increase with increasing surface reflectance. The chosen values represent a high optical depth regime with both the sun and sensor directly overhead and result in a change of 0.006 per 1% change in mean aerosol reflectance. Figure 7(b) represents the same situation but at a solar zenith angle of 30°, a typical value encountered by the QuickBird sensor, and results in a sensitivity of 0.005 change in AOD per 1% change in mean aerosol reflectance.

4.   Sensor (Viewing) Zenith Angle

The viewing zenith angle term in Eq. (34) serves to correct for off nadir viewing by the sensor. To quantify this influence, again, it is useful to recast Eq. (34) by combining multiple constants into one single constant where possible prior to carrying out the partial differentiation. As such, Eq. (34) will be recast into the following:

$$\delta = \left(\frac{\mu_0 \mu}{\mu_0 + \mu} \right) c_4 .$$

(44)

where c_4 is defined as:

$$c_4 = \ln \left[\left(\frac{r_s}{1 - r_s \bar{r}} \right) \left(\frac{\mu_0 F_0}{\pi L_d} \right) \right].$$

(45)

Using the quotient rule for differentiation, the partial differential of optical depth with respect to viewing zenith angle is:

$$\frac{\partial \delta}{\partial \mu} = \left(\frac{\mu_0}{\mu_0 + \mu} \right)^2 c_4 , \text{ or}$$

$$\frac{\partial \delta}{\partial \mu} = \left(\frac{\mu_0}{\mu + \mu_0} \right)^2 \ln \left[\left(\frac{r_s}{1 - r_s \bar{r}} \right) \left(\frac{\mu_0 F_0}{\pi L_d} \right) \right].$$

(46)

35

Figure 8 shows Eq. (46) evaluated at solar zenith angles of (a) 0° and (b) 30° for a range of sensor zenith angles and curves representing a range of unshaded/shaded radiance differences. Surface reflectance and mean aerosol reflectance values of 1.0 and 0.12 respectively were used to maximize the argument of the natural log in Eq. (46). Only this maximum value was used when evaluating Eq. (46) for the range of zenith angles and unshaded/shaded radiance differences. It can be seen that the rate of change in AOD with a 90° change in sensor zenith angle increases nearly linearly with the cosine of the sensor zenith angle. Likewise, one can see an increase between Figs. 8(a) and 8(b) indicating an increase in the rate of change in AOD with a 90° change in sensor zenith angle with increasing solar zenith angle. Figure 8 also shows that an increase in the unshaded/shaded radiance difference results in a decrease in the rate of change in AOD with a 90° change in sensor zenith angle. As with surface reflectance and mean aerosol reflectance, Eq. (46) represents a rate of change in AOD over the full range of zenith angles. Unlike surface reflectance and mean aerosol reflectance, the cosine function does not vary uniformly over the full range of zenith angles. As such, the rate of change in AOD with a 90° change in sensor zenith angle will be normalized to the rate of change of AOD with a 1° change in sensor zenith angle for sensor zenith angles ranging between 20° and 25° and a solar zenith angle of 30°. Again, in an effort to identify the maximum value of Eq. (46), an unshaded/shaded radiance difference of 10 W m^{-2} sr^{-1} nm^{-1} will be used.
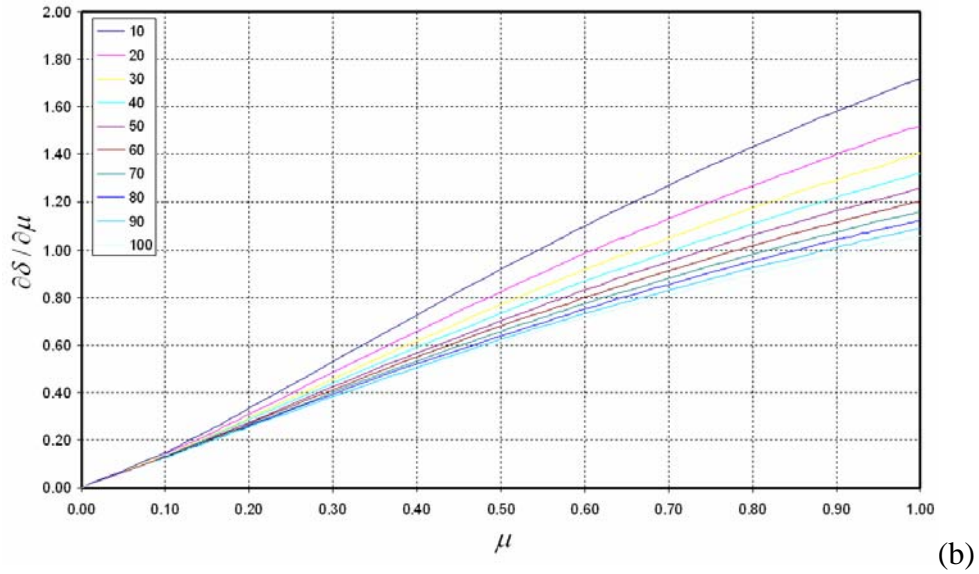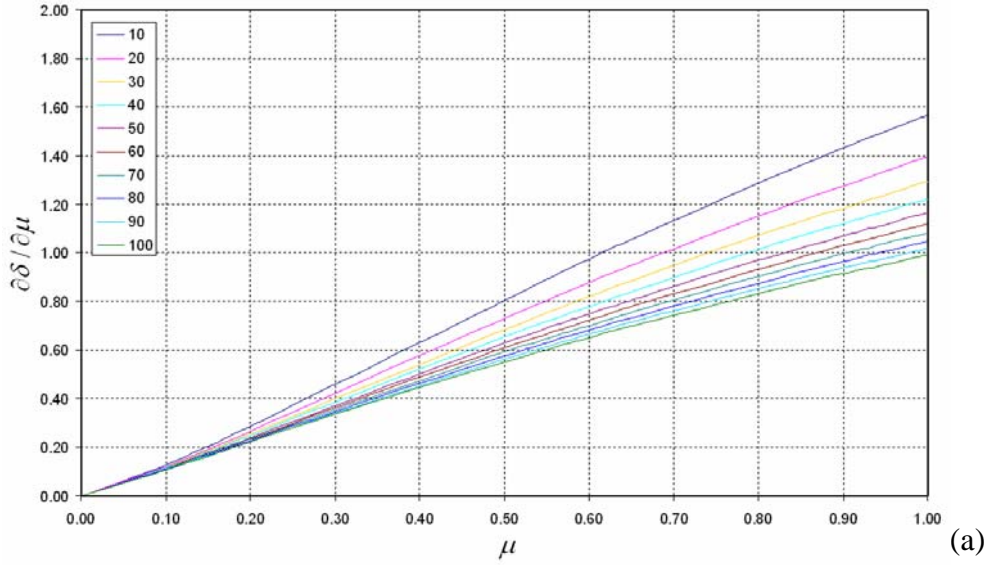
Figure 8.   The change in AOD with a change of 90° change in sensor zenith angle as a function of sensor zenith angle for solar zenith angles of (a) 0° and (b) 30°, with curves for unshaded/shaded radiance values ranging from 10 to 100 (for surface reflectance and mean aerosol reflectance values of 1.0 and 0.12 respectively).

As before, the goal is to capture the coarsest sensitivity associated with each parameter by maximizing the value of Eq. (46). For typical QuickBird values of sensor zenith angles of less than 25° and a solar zenith angle of 30° as in Fig. 8(b), the

maximum rate of change in AOD with a 1° change in sensor zenith angle is 0.0001 for an unshaded/shaded radiance difference of 10.

5.   Solar Zenith Angle

The effects of the solar zenith angle variation on retrieved aerosol optical depth using Eq. (34) are similar to those of viewing zenith angle. The solar and viewing zenith angles play the same mathematical role in the first term on the RHS of Eq. (34). Additionally, solar zenith angle also plays a role in the third term on the RHS of Eq. (34) by modifying extraterrestrial spectral solar irradiance. To quantify this influence, again, it is useful to recast Eq. (34) by combining multiple constants into one single constant where possible prior to carrying out the partial differentiation. As such, Eq. (34) will be recast into the following:

$$\delta = \left(\frac{\mu_0 \mu}{\mu + \mu_0} \right) \ln \left(c_5 \mu_0 \right), \tag{47}$$

where c_5 is defined as:

$$c_5 = \left(\frac{r_s}{1 - r_s \overline{r}} \right) \left(\frac{F_0}{\pi L_d} \right). \tag{48}$$

Using the product, quotient, and chain rules for differentiation, the partial differential of optical depth with respect to solar zenith angle is:

$$\frac{\partial \delta}{\partial \mu_0} = \frac{\mu}{\mu_0 + \mu} + \left(\frac{\mu}{\mu_0 + \mu} \right)^2 \ln \left(c_5 \mu_0 \right), \text{ or}$$

$$\frac{\partial \delta}{\partial \mu_0} = \frac{\mu}{\mu_0 + \mu} \left\{ 1 + \left(\frac{\mu}{\mu_0 + \mu} \right) \ln \left[\left(\frac{r_s}{1 - r_s \overline{r}} \right) \left(\frac{\mu_0 F_0}{\pi L_d} \right) \right] \right\}. \tag{49}$$

Figure 9 shows Eq. (49) evaluated at sensor zenith angles of (a) 0° and (b) 25° for a range of solar zenith angles and curves representing a range of unshaded/shaded radiance differences. Surface reflectance and mean aerosol reflectance values of 1.0 and 0.12 respectively were used to maximize the argument of the natural log in Eq. (49). Only this maximum value was used when evaluating Eq. (49) for the range of zenith

angles and unshaded/shaded radiance differences. It can be seen that the rate of change in AOD with a 90° change in solar zenith angle increases with increasing solar zenith angle. Likewise, one can see an increase between Figs. 9(a) and 9(b) indicating an increase in the rate of change in AOD with a 90° change in solar zenith angle with increasing sensor zenith angle.   Figure 9 also shows that an increase in the unshaded/shaded radiance difference results in a decrease in the rate of change in AOD with a 90° change in solar zenith angle. As with surface reflectance and mean aerosol reflectance, Eq. (49) represents a rate of change in AOD over the full range of zenith angles. Unlike surface reflectance and mean aerosol reflectance, the cosine function does not vary uniformly over the full range of zenith angles. As such, the rate of change in AOD with a 90° change in solar zenith angle will be normalized to the rate of change of AOD with a 1° change in solar zenith angle for solar zenith angles ranging between 30° and 35° and a sensor zenith angle of 25°. Again, in an effort to identify the maximum value of Eq. (49), an unshaded/shaded radiance difference of 10 W m^{-2} sr^{-1} nm^{-1} will be used.
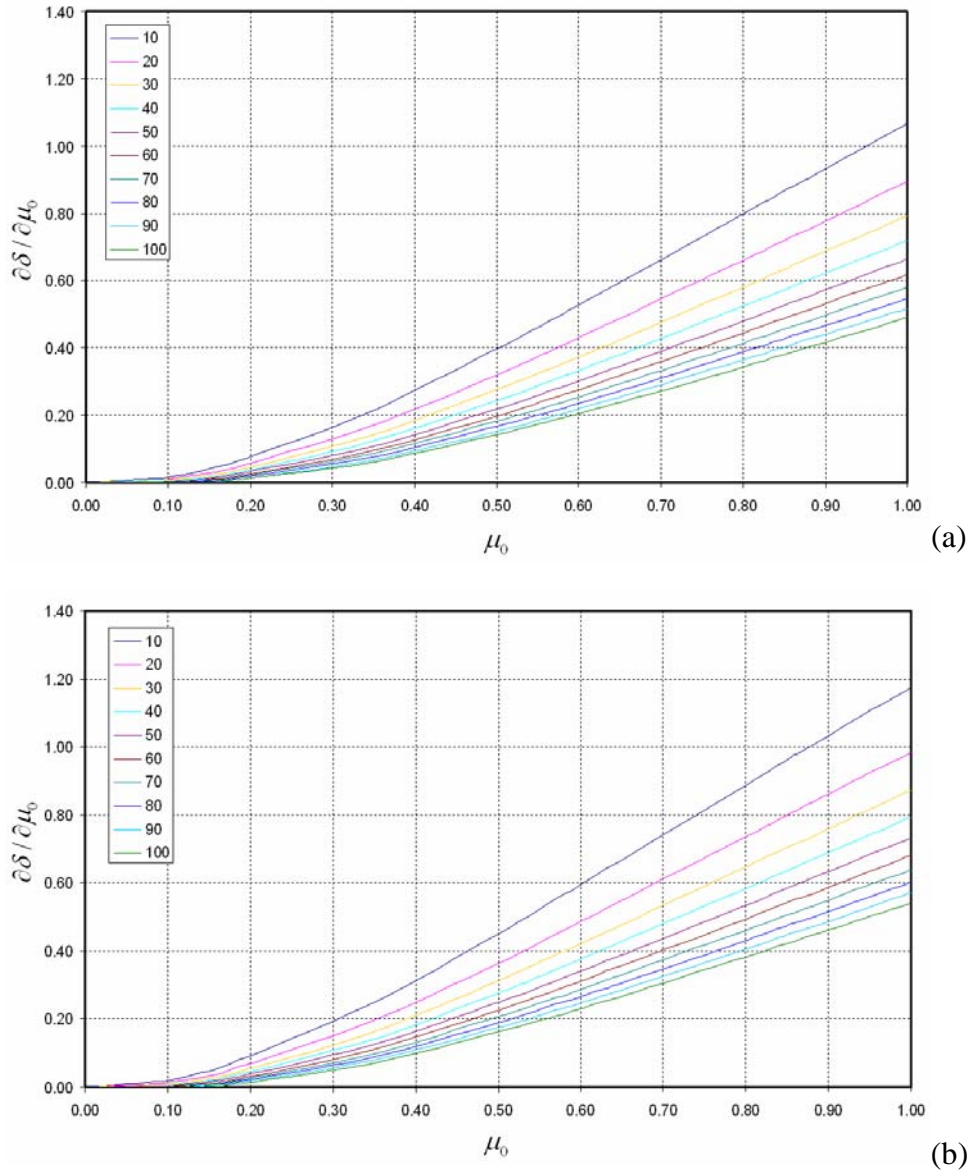
Figure 9.   The change in AOD with a change of 90° change in solar zenith angle as a function of solar zenith angle for sensor zenith angles of (a) 0° and (b) 25°, with curves for unshaded/shaded radiance values ranging from 10 to 100 (for surface reflectance and mean aerosol reflectance values of 1.0 and 0.12 respectively).

As before, the goal is to capture the coarsest sensitivity associated with each parameter by maximizing the value of Eq. (49). For typical QuickBird values of solar zenith angles between 30° and 35° and a sensor zenith angle as 25° as in Fig. 9(b), the

maximum rate of change in AOD with a 1° change in solar zenith angle is 0.0001 for an unshaded/shaded radiance difference of 10.

C.   SENSITIVITY SUMMARY OF THE GOVERNING EQUATION

A sensitivity analysis of Eq. (34), the governing equation, was undertaken to determine the utility of the Shadow method over a wide range of conditions. Table 2 lists the maximum rate of change in AOD for a unit change in each parameter and the corresponding rate of change under average conditions.

Table 2.   Sensitivity of Eq. (34) to the key parameters under extreme conditions (maximum) and average conditions (average) in the form of change in AOD per unit change in the parameter.

Parameter	Maximum AOD Sensitivity (per unit change in parameter)	Average AOD Sensitivity (per unit change in parameter)
Unshaded/shaded radiance difference	-0.05 per W m^{-2} sr^{-1} nm^{-1}	-0.04 per W m^{-2} sr^{-1} nm^{-1}
Surface Reflectance	0.05 per 1% change in reflectance	0.04 per 1% change in reflectance
Mean Aerosol Reflectance	0.006 per 1% change in reflectance	0.002 per 1% change in reflectance
Solar Zenith Angle	0.0001 per 1° change between 30°-35°	0.0001 per 1° change between 30°-35°
Sensor Zenith Angle	0.0001 per 1° change between 24°-25°	0.0001 per 1° change between 24°-25°

One can readily see that the unshaded/shaded radiance difference and surface reflectance have the greatest effect on retrieved AOD. The change in AOD per unit change of unshaded/shaded radiance difference and surface reflectance are of the same magnitude, however the former has an inverse relationship with change in AOD while the latter has a direct relationship to change in AOD. In both cases, the change in AOD per unit change in mean aerosol reflectance is an order of magnitude smaller than that of unshaded/shaded radiance difference and surface reflectance. Likewise, the change in

AOD per unit change in solar and sensor zenith angle is two orders of magnitude smaller than that of unshaded/shaded radiance difference and surface reflectance. This means that the Shadow method is quite responsive to changes in unshaded/shaded radiance difference and surface reflectance, while quite invariant with respect to mean aerosol reflectance, solar zenith angle, and sensor zenith angle. Additionally, the sensitivities for unshaded/shaded radiance difference and surface reflectance presented in Table 2 are well above the uncertainties for those same parameters presented in the next chapter illustrating that the required signal to discriminate between AOD changes is at least an order of magnitude greater than the uncertainty associated with that signal.

D.   SENSITIVITY TO CLOUD FRACTION AND PROXIMITY

Traditionally, companies collecting and selling commercial high-spatial resolution satellite imagery have avoided collecting imagery in the presence of clouds. With a focus on surface feature identification and geospatial applications, this only makes sense. However, Koelemeijer *et al.* (2002) estimates monthly effective cloud fraction to be between 0.2 and 0.5 globally depending on season and latitude, which can make avoiding clouds difficult, if not impossible, in some areas. As data compression and storage technology improves in the future and the number of high-resolution satellites increase, the frequency and spatial coverage of high-resolution imagery will increase as will the likelihood of cloud contamination. DigitalGlobe, the owner of the QuickBird satellite, will currently distribute imagery with 20% or less cloud cover in the scene, although more or less stringent cloud screening can be requested by the customer (DigitalGlobe 2005b). Repeat imaging of an area can minimize the impact of cloud cover in most areas if the surface features to be imaged are not transient. For atmospheric applications, such as regional air quality studies, time averaging through repeat imaging defeats the purpose of the studies. In such cases, the impact of clouds must be dealt with explicitly.

High spatial-resolution satellite imagery has the advantage of being able to resolve most clouds to their smallest scales unlike many of today's operational meteorological satellites. With the problem of cloud identification largely resolved by visual inspection, the specific impact of cloud fraction over the full scene and proximity

to the retrieval site for the shadow-based AOD retrieval method must be addressed. Cumuliform, stratiform, and cirriform clouds types will be addressed separately based on the unique impacts of each on the scene.

1.   Impacts of Cumuliform Clouds on the Shadow-based AOD Retrieval

The impacts of cumulus cloud amount and spacing on high-resolution imagery were investigated by Wen *et al.* (2001) using Landsat 7 Enhanced Thematic Mapper Plus (ETM+) data over the Southern Great Plains Atmospheric Radiation Measurement (SGP ARM) site. Focusing mainly on fair weather cumulus with variable spacing, Wen *et al.* (2001) tried to observe the effects of clouds on apparent path radiance in cloud free areas and then parameterize those effects. The term "apparent reflectance" as coined by Cahalan *et al.* (2001), or "apparent path radiance" as used by Wen *et al.* (2001), refers to the top of the atmosphere reflectance or radiance as observed by the sensor and is made up of the clear (cloud-free) path reflectance or radiance and the diffuse contribution from the cloud. Both Cahalan *et al.* (2001) and Wen *et al.* (2001) found that apparent path radiance for clear areas within a cumulus field was significantly enhanced by clouds in close proximity. This adjacency effect, or brightening of darker pixels by scatters in near-by bright pixels, severely impacts traditional path radiance AOD retrieval techniques, such as the dark object method. A schematic of adjacency effects due to (a) bright surfaces, (b) clouds, and (c) small scale bright features are shown in Fig. 10. Wen *et al.* (2001) was concerned with the effects seen in Fig. 10(b) and looked at the issues of cloud fraction and proximity separately.

(a)

(b)

(c)
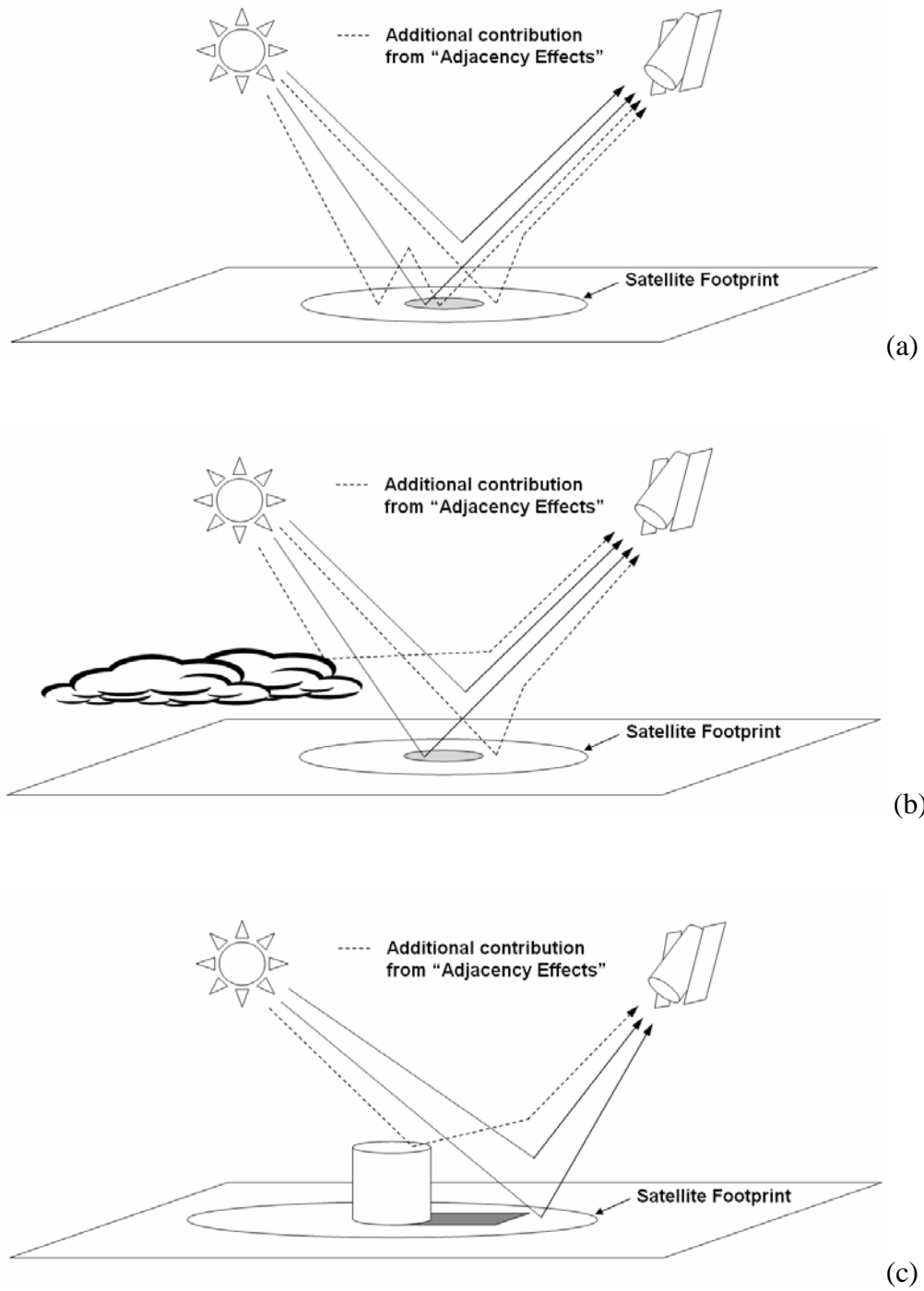
Figure 10.   Examples of the "adjacency effect," or brightening of dark pixels due to adjacent bright pixels due to (a) surrounding areas of high surface reflectance, (b) scattering from clouds, and (c) small, highly reflective objects, such as the top of a building, within the field of view.

44

a. *Cloud Fraction Impacts on Apparent Path Radiance*

Wen *et al.* (2001) quantified the impacts of cloud fraction on apparent path radiance using the correlation of ETM+ band 1 (0.49 µm) and band 7 (2.2 µm) for subimages representing clear sky and increasing cloud fractions of 0.17, 0.5, 0.92. ETM+ band 1 is very sensitive to scattering by aerosol particles while band 7, in the mid-IR, is largely insensitive to aerosol particles. The results of their investigation are displayed in Fig. 11. With apparent reflectance for band 1 (0.49 µm) on the y-axis and apparent reflectance for band 7 (2.2 µm) on the x-axis, a straight line is fit through the lower envelope of the correlation. The intercept of this line provides the atmospheric path radiance for clear sky conditions and includes all atmospheric influences except clouds. As cloud fraction increases, the apparent path radiance also increases. In this case, the increase in apparent path radiance ranges from 0.005 for a cloud fraction 0.17 to 0.03 for a cloud fraction of 0.92.
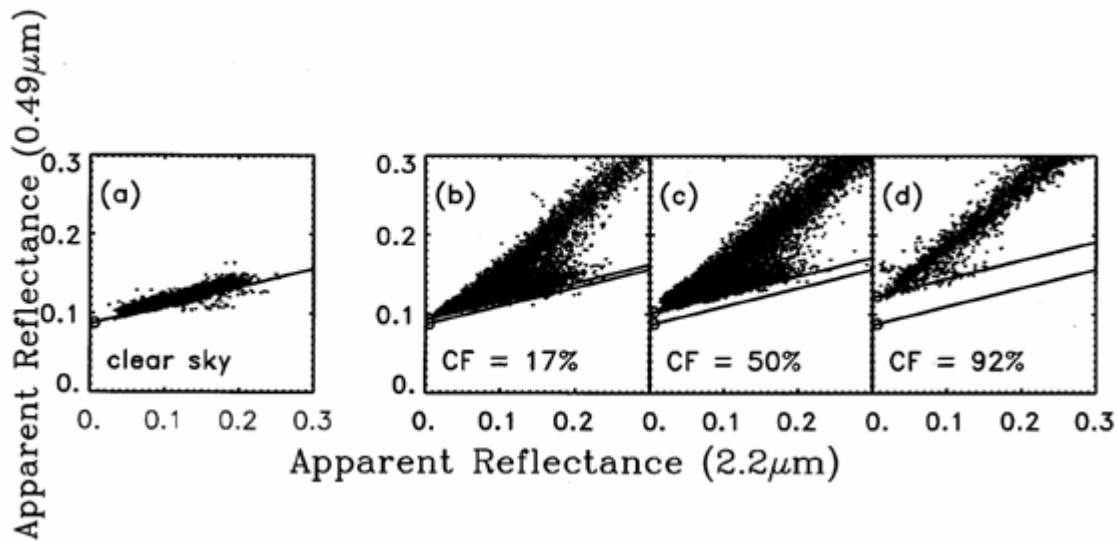
Figure 11.   The relation between the Band 1 and Band 7 for four subimages of a Landsat 7 ETM+ image of the Southern Great Plains Atmospheric Radiation Measurement (SGP ARM) site: (a) clear sky and (b)-(d) cloudy subimages with increasing cloud fraction (CF). The intercept of zero mid-IR reflectance determines the path radiance (for completely clear sky) and apparent path radiance (for clear patches in the cumulus cloud field), respectively. The line used to determine path radiance for clear sky in (a) is also plotted in cloudy cases ((b) through (d)) as a reference. (after Wen *et al.* (2001))

The implications of this for the shadow-based AOD retrievals using QuickBird are significant. While clouds are typically avoided, DigitalGlobe will distribute imagery with a cloud fraction of up to 0.2 as a matter of routine and greater than 0.2 at the customer's request. The presence of additional path reflectance across the scene due to cloud fraction will not impact the unshaded/shaded radiance difference as both areas will be affected equally and the difference will remain unchanged. The determination of surface reflectance using the unshaded area of the target will be affected however. Section B, Subsection 2 of this chapter shows that the sensitivity in final AOD to the surface reflectance is a 0.04 increase in AOD with a 1% increase in surface reflectance. If the bias determined by Wen *et al.* (2001) for Landsat ETM+ imagery holds for QuickBird imagery, a high bias of 0.02 to 0.12 in final AOD is possible for cloud fractions between approximately 0.2 and 0.9. For this reason, scenes with cloud fraction greater than 0.2 are best avoided. Future efforts will be necessary to quantify the impacts of cloud fractions greater than 0.2 for each sensor using the shadow-based AOD retrieval method.

b.   *Cloud Proximity Impacts on Path Radiance*

Wen *et al.* (2001) next investigated the impact of cloud proximity on apparent path reflectance using Landsat ETM+ bands 1 and 3, centered at 0.49 μm and 0.66 μm respectively. The results of this investigation are shown as Fig. 12, a graph of apparent path radiance (in reflectance units) for bands 1 and 3 as a function of mean cloud-free distance in kilometers. For this investigation, mean cloud-free distance is defined as the distance from a clear pixel to the nearest cloud along the principal plane. The authors chose this convention based on the rationale that the principal plane (that in line with the sun) is where the brightest reflectances occur will contribute the most to apparent path radiance (or reflectance). An exponential fit (solid line in Fig. 12) to the apparent path radiance for bands 1 and 3 as a function of mean cloud-free distance show decay to an asymptotic apparent path radiance. One can readily see that this asymptotic apparent radiance value is still approximately 0.005, or 0.5% reflectance, above that of the clear-sky apparent path radiance shown as the dashed line.
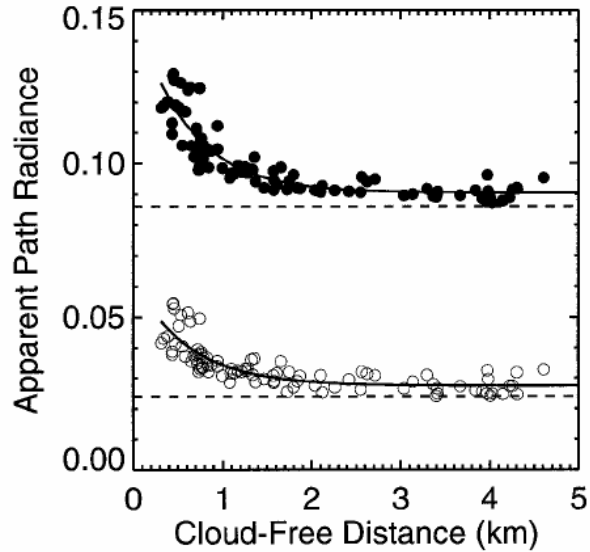
Figure 12.   The apparent path radiance for ETM+ band 1 (solid circles) and band 3
              (open circles) as a function of mean cloud-free distance, as defined above
              (after Wen *et al.* (2001)).

As with cloud fraction, this apparent path radiance has no effect on the unshaded/shaded radiance difference in the shadow-based AOD retrieval method, as both areas are affected equally by the diffuse field. The surface reflectance, however, can again be biased by approximately 0.5% just by the presence of cloud and as much as 3% for the red channel and 4% or more for the blue channel for clouds within 0.5 kilometers. Based on the sensitivity of the shadow-based AOD method to changes in surface reflectance, this high bias in surface reflectance equates to errors in retrieved AOD of 0.12 in the red to 0.16 or greater in the blue. The best fit lines for apparent path radiance in Fig. 12 approaches their asymptotic values by approximately two kilometers. This provides starting cloud edge stand-off criteria for target sites.   Wen *et al.* (2001) characterize the vertical extent of the fair weather cumulus clouds as 0.5 kilometers thick with bases at approximately 0.5 kilometers AGL. While clouds of greater vertical extent or optical depth are not considered by Wen *et al.* (2001), they do acknowledge that such changes could impact the apparent path radiance. By physical reasoning alone, the impacts of increased vertical extent are likely to include an increase in the asymptotic apparent path radiance as well as an increase in the mean cloud-free distance that apparent path radiance approaches the asymptotic value.

47

c.   *Vertical Cloud Development Impacts on Apparent Cloud Fraction*

Wen *et al.* (2001) considered the impacts of cloud fraction and proximity due to fair weather cumulus clouds on the apparent reflectance of Landsat ETM+ imagery.   Vertically developed cumulus clouds present an additional problem with determining cloud fraction. When viewed at nadir (sensor zenith angle of 0°), vertically developing cumulus clouds can cover a relatively small area. When viewed off nadir (sensor zenith angle greater than 0°), the vertically developing cloud presents a larger target as the vertical extent of the cloud comes within the field of view of the satellite. The increase in apparent cloud fraction can increase apparent reflectance across the scene if viewed within 90° of the principal solar plane and decrease apparent reflectance if viewed at relative azimuths to the principal solar plane of greater than 90°. To gauge the increase in cloud fraction as a function of sensor zenith angle, a notional cloud with a base of 1 km^2 and varying aspect ratio (height/width) is considered. This is best shown by determining the sensor zenith angle required for an effective doubling of the apparent cloud area of the cloud. If the area covered by the cloud doubles, so does the cloud fraction attributed to that cloud. The results shown in Fig. 13 indicate that for the most vertically developed clouds, a sensor zenith angle of only 5° is necessary to effectively double the apparent cloud fraction. This result is independent of cloud base height since the area viewed under the cloud and the area behind the cloud lost from view at non-zero sensor zenith angles grow proportionally. For all practical purposes, however, imagery collection in areas of vertically developing cumulus clouds rarely results in useable imagery due to the high cloud fraction. Such images would be unsuitable for the shadow-based AOD retrieval method.
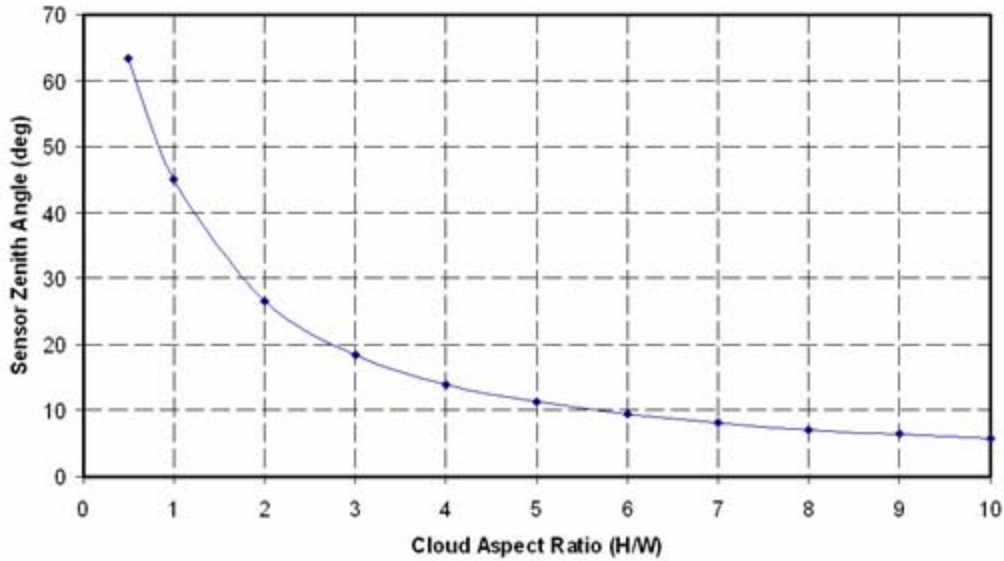
Figure 13.   Minimum sensor zenith angle required for a doubling of the apparent cloud area as a function of cloud aspect ratio (height/width) for a notional vertically developing cumulus cloud.

2.   Impacts of Stratiform Clouds on the Shadow-based AOD Retrieval

No specific studies of stratiform clouds on the apparent path radiance in high resolution imagery could be found. The horizontal extent of typical stratiform clouds precludes imaging with high resolution satellites due to the small spatial extent of the image. Also precluded is the opportunity to image between cloud elements, as with cumuliform clouds, due the continuous, blanket-like nature of stratiform clouds. Imagery showing the edge of the cloud field and some amount of cloud-free area may lend itself to the shadow-based AOD retrieval method, however. Such images would likely suffer the same impacts to apparent path radiance as seen with the fair weather cumulus clouds described in the preceding section.

3.   Impacts of Cirriform Clouds on the Shadow-based AOD Retrieval

The presence of thin cirrus clouds has long plagued satellite-based AOD retrievals. Their detection over highly reflective surfaces can be even more troublesome. Thin cirrus can present two problems in QuickBird imagery. First, large regions of thin cirrus over the QuickBird image area will cause an increase in the apparent reflectance of

the scene resulting in a high bias to the retrieved AOD. Second, thin cirrus contamination covering only part of the scene will bias only some of the retrievals across the image and bias the image mean AOD. Remer *et al.* (2005) discusses detection of thin cirrus clouds in MODIS imagery using channels sensitive to ice absorption in the at wavelengths greater than 1.0 μm in combination with reflectance tests in the near-infrared. Motta (2006) discusses operational identification of thin cirrus by looking at the 10.7 micrometer channel minus the 12.0 micrometer channel in GOES Imager data. QuickBird only has one near-infrared channel and all channels cover only the visible and near-infrared region of the spectrum below 1.0 μm, and therefore has no means of thin cirrus detection. Identification of thin cirrus from spatially and temporally collocated meteorological satellite imagery, such as MODIS (polar orbiting) or GOES (geostationary), would be necessary if it is to be avoided. An example of MODIS thin cirrus detection using the 1.38 micrometer channel over a highly reflective surface is shown in Fig. 14.
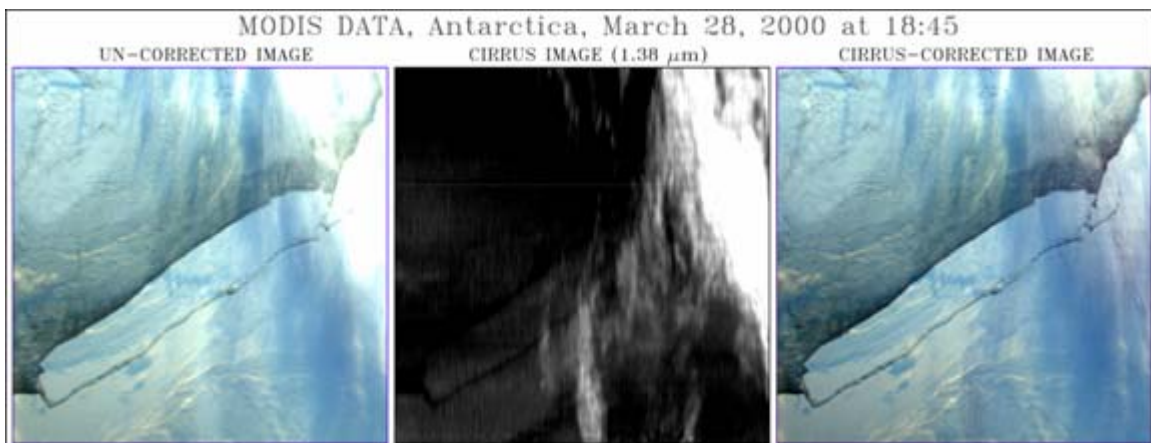
Figure 14. Thin cirrus over the highly reflective Ross Ice Shelf as shown in the RGB image (first image), identified using the MODIS 1.38 μm channel (second image), and the corrected RGB image (third image) (courtesy of NASA).

V.   UNCERTAINTY ANALYSIS

A.   GOVERNING EQUATION

The governing equation for retrieving total optical depth, δ_0, from satellite-measured radiances was introduced as Eq. (34) in Chapter III. The uncertainties associated with Eq. (34) will now be evaluated. Using standard error analysis techniques as presented in Taylor (1997), uncertainties due to surface reflectance, r_s, mean aerosol reflectance, $\bar{r}$, and the unshaded/shaded radiance difference, L_d, will be evaluated. It is assumed that solar and viewing zenith angles, μ_0 and μ respectively, and spectral solar irradiance, F_0, are constant and contain negligible uncertainty.

B.   UNCERTAINTY ANALYSIS PROCEDURE

The uncertainty in total optical depth as determined by Eq. (34) can be described by summing the uncertainty associated with each term in quadrature assuming the errors for each are independent of the others and random in nature. This uncertainty can be described as:

$$\Delta\delta = \sqrt{\left(\left|\frac{\partial\delta}{\partial r_s}\right|\Delta r_s\right)^2 + \left(\left|\frac{\partial\delta}{\partial \bar{r}}\right|\Delta\bar{r}\right)^2 + \left(\left|\frac{\partial\delta}{\partial\Delta L}\right|\Delta L_d\right)^2}\ ,\qquad(50)$$

where the LHS represents the total uncertainty in optical depth and the RHS represents the sum in quadrature of the uncertainty associated with each term as described by the product of the partial derivative of Eq. (34) with respect to the individual term and the uncertainty associated with that term. As in Chapter IV, it is useful to recast Eq. (34) by combining multiple constants into one single constant where possible prior to carrying out the partial differentiation. As such, Eq. (34) will be recast into the following form for the first two differentiations:

$$\delta = c_1 \ln\left[c_2\left(\frac{r_s}{1-r_s\bar{r}}\right)\right],\qquad(51)$$

where the constants c_1 and c_2 represent:

$$c_1 = \frac{\mu_0 \mu}{\mu_0 + \mu} \tag{52a}$$

$$c_2 = \frac{\mu_0 F_0}{\pi L_d}. \tag{52b}$$

Using the quotient, power and chain rules for differentiation, the partial differentials of optical depth with respect to surface reflectance and mean aerosol reflectance are:

$$\frac{\partial \delta}{\partial r_s} = \frac{c_1}{r_s \left(1 - r_s \overline{r}\right)}, \text{ and} \tag{53}$$

$$\frac{\partial \delta}{\partial \overline{r}} = \frac{c_1 r_s}{\left(1 - r_s \overline{r}\right)}. \tag{54}$$

Again, it is useful to recast Eq. (34) in terms of other constants to carry out the differentiation with respect to the unshaded/shaded radiance. Eq. (34) can be rewritten as:

$$\delta = c_1 \ln\left[c_3 \left(\frac{1}{L_d}\right) \right] \tag{55}$$

where c_1 remains the same as defined in Eq. (52a) and c_3 is defined as:

$$c_3 = \left(\frac{r_s}{1 - r_s \overline{r}}\right)\left(\frac{\mu_0 F_0}{\pi}\right). \tag{56}$$

Using the power and chain rules for differentiation, the partial differential of optical depth with respect to the unshaded/shaded radiance difference is:

$$\frac{\partial \delta}{\partial L_d} = -\frac{c_1}{L_d}. \tag{57}$$

Now, substituting Eqs. (53), (54), and (57) into Eq. (36), the uncertainty in optical depth can be described by:

$$\Delta\delta = \sqrt{\left(\left|\frac{c_1}{r_s\left(1-r_s\overline{r}\right)}\right|\Delta r_s\right)^2 + \left(\left|\frac{r_s c_1}{\left(1-r_s\overline{r}\right)}\right|\Delta\overline{r}\right)^2 + \left(\left|-\frac{c_1}{L_d}\right|\Delta L_d\right)^2} \qquad (58)$$

where the Δ terms on the RHS represent the uncertainties of the individual terms.

1.   Uncertainty due to Measured Radiance Values

Before total uncertainty estimates can be determined, a measure of uncertainty for each measured term must be made. First, the uncertainty for the difference in observed unshaded/shaded radiance difference can be determined from the uncertainty in any individual radiance measurement within each QuickBird channel. The maximum uncertainty for each QuickBird channel is given in Table 3 as Noise Equivalent Radiance (NER).

Table 3.   Noise Equivalent Radiance (NER) for QuickBird channels (adapted from DigitalGlobe 2005a).

Band	Noise Equivalent Radiance ($W\ m^{-2}\ sr^{-1}\ \mu m^{-1}$)
Blue	0.2359
Green	0.1453
Red	0.1785
Near-Infrared	0.1353
Panchromatic	0.1620

Because the term of interest is the difference between two radiances, the total uncertainty due to the radiance difference term is the sum of the uncertainties for each radiance measurement or two times the uncertainty for an individual radiance measurement within each channel. Therefore, the uncertainty for the radiance difference term within each channel is twice the value for each channel found in Table 3. These

uncertainties are found to make the largest contribution to the total uncertainty in retrieved total optical depth and tend to be invariant with increasing surface reflectance as is indicated by the purple and green solid lines in Figs. 17 through 21. Uncertainty due to the difference in measured radiance is considered the first order uncertainty.

2.   Uncertainty due to Surface Reflectance

The uncertainty due to surface reflectance must be calculated based on the uncertainty of the unshaded radiance measurement used to determine top of the atmosphere (TOA) reflectance. This TOA reflectance is used as surface reflectance for the initial calculation of aerosol optical depth and is defined as:

$$r_s = \frac{\pi L_{unshaded}}{\mu_0 F_0},$$
(59)

where $L_{unshaded}$ is the unshaded radiance used in the radiance difference, L_d, and F_0 is the appropriate spectral solar irradiance for each QuickBird channel, and μ_0 is the cosine of the solar zenith angle. The uncertainty for surface reflectance may then be calculated as:

$$\Delta r_s = \left| \frac{\partial r_s}{\partial L} \right| \Delta L \text{, or}$$

$$\Delta r_s = \frac{\pi}{\mu_0 F_0} \Delta L.$$
(60)

The resulting surface reflectance uncertainties for each QuickBird channel are listed in Table 4. The dark blue line in Figs.17 through 21 indicates that uncertainty in total optical depth due to uncertainty in surface reflectance decreases with increasing surface reflectance. This likely results from the fact that the uncertainty in surface reflectance is a smaller percentage of surface reflectance as surface reflectance increases. The uncertainties associated with surface reflectance are not as large as those associated

with the difference in measured radiance, and, as such, are considered second order uncertainties.

Table 4.   Uncertainties in surface (TOA) reflectance based on QuickBird radiance measurement uncertainties.

Band	Surface (TOA) Reflectance Uncertainty
Blue	3.82×10^{-4}
Green	2.46×10^{-4}
Red	3.36×10^{-4}
Near-Infrared	3.87×10^{-4}
Panchromatic	3.38×10^{-4}

Among the uncertainties in the surface reflectance is the assumption of a Lambertian surface. The Lambertian assumption dictates that a surface's reflectance is independent of viewing angle. While this assumption is routinely used for satellite AOD retrievals, the unique nature of high-resolution commercial satellite imagery requires that the assumption be revisited. Highly varied and complex surface types are explicitly seen in high resolution imagery when such variability is averaged over one square kilometer or more in most environmental satellite sensors. While the Lambertian assumption still typically holds, the opportunity for specular reflection is increased. Specular reflection results when highly reflective surfaces reflect the direct sun light in a "mirror-like" fashion and is highly dependent on solar/sensor geometry. Such reflections would cause large overestimates of the surface reflectance and artificially increase the unshaded/shaded radiance difference in the shadow-based AOD retrieval method. Although such specular reflections are possible, they can be avoided in four ways: 1) inspecting imagery for solar/sensor geometry favorable to specular reflection, 2) restricting retrievals to some maximum surface reflectance value (such as 0.75),

3) discarding extremely low retrieved AODs due to exceptionally high unshaded/shaded radiance differences, 4) through visual inspection of the imagery for specular reflections.

### 3.	Uncertainty due to Mean Aerosol Reflectance

Determining the uncertainty due to the mean aerosol reflectance is a more difficult problem due to the complicated nature of the resulting equation. Recall that Eq. (27), the definition for the mean aerosol reflectance, is:

$$\bar{r} = \frac{1}{\pi}\int\limits_0^{2\pi}\int\limits_0^1\int\limits_0^{2\pi}\int\limits_0^1 \frac{\omega\mu'\mu''}{(\mu'+\mu'')}\left(\frac{P(\Theta)}{4\pi}\right)\left(1-e^{-\delta\left(\frac{1}{\mu'}+\frac{1}{\mu''}\right)}\right)d\mu'd\phi'd\mu''d\phi'' , \quad (27)$$

where Θ represents the scattering angle based on the source and resultant zenith and azimuth angles. The uncertainty of the mean aerosol reflectance term, $\Delta\bar{r}$, must be determined prior to determining the mean aerosol reflectance contribution to the total aerosol optical depth uncertainty. This uncertainty is determined using substitution of realistic values to determine a range of uncertainty due to the resulting unsolvable partial differential equation using the partial derivative method above.

The uncertainty in mean aerosol reflectance due to uncertainty in the phase function can be determined using the Henyey-Greenstein phase function to capture the uncertainty due to the amount of forward scatter. The Henyey-Greenstein phase function is defined as:

$$P(\Theta) = \frac{1-g^2}{\left(1+g^2-2g\cos\Theta\right)^{3/2}} , \quad (61)$$

where Θ represents the scattering angle and g is the asymmetry parameter varying between 1 for fully forward scattering conditions, –1 for fully backscattering conditions, and 0 for isotropic conditions (Henyey and Greenstein, 1941). An asymmetry parameter of 0.65 ± 0.05 is assumed to approximate the forward scatter of most aerosols. Additionally, uncertainty in single scatter albedo, or ratio of scattering to total extinction,

is captured by determining the mean aerosol reflectance for the range of asymmetry parameters between 0.60 and 0.85 and single scatter albedo values of 0.9 and 1. The resulting maximum mean aerosol reflectance is 0.09 ± 0.02. This represents the maximum value and uncertainty for the mean aerosol reflectance term.

The Henyey-Greenstein phase function was chosen as a general approximation to a particulate aerosol phase function in the mean aerosol reflectance calculation due to its generic nature. Recent work in modeling the phase functions of non-spherical dust particles by Mishchenko *et al* (1997) and Wang *et al.* (2003) have produced more realistic phase functions than can be described by the Henyey-Greenstein approximation. A comparison of the Henyey-Greenstein phase function (asymmetry parameter = 0.65), the dust phase function from Mishchenko *et al.* (1997), and the T-matrix dust phase function developed by Wang *et al.* (2003) is shown in Fig. 15. To gauge the impact of the Henyey-Greenstein phase function approximation, mean aerosol reflectance (single scatter albedo = 0.94) using each phase function are plotted as a function of total optical depth in Fig. 15. It can be seen in Fig. 15 that the mean aerosol reflectance based on the T-matrix phase function is approximately 0.015 lower than that based on the Henyey-Greenstein phase function at higher total optical depths. Additionally, the mean aerosol reflectance based on the Mishchenko phase function is approximately 0.01 lower than that based on the Henyey-Greenstein phase function at higher total optical depths. Based on the sensitivity analysis presented in Chapter VI, a net low bias of 0.057 in retrieved AOD is possible for AODs above 0.8 using the Henyey-Greenstein phase function vice using a phase function developed for non-spherical aerosol particles. This shows that the use of the Henyey-Greenstein phase function only slightly overestimates mean aerosol reflectance when compared to mean aerosol reflectance based on non-spherical phase functions. As such, the use of the Henyey-Greenstein approximation is considered adequate for unknown aerosol types and combinations.
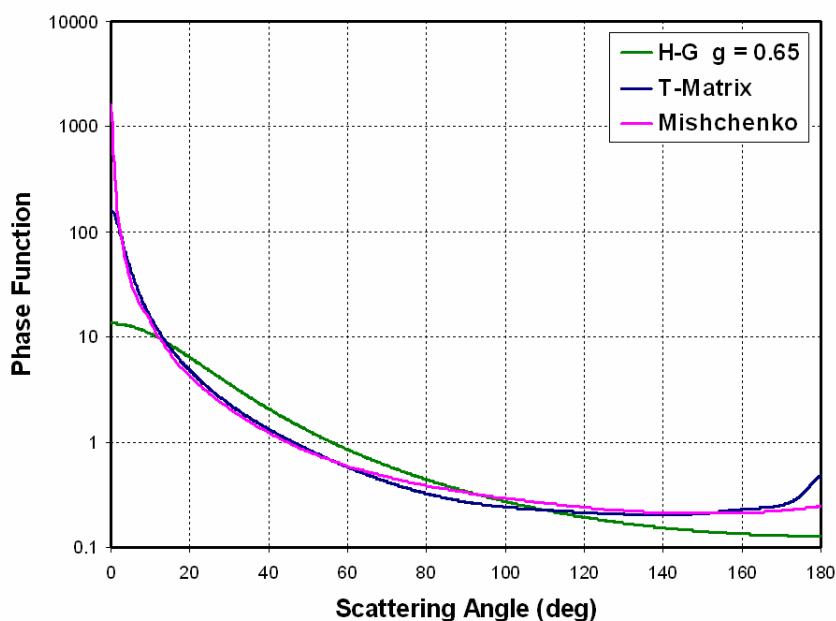
Figure 15.   Comparison of the Henyey-Greenstein phase function (g = 0.65), the T-matrix non-spherical dust phase function from Wang *et al.* (2003), and the non-spherical dust phase function from Mishchenko *et al.* (1997) as a function of scattering angle in degrees.
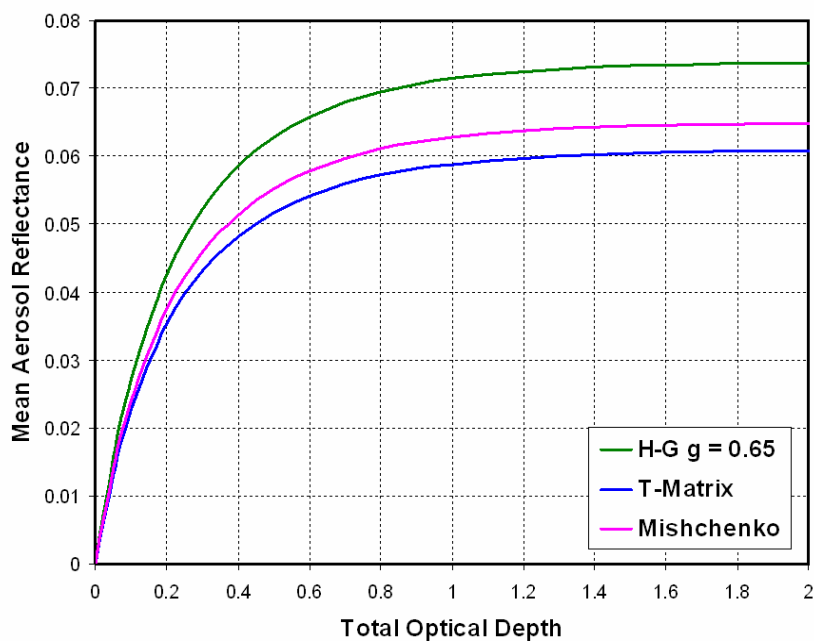
Figure 16.   Mean aerosol reflectance as a function of total optical depth based on the Henyey-Greenstein phase function (g = 0.65), the T-matrix non-spherical dust phase function from Wang *et al.* (2003), and the non-spherical dust phase function from Mishchenko *et al.* (1997) for a single scatter albedo of 0.94.

The mean aerosol reflectance is small, usually an order of magnitude or more, as compared to surface reflectance for bright targets under normal circumstances. The assumption that surface reflectance greatly exceeds mean aerosol reflectance allows the initial estimation total optical depth by ignoring mean aerosol reflectance. Ultimately, the contribution of mean aerosol reflectance to the total optical depth retrieval is small compared to that of surface reflectance. As shown in the Figs. 17 through 21 below, the uncertainty in total optical depth due to mean aerosol reflectance increases with increasing surface reflectance and is of the same order as the uncertainty due to surface reflectance or greater for surface reflectances above 0.15. The uncertainty due to mean aerosol reflectance only approaches the uncertainty due to unshaded/shaded radiance differences for surface reflectances of 0.5 and higher.

While the mean aerosol reflectance is small, its role in partitioning TOA reflectance into a surface and atmospheric component cannot be overstated. The sensitivity of the final AOD retrieval is an increase of 0.04 for every 0.01 increase in surface reflectance. Without the corrective step using mean aerosol reflectance, surface reflectance can be overestimated by as much as 0.1 and result in an error of 0.4 in AOD. The determination of mean aerosol reflectance from the initial estimation of total optical depth has an inherent high bias, typically of 0.01 to 0.03, that comes at the expense of surface reflectance. However, the low bias in AOD due to an underestimation by surface reflectance is much smaller, typically 0.04 to 0.12, as compared to the overestimation in the initial TOD of 0.1 to 0.4.

4. Total Uncertainty in Retrieved Aerosol Optical Depth

Total uncertainty estimates were determined for each QuickBird channel using Eq. (43), the sum of the individual uncertainties in quadrature, and a range of realistic values for the three main terms: surface reflectance, mean aerosol reflectance, and difference in observed radiances between unshaded and shaded areas. For this study, values of 0.05, 0.1, 0.2, 0.3, 0.4, and 0.5 were used for surface reflectance, values of 1, 2, 3, 4, 5, 7, 10, 20, and 30 were used for the radiance difference, and values of 0, 0.001, 0.01, 0.09, 0.1, 0.2, and 0.5 were used for mean aerosol reflectance. Results show that

59

total uncertainty in retrieved optical depth are most sensitive to the lower range of radiance differences, with the optical depth uncertainties approaching, and for some channels exceeding, 0.1. This implies that, as optical depth increases and the difference in radiances measured in unshaded and shaded areas decreases, the uncertainty associated with that optical depth also grows. For realistic radiance differences (e.g. 10 W m^{-2} sr^{-1} nm^{-1} or greater), uncertainty due to the uncertainties in the radiance difference are approximately ±0.04 or lower for all channels. See Figs. 17 through 21.
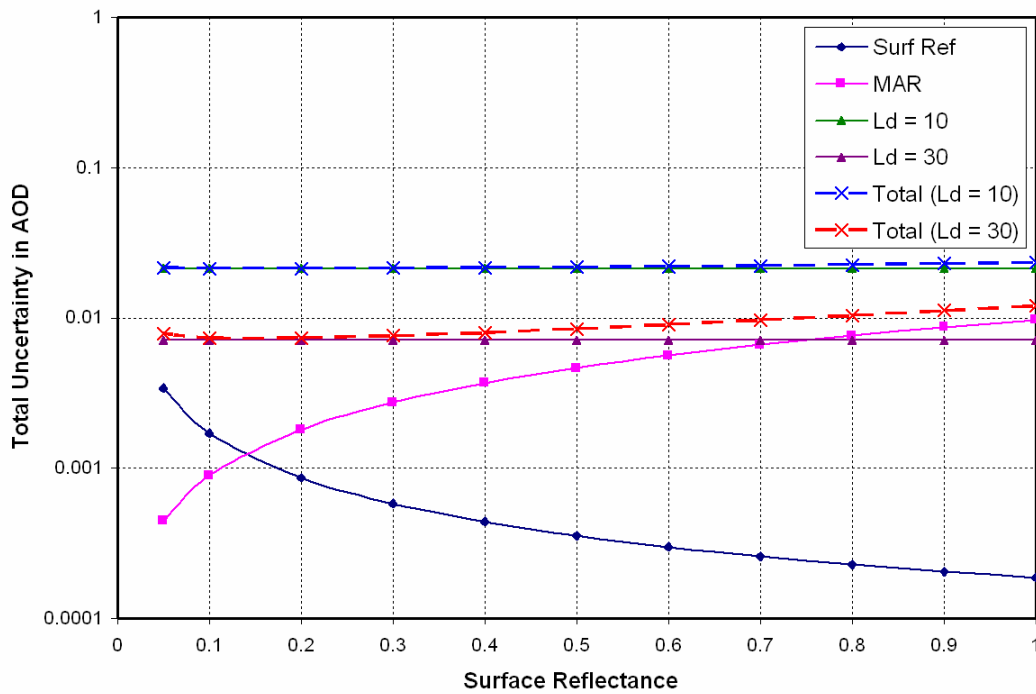
Figure 17.   Uncertainty analysis for the QuickBird blue channel (482 nm) for $L_d = 10$ and $L_d = 30$.
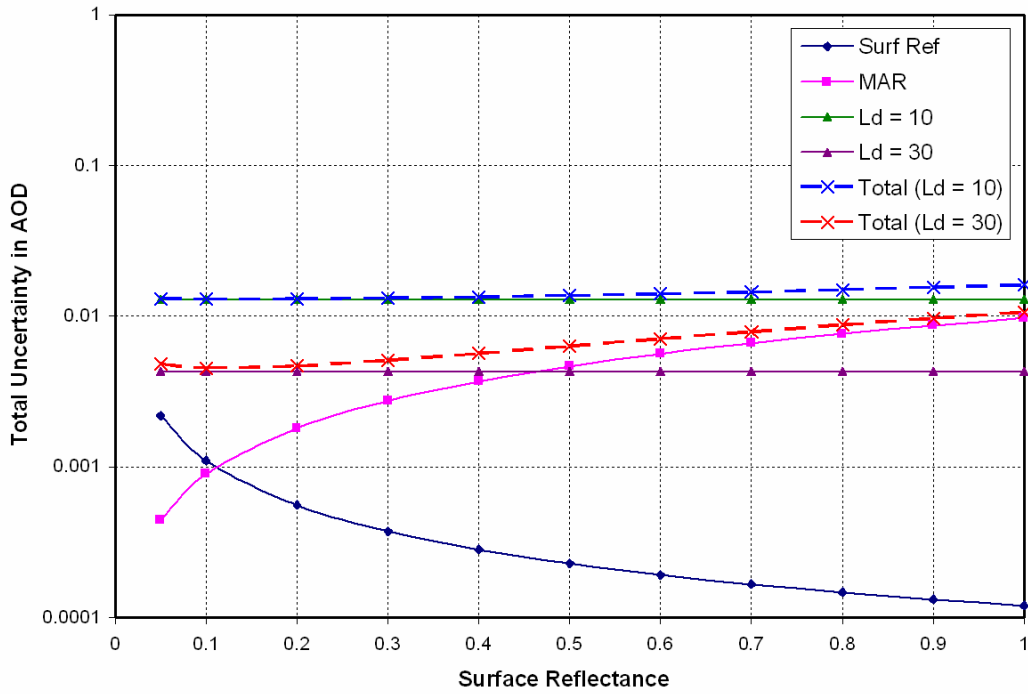
Figure 18.   Uncertainty analysis for the QuickBird green channel (556 nm) for $L_d = 10$ and $L_d = 30$.
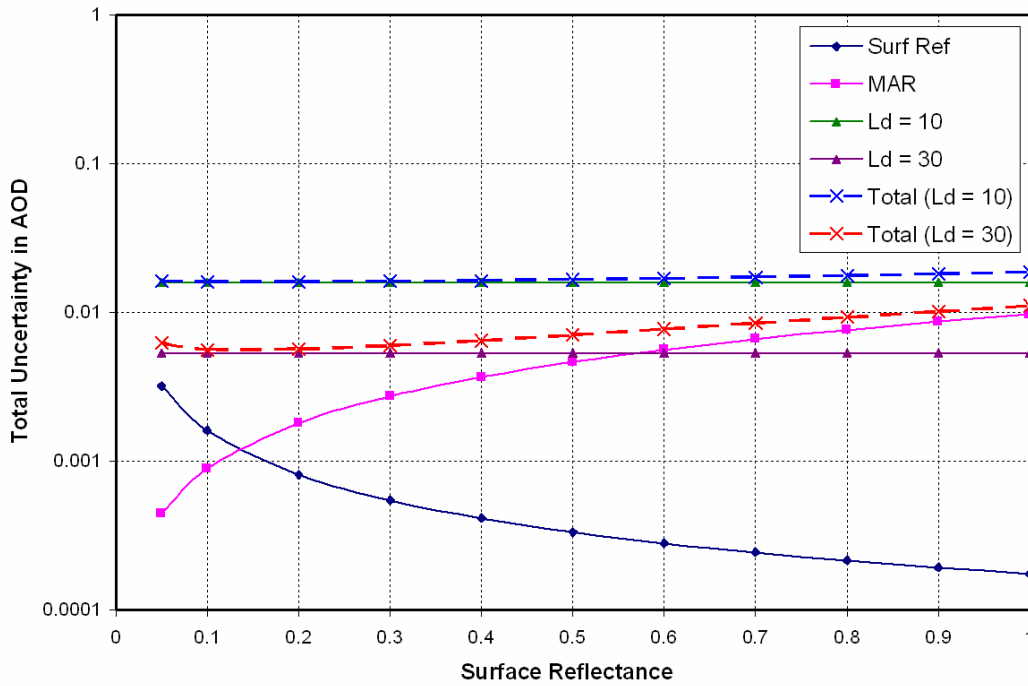
Figure 19.   Uncertainty analysis for the QuickBird red channel (658 nm) for $L_d = 10$ and $L_d = 30$.
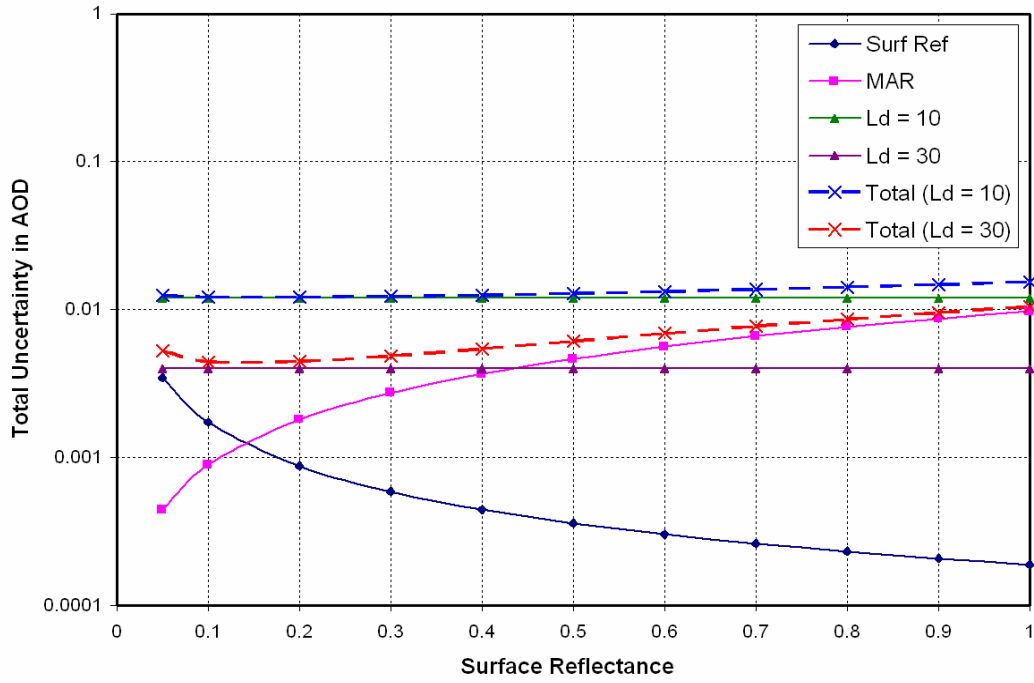
Figure 20.   Uncertainty analysis for the QuickBird near-infrared channel (816 nm) for
L_d = 10 and L_d = 30.
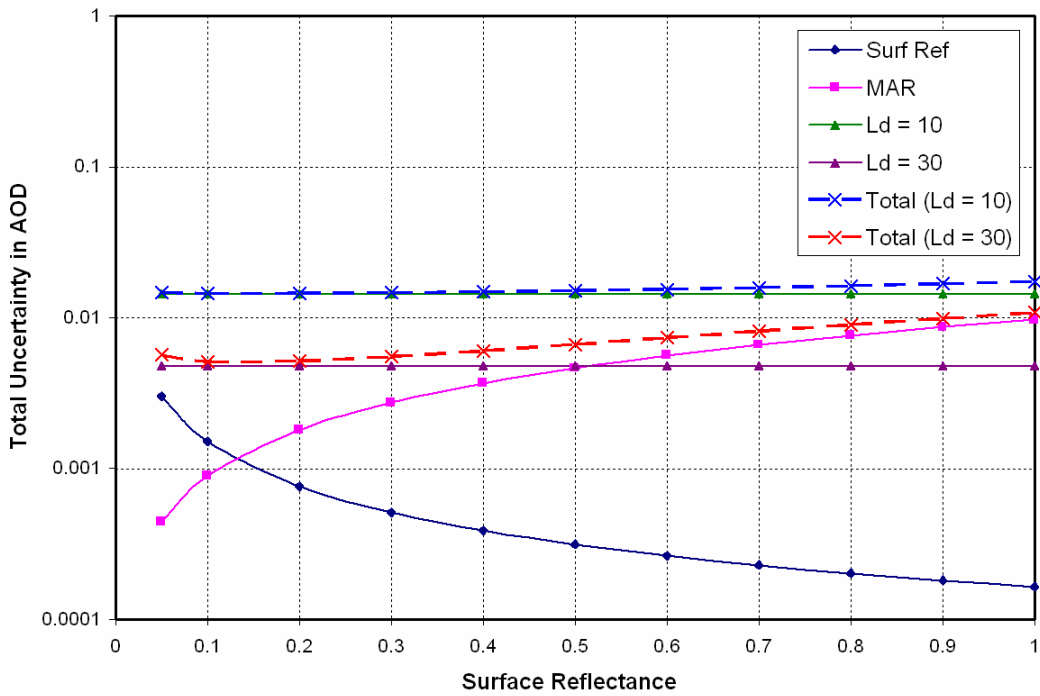
Figure 21.   Uncertainty analysis for the QuickBird Panchromatic Channel (673 nm) at
L_d = 10 and L_d = 30.

VI. AOD RETRIEVAL METHOD

A. OVERVIEW OF AOD RETRIEVAL METHODOLOGY

The shadow-based AOD retrieval method is intended for use with high-spatial (< 5-meter) resolution commercial satellite imagery with no *a priori* knowledge of surface reflectance or mean aerosol reflectance. As such, an iterative approach must be used when retrieving total optical depth with Eq. (34).

In the first estimation of total optical depth (TOD), mean aerosol reflectance is assumed to be much smaller than surface reflectance such that the product of surface reflectance and mean aerosol reflectance is much less than one and can be neglected in the denominator of the second term on the RHS of Eq. (34). Top of the atmosphere (TOA) reflectance over the unshaded area is used as surface reflectance in the first iteration. A total optical depth is retrieved and subsequently used to determine a mean aerosol reflectance using Eq. (27). This mean aerosol reflectance is subtracted from the surface (TOA) reflectance and total optical depth is again retrieved using Eq. (34). This retrieved total optical depth is then corrected for molecular Rayleigh scattering using Eq. (35) to produce an aerosol optical depth.

B. METHODOLOGY

To begin the process of retrieving AOD from the QuickBird satellite imagery using Eq. (34), one must first collect the solar/viewing geometry and the radiance values from the orthorectified and calibrated image. The Environment for Visualizing Images (ENVI) version 4.1 from Research Systems, Incorporated was used for viewing, orthorectifying, calibrating, and interrogating the QuickBird imagery. ENVI is a suite of imagery analysis applications written in the Interactive Data Language (IDL), also from Research Systems, Incorporated. A program based on IDL version 6.1 was written to process the information collected using ENVI and carry out the necessary calculations required by Eq. (34). Figure 22 provides a diagram of the AOD retrieval process from initial calibration of the imagery to retrieval of the AOD.
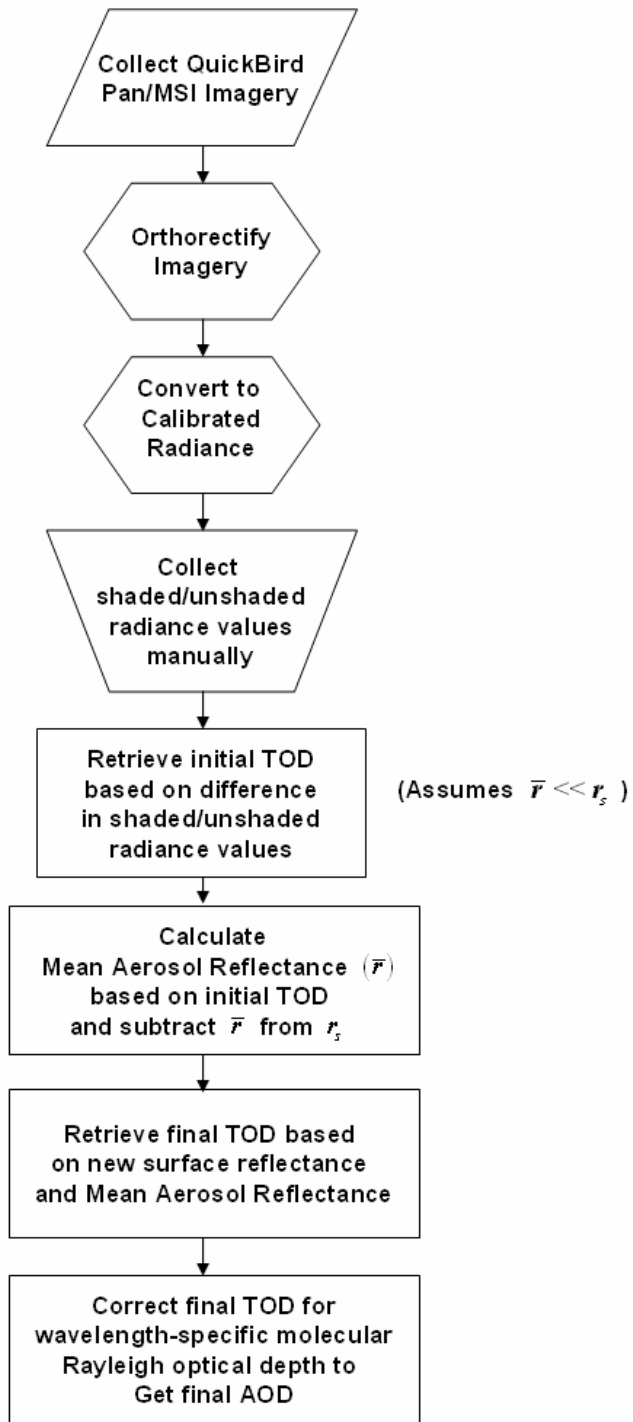
Figure 22.   Process flow for retrieving aerosol optical depth from QuickBird satellite imagery using the shadow method.

1. Imagery Collection

The QuickBird imagery used in the desert background investigation was tasked and purchased from DigitalGlobe through the National Geospatial-Intelligence Agency (NGA). DigitalGlobe provided a primary and alternate imaging windows based on customer provided locations and time frames. Once collected, the DigitalGlobe provided the images to NGA for archive in the Commercial Satellite Imagery Library (CSIL) and transfer to the end-user. NGA provided 11-bit, un-rectified images in NITF 2.0 format on DVD approximately five to seven days from image collection. The remaining imagery used for the urban and grass background investigations were obtained from the CSIL archive.

2. Imagery Orthorectification

An ENVI-provided data specific utility was used to read in the QuickBird imagery in NITF 2.0 format. The image, still in image-relative coordinates, must be orthorectified, or reprojected into real-world coordinates with corrections for tilt and relief. ENVI has another QuickBird-specific tool for orthorectification that allows the user the choice between using a rational polynomial coefficient file (.RPB) provided with the imagery or user-defined ground control points. In this case, the first option was used with .RPB files provided by DigitalGlobe. Elevation information and geoid offset, the difference between mean sea level and the gravitational potential surface, for each scene is also required. In desert background investigation, each image was centered on a coastal site and was processed with a fixed height of one meter with no geoid offset. For the remaining images, the fixed height was read from the metadata file for each image and no geoid offset was used. While this is not the most accurate method of orthorectification, sampling of pixels was done by visual inspection and did not require extremely accurate orthorectification or geolocation.

3. Conversion to Calibrated Absolute Radiance Values

Once the images were orthorectified, the image data were converted from relative radiance values into absolute radiance values. Like orthorectification, ENVI includes a

data specific utility to carry out this task, however, this tool was not used. The ENVI-provided tool uses the DigitalGlobe absolute calibration factor found in the image metadata file provided with the image and nominal bandpass widths to convert the data from units of watts per meter squared per steradian (W m^{-2} sr^{-1}) into micro-watts per centimeter squared per steradian per nanometer (μW cm^{-2} sr^{-1} nm^{-1}). The nominal bandpass widths used by ENVI, while close, are rounded to the nearest tens of nanometers and can introduce additional uncertainty to the absolute radiance values. As such, the Band Math tool was used to construct a simple expression based on the absolution calibration factor and the actual bandpass width for each channel. The final absolute radiance values returned by this process are in watts per meter squared per steradian per nanometer (W m^{-2} sr^{-1} nm^{-1}).

4.   Manual Collection of Unshaded/Shaded Radiance Values

Radiance values were collected from adjacent unshaded/shaded areas using the Region of Interest (ROI) tool in ENVI. The ROI tool allows the user to define an area using a polygon, rectangle, or oval, save the location of that area and manipulate or analyze the data only in that area. In this case, the polygon tool was used to collect areas within and just outside of the shadows. The ROI tool also includes a Statistics function that calculates maximum, minimum, mean and standard deviation of the pixel values within each region of interest for each channel in the image. A Histogram option is also available in the Statistics function and was used to determine the mode radiance within each region of interest for the panchromatic channel. Maximum, minimum, mean and mode radiance values were archived for each region of interest for the panchromatic channel and maximum, minimum, mean and standard deviation of the radiance values for the multi-spectral channels in each image.

5.   Retrieval of Aerosol Optical Depth from QuickBird Imagery

An IDL program was constructed to carry out the retrieval of AOD from the QuickBird imagery. This program carries out four distinct steps: (1) retrieval of the initial total optical depth, (2) determination of the mean aerosol reflectance based on the

initial total optical depth and partitioning of the total reflectance into surface and mean aerosol reflectance, (3) retrieval of the final total optical depth based on the surface and mean aerosol reflectance, and (4) correction of the final total optical depth for molecular Rayleigh scattering. Each step is described in depth below.

a.   *Retrieval of Initial Total Optical Depth (TOD)*

The IDL AOD retrieval program first uses matrices of unshaded and shaded radiance values (min, max, mean, and, in the case of the panchromatic channel, mode) to determine the radiance difference. A total optical depth (TOD) is then retrieved using the radiance difference, the solar/sensor geometry, and the assumption that the mean aerosol reflectance is at least an order of magnitude smaller than the surface reflectance. In this first step, surface reflectance is taken as the top of the atmosphere reflectance based on the unshaded radiance value. The total optical depth returned in this section is then used to determine a mean aerosol reflectance.

b.   *Determination of Mean Aerosol Reflectance and Partitioning of Top-of-the Atmosphere (TOA) Reflectance*

The assumption that surface reflectance is much larger than mean aerosol reflectance breaks down over areas of low surface reflectance, however, mean aerosol reflectance is multiplied by surface reflectance only as a minor corrective term. The real impact of this assumption lies in the overestimation of mean aerosol reflectance and its effect on the partitioning of top of the atmosphere reflectance. If the mean aerosol reflectance is greater than the top of the atmosphere reflectance, a possibility with low surface reflectance, then the resulting surface reflectance will be negative. Mean aerosol reflectance is determined using a numeric approximation of the quadruple integral in Eq. (27). A ten-degree increment was used for azimuthal integrations and a five-degree increment was used for integrations over zenith angle. Additionally, integrations over zenith angle were only carried out to 85° due to the extremely small values of the cosine function as the argument approaches 90°. Sensitivity tests designed to determine if this truncation of the zenith angle would significantly impact the final answer showed that both the one-degree and two-degree increments in zenith angle taken to 89° and 88°

respectively, differed by less than 10% of the total value when evaluated to 85°. The larger angular increments used in this approximation not only returned integrated values very close to those from much smaller angular increments, but also reduced computer run time for a ten target set from 20 minutes to approximately 30 seconds.

The Henyey-Greenstein phase function is used to approximate the phase function of the aerosol required in Eq. (27). The Henyey-Greenstein phase function requires an asymmetry parameter to determine the amount of backscatter (0 to -1) or forward scatter (0 to 1) (Henyey and Greenstein 1941). The value used for each image varied by location and is described in results chapter for each investigation. Equation (27) also requires a single scatter albedo to determine the mean aerosol reflectance. The value used for each image varied by location and is described in Section C. of each chapter detailing the different background investigations.

Finally, the mean aerosol reflectance was subtracted from the top of the atmosphere reflectance to partition top of the atmosphere reflectance into surface and mean aerosol reflectance. These values were passed back to the governing equation, Eq. (34), to retrieve the final total optical depth.

6.   Retrieval of Final Total Optical Depth and Correction for Molecular Rayleigh Scattering

Total optical depth is retrieved using Eq. (34) based on the new surface and mean aerosol reflectances. This total optical depth represents the attenuation due to aerosol particles, aerosols in gaseous phase, and molecular Rayleigh scattering. Here, it is assumed that the aerosol particles are the dominant scatterers and that aerosols in gaseous phase contribute little to the total attenuation. Therefore, only a band-averaged correction for molecular Rayleigh scattering optical depth is carried out using Eq. (35). The final aerosol optical depth for each site is archived along with all values from each step of the program.

VII.   DATA

A.   OVERVIEW OF OBSERVATIONAL DATA

Two main types of data are required for this study. First, high-resolution commercial satellite imagery capable of spatial resolutions of 5 meters or better is required for AOD retrievals. Second, a reliable source of independent aerosol optical depth data is required for validation of AOD retrievals. DigitalGlobe's QuickBird satellite currently provides the highest-spatial resolution, commercially available satellite imagery. The QuickBird satellite is capable of 0.61-meter resolution imagery using a panchromatic channel and 2.44-meter resolution using four multi-spectral channels (blue, green, red, and near-infrared) (DigitalGlobe 2005a). The Aerosol Robotic Network (AERONET), supported and maintained largely by NASA's Earth Observing System, is an optical ground-based aerosol monitoring network and is used in these studies as ground-truth for satellite-based AOD retrievals (Holben *et al.* 1998). An in-depth description of both systems is provided below.

B.   QUICKBIRD   HIGH-SPATIAL   RESOLUTION   COMMERCIAL SATELLITE IMAGERY

The QuickBird satellite is the first commercial satellite to offer sub-meter resolution imagery for the open market. An altitude of 450 km with a 98°, sun-synchronous inclination allows revisit frequency of approximately 3.5 days at the equator and closer to one day at the poles. A local equator crossing time of 10:30 a.m. ensures that solar illumination provides a sufficient length of shadow for the proposed retrieval method. QuickBird data has a dynamic range of 11 bits and is available at 0.61-meter resolution from the panchromatic sensor (445 nm to 900 nm) and 2.44-meter resolution for the multi-spectral sensor (blue (450-520 nm), green (520-600 nm), red (630-690 nm), and near-infrared (760-900 nm)) for near-nadir views. Minimum, maximum, and central effective wavelengths for each band are shown in Table 5 along with the average in-channel spectral solar irradiance for each channel. The average scene is approximately 16.5 km by 16.5 km, however the sensor can collect strips that are 16.5 km wide and 165 km long. Mosaics of individual scenes may also be constructed when one image or strip

cannot cover the area of interest completely. The QuickBird satellite is an agile spacecraft with in-track and cross-track pointing capability, generally restricted to within 30° of nadir, but greater viewing zenith angles are possible upon request (DigitalGlobe 2005a). The specific images used in each study are described in the chapters detailing each investigation.

Table 5. QuickBird minimum, maximum and center effective wavelengths (after DigitalGlobe (2005)) with in band spectral solar irradiance based on Wehrli (1985) spectral solar irradiance curves.

QuickBird Channel	Minimum Wavelength (nm)	Maximum Wavelength (nm)	Center Effective Wavelength (nm)	Spectral Solar Irradiance (W m^{-2} nm^{-1})
Ch 1 (Blue)	450	520	482	1973
Ch 2 (Green)	520	600	556	1854
Ch 3 (Red)	630	690	658	1570
Ch 4 (Near-Infrared)	760	900	816	1095
Panchromatic	445	900	673	1506

The accuracy of the radiometric calibration of the QuickBird data is often key to aerosol optical depth retrievals. Martin (2004) questioned the radiometric calibration of QuickBird data and stated the need for further characterization of QuickBird's radiometric calibration. Holekamp (2003) and Thome (2003) present the results of vicarious calibration efforts in support of the Joint Agency Commercial Imagery Evaluation (JACIE) team. Vicarious calibration uses multiple sensors and known targets to establish a stable baseline of radiometric data that can be compared with the sensor to be calibrated. Thome (2003) characterized radiometric calibration changes from initial construction of the detectors at Kodak to bench tests during sensor assembly at Ball Aerospace. This work resulted in changes to the radiometric calibration coefficients distributed with QuickBird data (DigitalGlobe 2003). Holekamp (2003) focused

vicarious calibration efforts on testing the accuracy and stability of these new calibration coefficients instituted by DigitalGlobe and found that these new calibration coefficients underestimated radiance by 8.6%, 7.8%, 4.9% and 0.4% for the blue, green, red and near-infrared channels respectively. The shadow-based AOD retrieval method is based on the ratio of surface reflectance (based on unshaded radiance) to the unshaded/shaded radiance difference with a minor correction for surface reflectance in the denominator. Because of this, calibration errors largely cancel out and only a small error, on the order of 0.001, results from a calibration error of ten percent. In addition to the overall radiometric calibration error, the in-band variation of the calibration coefficient with brightness can add error to the difference between observed radiances in the unshaded and shaded areas of the image. In this study, a linear relationship between radiance and brightness count is assumed for QuickBird based on IKONOS calibration efforts outlined in Pagnutti *et al.* (2003).

The QuickBird data used in the desert background investigation described in Chapter VIII was collected in support of the Unified Aerosol Experiment, United Arab Emirates (UAE^2) with the assistance of the National Geospatial Intelligence Agency (NGA). The QuickBird data used in the urban and grass background investigations were obtained from NGA's Commercial Satellite Imagery Library.

C.   AEROSOL ROBOTIC NETWORK (AERONET)

The Aerosol Robotic Network (AERONET) is federation of ground-based aerosol-focused remote sensing networks that provide a common set of instrumentation, calibration, and processing strategies as well as data archival capabilities (Holben *et al.* 1998, GSFC 2005). Products from this global network typically include spectral optical depths, inversion products based on assumptions about the aerosol physical properties, and precipitable water in three data levels: Level 1.0 consisting of unscreened data, Level 1.5 consisting of cloud-screened data, and Level 2.0 consisting of cloud-screen and quality assured data. The Level 2.0 data using the Direct Sun version 2.0 processing scheme is used unless otherwise noted. The standard AERONET channels and their associated bandwidths are listed in Table 6.

Table 6. Standard AERONET Channels and their associated bandwidths (GSFC 2005).

Standard AERONET Wavelengths (nm)	Bandwidth (nm)
340	2
380	4
440	10
500	10
675	10
870	10
940	10
1020	10

It should be noted that the bandwidths of the AERONET channels do not match the bandwidths of the QuickBird channels. To ensure suitable comparisons of QuickBird-derived aerosol optical depths to those from AERONET, band-averaged aerosol optical depths for the QuickBird channels were determined using exponential best-fit curves approximating the spectral distribution of AERONET values and then averaged over the QuickBird channel's bandwidth using the spectral response function of that channel. The resulting band-averaged aerosol optical depth for each QuickBird channel is used as ground truth with an uncertainty of ±0.02 for the AERONET data as described in Holben *et al.* (1998).

The data used in the desert background investigation were collected in support of the UAE[2] campaign using a network of 14 AERONET sites around the southern Arabian Gulf, the United Arab Emirates, and Oman (see Fig. 23). This network represents the finest resolution mesoscale network constructed for the purpose of aerosol remote sensing. The AERONET site collocated with Naval Research Laboratory's Mobile Atmospheric Aerosol and Radiation Characterization Observatory (MAARCO) (located at 24.7N-54.66E) was used for comparison with retrieved aerosol optical depths. Note that not all channels listed in Table 6 are available in the data used in this investigation.

The AERONET data used in the urban and grass background investigations were collected during routine monitoring for the network in each of the cities. Descriptions of

the AERONET data for each day of the investigations in included in Chapters VIII and IX.

Figure 23.   Distribution of the AERONET sites in support of the UAE^2 campaign.

THIS PAGE INTENTIONALLY LEFT BLANK

VIII. DESERT BACKGROUND INVESTIGATION

A.   OVERVIEW

The shadow method for AOD retrieval was originally developed to address the shortfalls of other AOD retrieval methods in the presence of highly reflective backgrounds such as deserts. The satellite imagery and meteorological data used in this investigation were collected in the United Arab Emirates during August and September of 2004 as a part of the Unified Aerosol Experiment, United Arab Emirates (UAE[2]). This field campaign provided a unique opportunity to image highly reflective desert backgrounds in a well-instrumented environment.

B.   OBSERVATIONAL DATA

As described in Chapter VII., QuickBird commercial satellite imagery and AERONET AOD data were used in this investigation. Below is a description of the individual scenes and the accompanying AERONET data used in the desert background investigation.

1.   Northeast of MAARCO – Taweelah, UAE, 19 August 2004

Initial tasking of the QuickBird imagery collection missed the MAARCO site by approximately 15 kilometers. As such, the multispectral and panchromatic imagery collected on 19 August 2004 was situated approximately 15 km northeast of the MAARCO site (24.7N-54.66E). Figure 24(a) is a MODIS overview of the Southern Arabian Gulf region. One can readily see in the MODIS image the location of clouds that would preclude the use of the shadow method. In the future, such operational meteorological satellite imagery will be very useful in locating areas were the shadow-based AOD retrieval method can be applied. Seven individual shadow sites used for shadow-based AOD retrieval are marked with green circles in the QuickBird image shown in Fig. 24(b). The red lines indicate the location of the QuickBird image in the larger scale MODIS image. An example of the individual shadows used can be seen in

Fig. 1 in Chapter II. The imagery covered the standard 16.5 km by 16.5 km area. Exact time and solar/viewing geometries are provided in Table 7.

Figure 24.   A MODIS Terra overview (a) of the Southern Arabian Gulf, including the United Arab Emirates, for 19 August 2004 and (b) the QuickBird RGB image of the area around Tahweelah, UAE for the same day and time with shadow retrieval targets marked with green circles. Red lines indicate the location of the QuickBird image in the larger MODIS image (QuickBird image courtesy of DigitalGlobe).

AERONET Level 2.0 data collected at the MAARCO site at 07:02 UTC were used for comparison with the aerosol optical depth retrievals from the August 19, 2004 QuickBird image. All channels were available and used in determining the exponential best fit of the spectral aerosol optical depth distribution.

2.   MAARCO – Northeast of Abu Dhabi, UAE, 16 September 2004

The QuickBird satellite imagery of the MAARCO site for 16 September 2004 also consisted of both panchromatic and multi-spectral imagery. Figure 25(a) is a MODIS overview of the region, while the 12 shadow sites used for both multispectral and panchromatic AOD retrievals are marked with green circles and 10 additional sites used for only panchromatic AOD retrievals are marked with blue circles in Fig. 25(b).

Again, the QuickBird imagery covered the standard 16.5 km by 16.5 km area. Exact time and solar/viewing geometries are provided in Table 7.
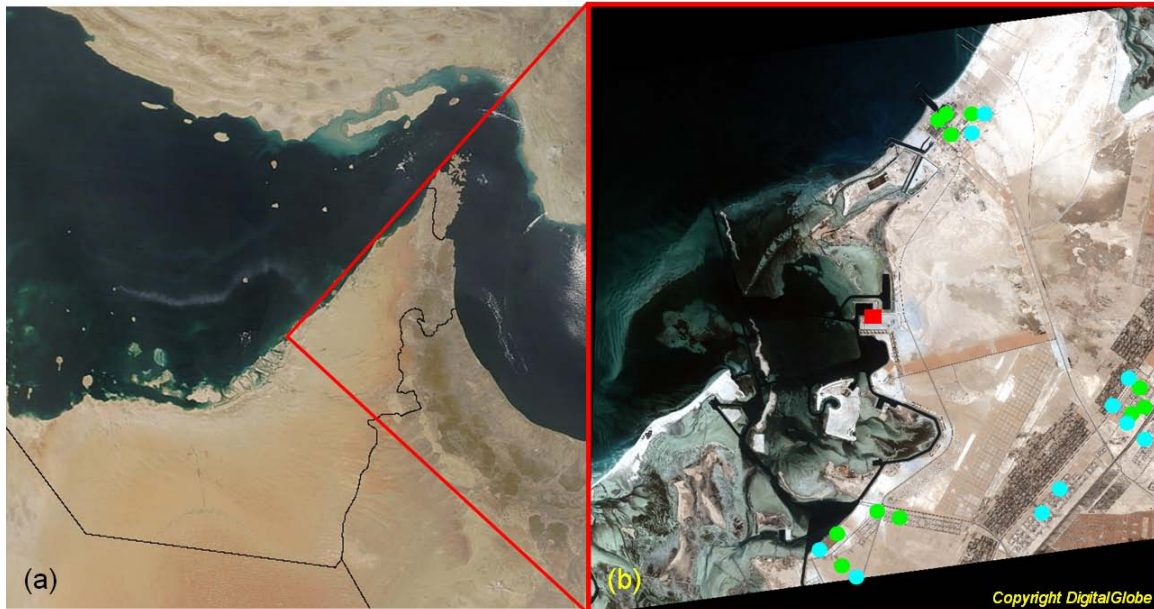
Figure 25.   A MODIS Terra overview (a) of the Southern Arabian Gulf, including the United Arab Emirates, for 16 September 2004 and (b) the QuickBird RGB image of the area around the MAARCO site for the same day and time with MSI shadow retrieval targets marked with green circles, panchromatic shadow retrievals marked with blue and green circles, and the MAARCO site marked with a red box. Red lines indicate the location of the QuickBird image in the larger MODIS image (QuickBird image courtesy of DigitalGlobe).

AERONET data collected at the MAARCO site at 06:55 UTC were used for comparison with QuickBird AOD retrievals from the September 16, 2004 QuickBird imagery. All channels were available and used in determining the exponential best fit of the spectral aerosol optical depth distribution.

3.   MAARCO – Northeast of Abu Dhabi, UAE, 24 September 2004

Again, the QuickBird satellite imagery of the MAARCO site on 24 September 2004 consisted of both panchromatic and multi-spectral imagery, however, in this case the solar and satellite azimuths are within 10° of each other. This solar/viewing geometry is unfavorable for observing shadows, as seen in Fig. 26 in which the favorable

solar/sensor geometry of (a) 16 September is compared to the unfavorable geometry of (b) 24 September. Relative azimuth differences of 90° to 180° are preferred. Again, the imagery covered the standard 16.5 km by 16.5 km. As seen above, Fig. 27(a) is the MODIS overview of the region with the 11 shadow sites are marked with green circles in the QuickBird image as shown in Fig. 27(b). Exact time and solar/viewing geometries are provided in Table 7.
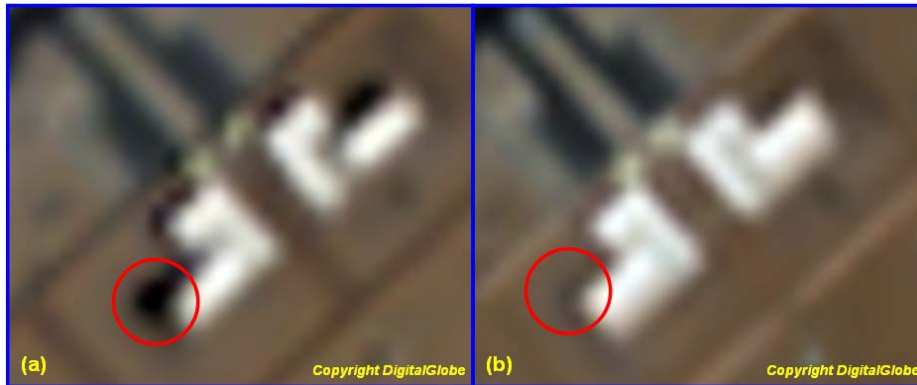
Figure 26.   Comparison of shadows produced from favorable solar/sensor geometry on (a) 16 September and unfavorable solar/sensor geometry on (b) 24 September (courtesy of DigitalGlobe).
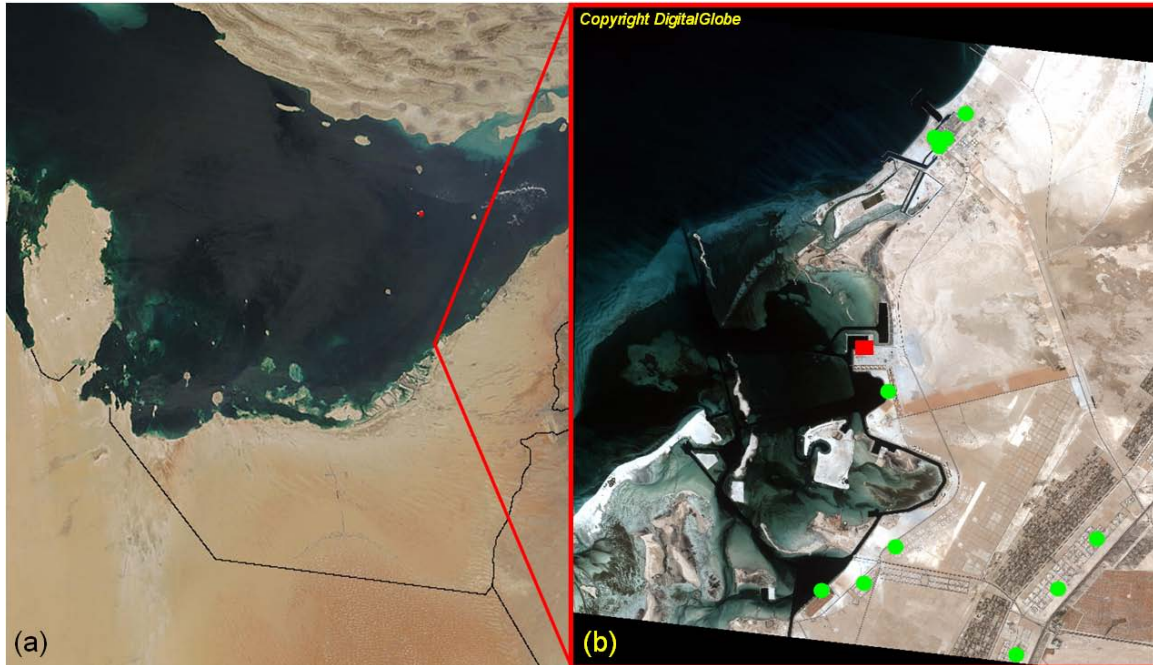
Figure 27. A MODIS Terra overview (a) of the Southern Arabian Gulf, including the United Arab Emirates, for 24 September 2004 and (b) the QuickBird RGB image of the area around the MAARCO site for the same day and time with shadow retrieval targets marked with green circles and the MAARCO site marked with a red box. Red lines indicate the location of the QuickBird image in the larger MODIS image (QuickBird image courtesy of DigitalGlobe).

AERONET data was not collected at the MAARCO site at the time of the September 24, 2004 QuickBird image (06:59 UTC). However, Microtops II Sun photometer data was collected between 06:50 UTC and 07:01 UTC using three different instruments. Data collected at 06:59 UTC was used and handled in the same manner as the AERONET data.

Table 7. Location, date, time, solar/viewing geometry and cloud cover for the QuickBird imagery used in the desert background investigation.

Location	Date	Time (UTC)	Satellite Zenith	Satellite Azimuth	Solar Zenith	Solar Azimuth	Cloud Cover
MAARCO	19 Aug 04	06:56	24.2°	047.6°	24.1°	116.2°	20%
MAARCO	16 Sep 04	07:09	28.1°	223.5°	27.4°	141.1°	0
MAARCO	24 Sep 04	06:59	23.2°	149.9°	31.0°	141.7°	0

C.   AEROSOL CHARACTERISTICS

The Southern Arabian Gulf and Arabian Peninsula is a complicated region and forms a "meteorological crossroads" of sorts coming under the influence at various times of atmospheric interactions with the Tibetan Plateau, the Indian sub-continent, and Saharan Africa. The overall synoptic pattern of South West Asia and the Arabian Gulf region is dominated by a monsoon regime in which a Northeasterly monsoon sets up in the winter and a Southwesterly monsoon in the summer, with transition periods in between. Appendix A provides a brief description of these monsoons as outlined in the Science Plan for the UAE[2] campaign (Reid *et al.* 2004) and described in depth by the Forecaster's Handbook (NCMOF Bahrain 1999), with emphasis on the Southwesterly monsoon that dominated during the UAE[2] campaign.

The complicated nature of this regional climatology results in several varied source regions for aerosol particles, as well as several types of aerosol particles. Appendix A provides information on potential source regions for the aerosol particles found in the scenes used in this investigation. The shadow method, however, is not extremely sensitive to the accuracy of the parameters used to describe the aerosol particles, asymmetry parameter and single scatter albedo. For this investigation, an asymmetry parameter of 0.65 and a single scatter albedo of 0.94 were used (Reid 2005). These values adequately describe the forward scatter and low absorption nature of the dust typically found in the region.

D.   RESULTS

1.   Mean QuickBird-retrieved Aerosol Optical Depths

The mean of all shadow-based AOD retrievals, annotated by day and QuickBird channel are shown in Fig. 28. The standard error of the mean is annotated as an error bar parallel to the y-axis, while the uncertainty of the AERONET data, ±0.02, and is shown parallel to the x-axis. It can be quickly seen that the shadow-based AOD retrieval method performed well on September 16, 2004, while the other two days showed a slight high bias in means of the AOD retrieval as well as larger standard error. In all cases, the blue, green and red channels showed a spectral consistency even though all retrievals were made independently. The AOD retrievals from the near-infrared channels show a slight high bias above what would be expected from the spectral distribution of the other multi-spectral AOD retrievals. Also of note is the low bias of the AOD retrievals from the panchromatic channel.
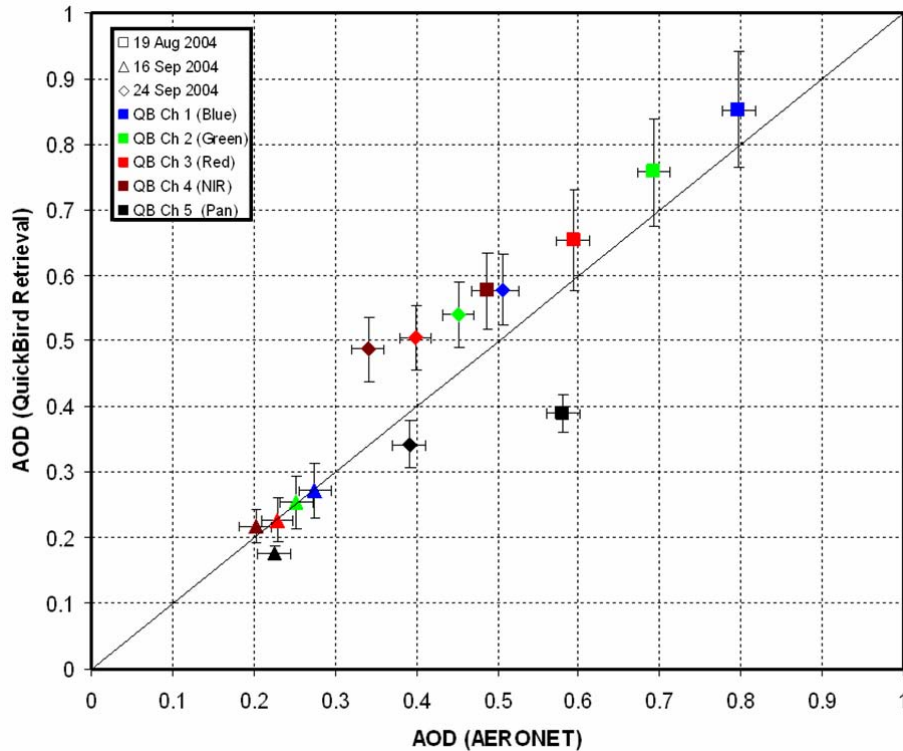
Figure 28.   Mean shadow-based AOD retrievals over desert backgrounds for 19 August, 16 September, and 24 September 2004 in the vicinity of the MAARCO site.

2. Surface Reflectance Retrievals

Chapter IV quantified the sensitivity of the shadow method to surface reflectance and established a minimum requirement for surface reflectance of 0.15. Chapter VI outlined the procedure used to determine surface reflectance by partitioning the top of the atmosphere reflectance between surface reflectance and mean aerosol reflectance. To ensure this method of surface reflectance determination was appropriate, Eq. (34) was solved for surface reflectance and then evaluated for each site using the AERONET-retrieved AOD. The resulting equation for surface reflectance is:

$$r_s = \frac{c}{1 + \bar{r}c}, \text{ where} \tag{62}$$

$$c = \left(\frac{\pi L_d}{\mu_0 F_0} \right) e^{\delta \left(\frac{1}{\mu_0} + \frac{1}{\mu} \right)}. \tag{63}$$

The resulting surface reflectances were compared to the surface reflectances determined by the partitioning of the top of the atmosphere reflectance as shown in Fig. 29. Mean aerosol reflectance for all surface reflectance retrievals was calculated based on the AERONET AOD. All other parameters were used from the original QuickBird AOD retrieval.

The shadow-based AOD retrieval method was originally designed to address the issue of retrievals in the presence of highly reflective backgrounds. The range of surface reflectances seen in this investigation runs from 0.1 to 0.4 with the red, near-infrared, and panchromatic channels having the highest reflectances as seen in Fig. 29. Note that almost all surface reflectances are above the 0.15 minimum reflectance suggested in Chapter IV. Comparing the QuickBird-derived surface reflectance to the surface reflectance required by the AERONET-measured AOD, one can see that errors, while weakly correlated, show a large variation and no clear bias. The QuickBird-derived panchromatic surface reflectances are the exception and show a consistent low bias (black dots above the one to one correlation) compared to the surface reflectance required by the AERONET retrieval.
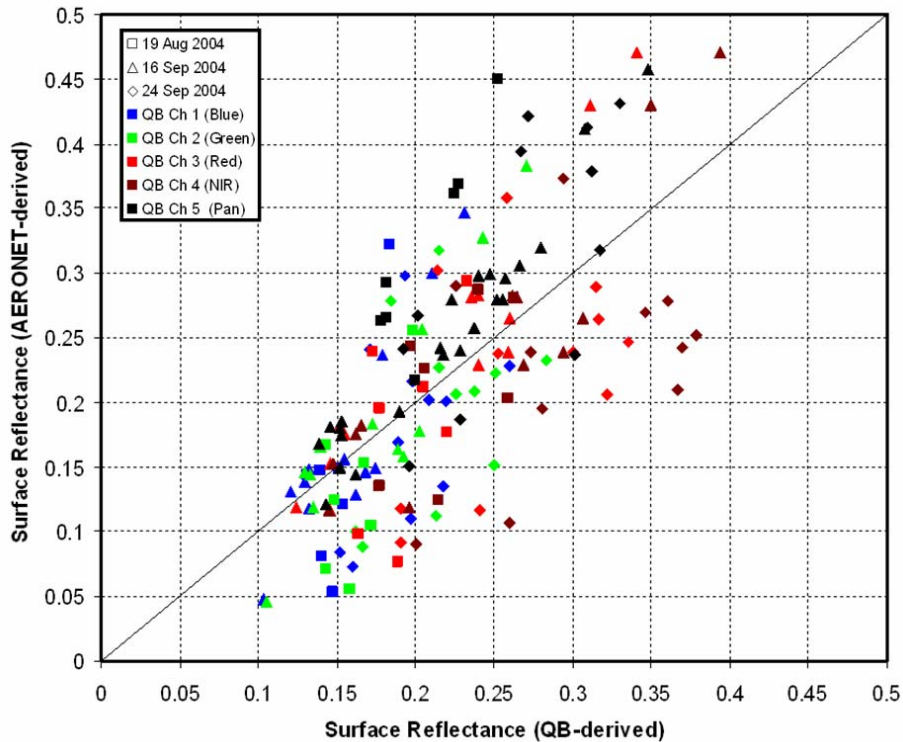
Figure 29.   Comparison of QuickBird-derived surface reflectances as determined from measured unshaded radiance to surface reflectance required to obtain the AERONET-derived AOD.

3.   Sources of Error

Without a controlled environment in which to carefully fix and vary factors affecting the parameters of the governing equation, specific sources of error cannot be conclusively identified. However, by studying the errors in the final AOD retrievals in the context of the sensitivity analysis presented in Chapter IV, one can determine whether the errors seen are consistent with errors in the individual parameters of the governing equation.   In this section, the errors will be examined for consistency with the expectations set out in Chapter IV (e.g. minimum surface reflectance criteria) and possible explanations will be presented. Factors that are well described and taken as constant, such as solar and satellite zenith angles, will not be examined in favor of focusing on more dynamic factors, such as surface reflectance.

a. *Unshaded/Shaded Radiance Difference*

One possible source of error lies in the value and the determination of the unshaded/shaded radiance difference. This is the primary measured signal on which the shadow-based AOD retrieval method is based. The expected decrease in error with increased unshaded/shaded radiance difference, as suggested in Chapter IV, can be seen in Fig. 30, with minimum error occurring with radiance differences of approximately 40 to 70 W m^{-2} sr^{-1} nm^{-1}. A minimum unshaded/shaded radiance difference of 10 W m^{-2} sr^{-1} nm^{-1}, as suggested in Chapter IV, would only remove a small number of retrievals with the highest error and does little to improve the overall mean AOD. Based on the mean AOD retrievals discussed in Section D. subsection 1 of this chapter, the errors seen here are largely minimized in the averaging process.
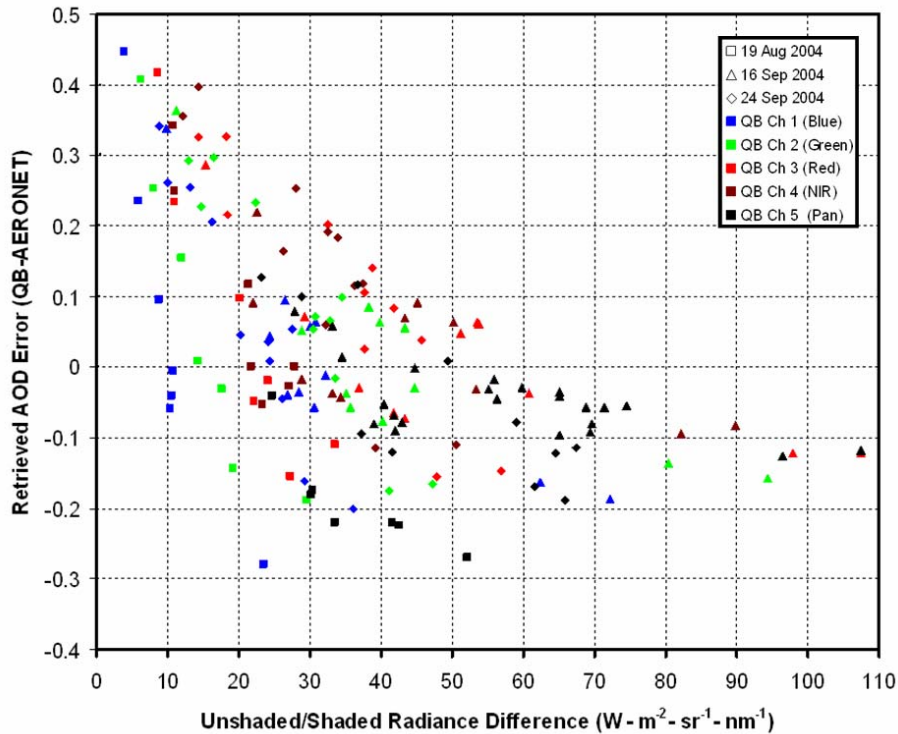
Figure 30.   Shadow-based AOD retrieval error as a function of unshaded/shaded radiance difference for all desert background cases.

The unshaded/shaded radiance difference seems immune to most factors that would affect measured radiance, such as area-wide increases in diffuse radiance or calibration errors, as both the unshaded and shaded regions are affected equally by these

effects and the radiance difference is unaffected. However, this is not necessarily true of some adjacency effects, or brightening of dark pixels by adjacent bright pixels. Typically, the adjacency effect is considered over a large area, such as clouds contrasting with a darker surface or bright desert areas on the coast, and would increase the diffuse field over both the unshaded and shaded areas equally. At high spatial resolutions, a similar effect happens when the relative azimuth between the solar and satellite viewing geometries is small and the structure casting the shadow is highly reflective. In this case, the shadow is almost blocked by the shading structure and only a small portion of the shadow is available for sampling. This small portion, when viewed next to a highly reflective structure can increase the radiance within the shadow, but may not necessarily increase the radiance outside the shadow to the same degree, thus reducing the unshaded/shaded radiance difference. A required minimum relative azimuth difference between solar and satellite viewing geometries is required, not only for access to the shadow, but also to minimize this contamination.

One final error source to consider in the unshaded/shaded radiance difference is due to data collection methods. The mean radiance value was used both within and outside of the shadow in determining the unshaded/shaded radiance difference. If the pixels used in the calculation are partially shaded or partially illuminated, the difference will likely be decreased and cause an increase in AOD (-0.04 for each increase of 1 W m^{-2} sr^{-1} nm^{-1}). Such contamination is less likely in the panchromatic band due to the higher resolution. With the increased number of points comes the ability to determine the mode radiance both within and outside of the shadow and preclude any contamination by partially illuminated or shaded pixels. The error associated with the operator will vary greatly and be difficult to quantify until an automated process is developed.

b.   *Surface Reflectance/Mean Aerosol Reflectance*

Surface reflectance provides the largest potential source of error in the shadow-based AOD retrieval method. While the unshaded/shaded radiance difference is largely unaffected by changes in the diffuse radiance field, the surface reflectance determined from the unshaded radiance is subject to all diffuse field fluctuations. In

addition to establishing a minimum required surface reflectance of 0.15, Chapter IV shows error in the individual AOD retrievals is inversely proportional to surface reflectance. Such a relationship is only weakly evident as seen in Fig. 31 and, in fact, little correlation can be seen between surface reflectance and error in retrieved AOD. Therefore, it is suggested that error in retrieved AOD viewed in the context of error in surface reflectance may provide clues to relevant error mechanisms.
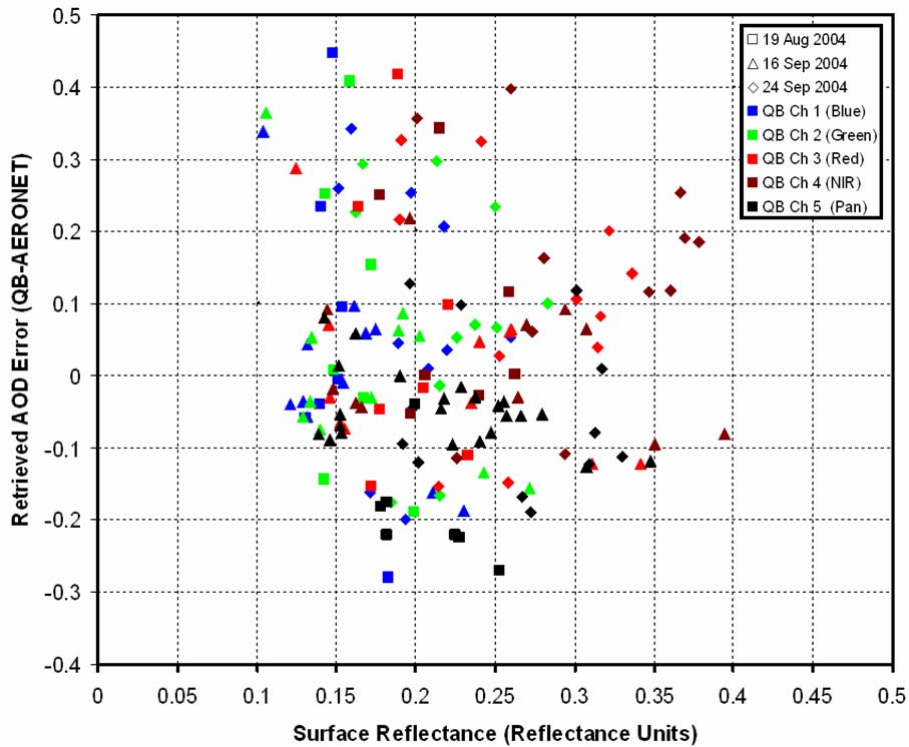
Figure 31.   Shadow-based AOD retrieval error as a function of surface reflectance for all desert background cases.

The methodology used in the shadow-based AOD retrieval method produces a consistent low bias in surface reflectance due to an overestimation of mean aerosol reflectance. In the initial calculation of total optical depth, mean aerosol reflectance is assumed to be negligible and top of the atmosphere (TOA) reflectance, as determined from the measured unshaded radiance is used in place of surface reflectance. This produces an initial total optical depth with a consistent high bias. This total optical depth is used to determine the mean aerosol reflectance, also resulting in a high bias. Top

of the atmosphere reflectance is then partitioned by subtracting the mean aerosol reflectance and classifying the remainder as surface reflectance. Mean aerosol reflectance values tend toward a high bias of 0.01 to 0.03 resulting in a corresponding low bias to surface reflectance values. The sensitivity of the final shadow-based AOD retrieval to surface reflectance is a 0.04 increase for every 0.01 increase in surface reflectance. The sensitivity of the final AOD retrieval to mean aerosol reflectance is a 0.002 decrease for every 0.01 increase in mean aerosol reflectance. Therefore, for every 1% error in surface reflectance, there should be a corresponding error in AOD of 0.038 if the error were only due to the overestimation of mean aerosol reflectance and underestimation of surface reflectance. To demonstrate this, all three desert cases were combined in Fig. 32 and retrieved AOD error was compared to error in surface reflectance as determined above in Section D, subsection 2.
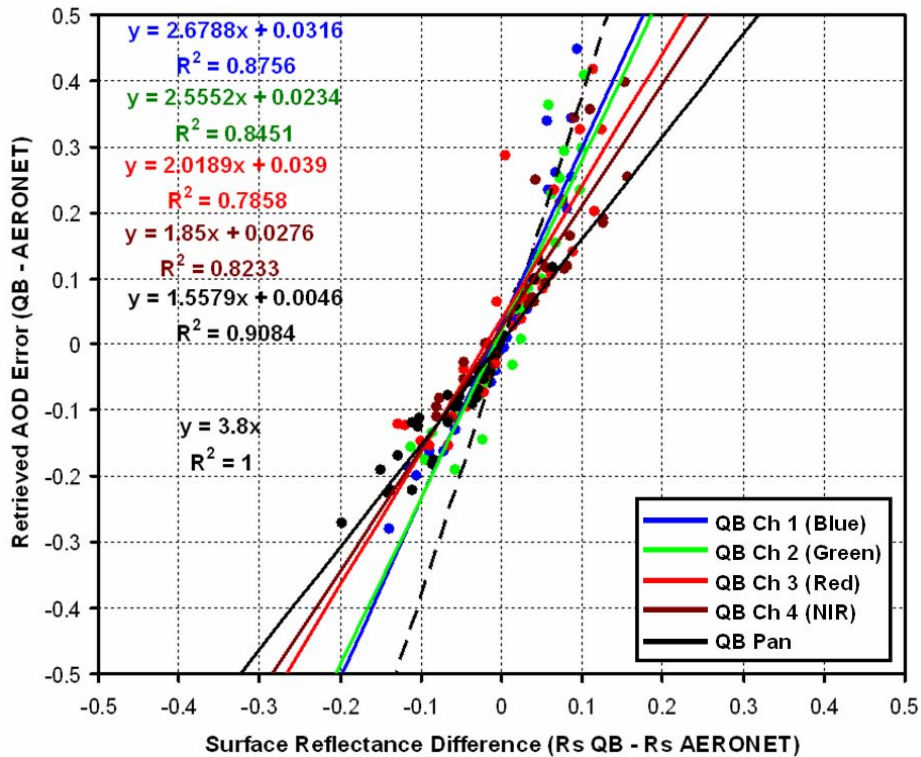
Figure 32.   Retrieved AOD error as a function of surface reflectance error for all three desert cases combined for each QuickBird channel. The dashed line denotes the theoretical error due to overestimation of mean aerosol reflectance and underestimation of surface reflectance combined. Solid lines represent a best fit for the corresponding QuickBird channel.

The relationships seen in Fig. 32 between the error in surface reflectance and the retrieved AOD error are generally consistent with the sensitivity analyses presented in Chapter IV (indicated by values falling along the dashed line), however, the retrieved AOD error cannot be solely attributed to underestimating surface reflectance. Another factor or factors appear to offset the retrieved AOD error from what is expected with the accompanying surface reflectance error and the magnitude of the offset seems to be proportional to the central wavelength of the channel considered (i.e., larger offsets for the near-infrared channel versus the blue channel). While some portion of the retrieved AOD error is consistent with the systematic bias of surface reflectance in the procedure, other sources of error in surface reflectance must be investigated.

Factors affecting the unshaded radiance, and thus the TOA reflectance prior to partitioning, must be considered. Holekamp (2003) asserted that DigitalGlobe's post-launch calibration coefficients underestimated QuickBird radiance values by 8.6%, 7.8%, 4.9% and 0.4% for the blue, green, red and near-infrared channels respectively. The panchromatic channel was not characterized by Holekamp (2003). Such errors would cause an additional low bias to the TOA reflectance and, subsequently, to the surface reflectance. This is not consistent with the offset of the systematic low bias in surface reflectance, and is, in fact, in the opposite direction.

One of the initial assumptions in the shadow-based AOD retrieval method was that molecular absorption due to atmospheric gases was negligible in the visible and near-infrared portion of the solar spectrum covered by the QuickBird channels. Molecular absorption would reduce transmittance and decrease the satellite-observed radiance, decreasing the TOA and surface reflectance and the unshaded/shaded radiance difference. Only the panchromatic channel suffers from a constant low bias that would be consistent with the effects of molecular absorption. A correction factor was determined for the combined effects of carbon dioxide, oxygen, ozone, and water vapor using MODTRAN 4 based on AERONET-measured precipitable water and an average tropical atmosphere. Water vapor accounted for nearly half of the calculated absorption. Improvements in the panchromatic AOD retrieval can be seen in Fig. 33 after the correction factor was applied to the unshaded radiance prior to the calculation of TOA

reflectance. The mean aerosol reflectance calculation and subsequent partitioning of reflectance were carried out normally for the points in Fig. 33.
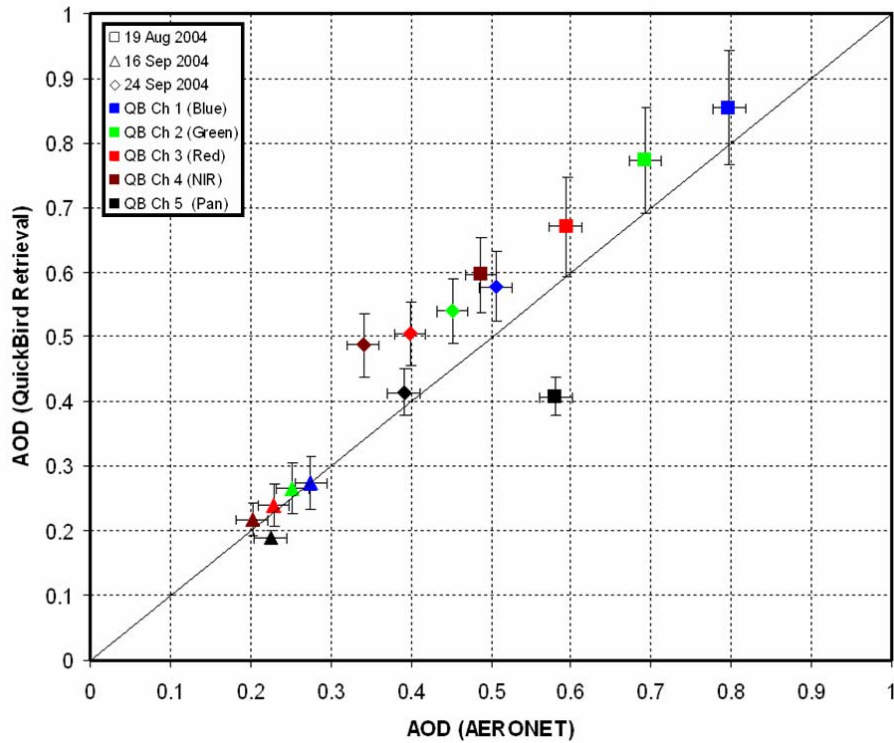
Figure 33.   Mean shadow-based AOD retrievals over desert backgrounds for 19 August, 16 September, and 24 September 2004 in the vicinity of the MAARCO site with a gaseous absorption correction applied to the panchromatic AOD retrievals.

In the case of 19 August 2004, the effects of cloud proximity must be considered as a potential source of error. As discussed in Chapter IV, Wen *et al.* (2001) showed that clouds can cause a scene wide increase in apparent surface reflectance as well as increased AOD with a decrease in the mean cloud-free distance to the target. Retrieved AOD error as a function of mean cloud-free distance along the principle solar plane is shown in Fig. 34. While there were only seven target sites, there is not an apparent relationship between error in the AOD retrieval and the target's proximity to clouds in the image.
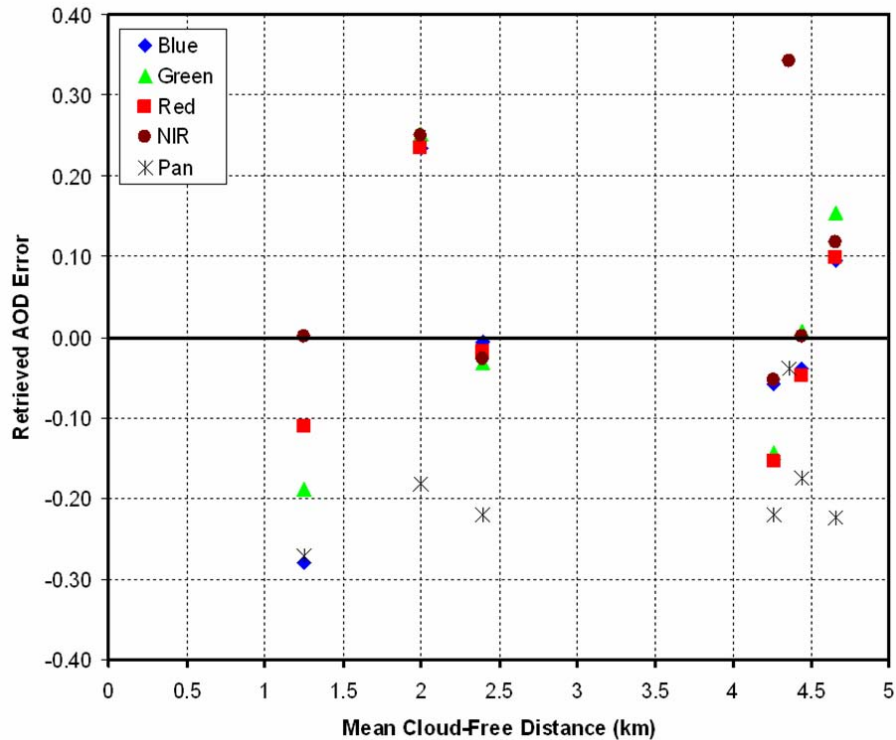
Figure 34.   Retrieved AOD error as a function of mean cloud-free distance along the principle solar plane for the 19 August 2004 case.

Finally, the last source of error to be considered is that due to the adjacency effect, or brightening of the darker pixels by the brighter surface nearby. The magnitude of the adjacency effect is determined by the amount of scattering particles in the atmosphere and the spatial extent of the effect is proportional to the scale height of the scattering layer. In all three cases considered, most of the image is covered by highly reflective surfaces and is therefore subject to the adjacency effect. In the three desert cases, the high bias in retrieved AOD increases with AOD. Finally, the impact of the adjacency effect on unshaded radiance and the resulting increase in apparent TOA reflectance are consistent with the offsetting errors seen in conjunction with the low bias in surface reflectance inherent in the shadow-based AOD retrieval method.

90

E. INVESTIGATION OF COLOCATED TARGETS IN MULTIPLE IMAGES

The QuickBird images for 16 September 2004 and 24 September 2004 cover nearly identical areas and are only eight days apart. This provides an excellent opportunity to investigate the consistency of the surface reflectance retrievals and AOD retrievals between days. This also allows comparison of the mean of the retrievals for multiple points from the same highly reflective background with the mean of the retrievals taken from a variety of highly reflective backgrounds. Ten targets common to both the 16 and 24 September images were selected for their consistent background and shadowing structures and can be seen in Fig. 35.
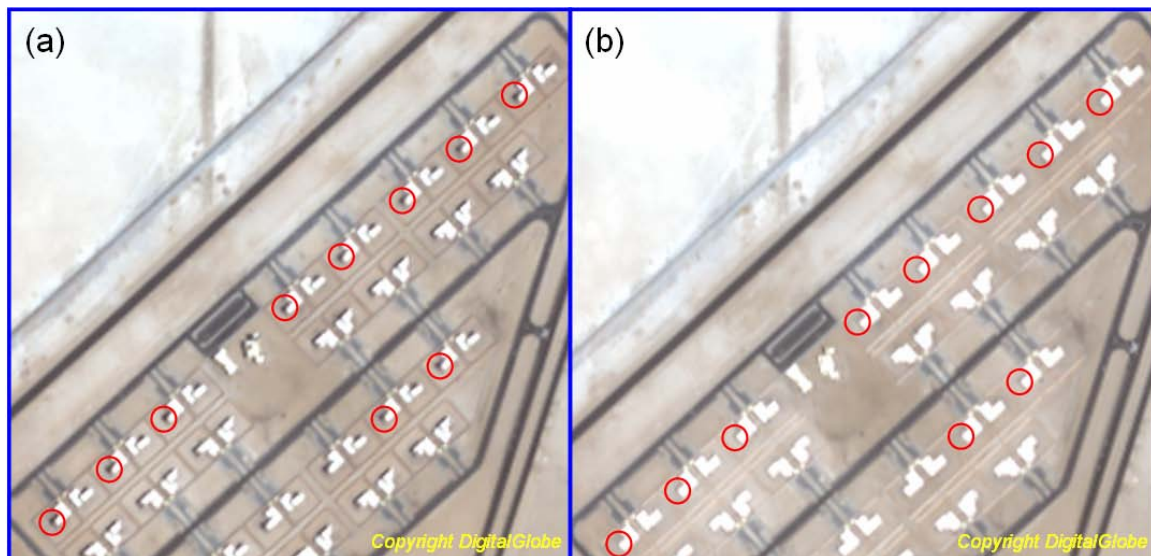
Figure 35.   Ten shadow targets (red circles) common to the (a) 16 September 2004 QuickBird image and the (b) 24 September 2004 QuickBird image (courtesy of DigitalGlobe).

1.   QuickBird-derived Surface Reflectance Comparisons

An initial assumption of the shadow-based AOD retrieval method is that retrievals are made over a homogeneous, Lambertian surface. Comparison of the QuickBird-derived surface reflectances for the collocated targets in the 16 and 24 September 2004 images, as seen in Fig. 36, show that values for each site are highly correlated and that the surface reflectances from the 24 September image are higher than the 16 September

case by 0.02 to 0.03 for the multispectral values. The linear fit of the panchromatic channels suggest higher values of approximately 0.11 for the surface reflectances from the 24 September image compared to 16 September, although the individual data points suggest that the difference is highly uncertain and is likely of the same order as that of the multispectral surface reflectances. This difference in surface reflectance is consistent with an increased adjacency effect from the higher optical depth on 24 September, caused by increased backscatter from the incoming solar radiation due to the small relative azimuth between the sensor and the sun, or both. Without more cases covering a range of AODs and solar/sensor geometries, the magnitude of the effects of each factor can not be isolated.
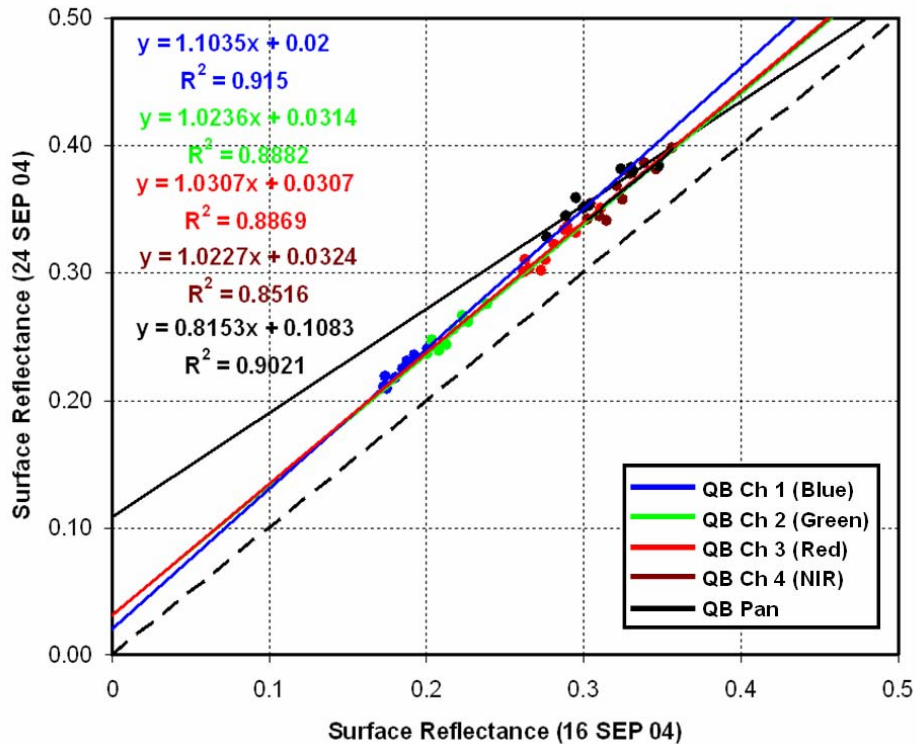
Figure 36.   Comparison of QuickBird-derived surface reflectances for 16 September 2004 and 24 September 2004 for 10 targets common to both images.

2. Comparison of Mean AOD Values from Varied and Single Backgrounds

Every effort was made in the initial investigation to choose shadow targets over a variety of bright backgrounds to prevent a bias to one particular surface type. With ten targets common to both the 16 and 24 September images, it is now possible to characterize the impact of background type bias on the mean AOD. In Fig. 37, the 24 September means for the single background showed as much as a 190% high bias. At lower optical depths, as in the case of 16 September, however, the correlation was almost exact. One would expect the standard error for the multiple background types to be larger than the standard error for a single background type due to consistency in surface reflectance. This is seen in the 16 September case and the panchromatic channel for the 24 September case, however, the standard error for the multispectral channels in the 24 September case show roughly equivalent standard error for both single and multiple backgrounds. The cause of the exceptionally high bias in the common targets for the 24 September case is difficult to isolate. While a higher AOD may cause some of the bias and increased standard error, unfavorable viewing geometry and small-scale adjacency effects, as demonstrated in Fig. 26, are the largest sources of error in the 24 September case. As with surface reflectance, without further tests under a variety of controlled conditions, the role of each factor is difficult to ascertain.
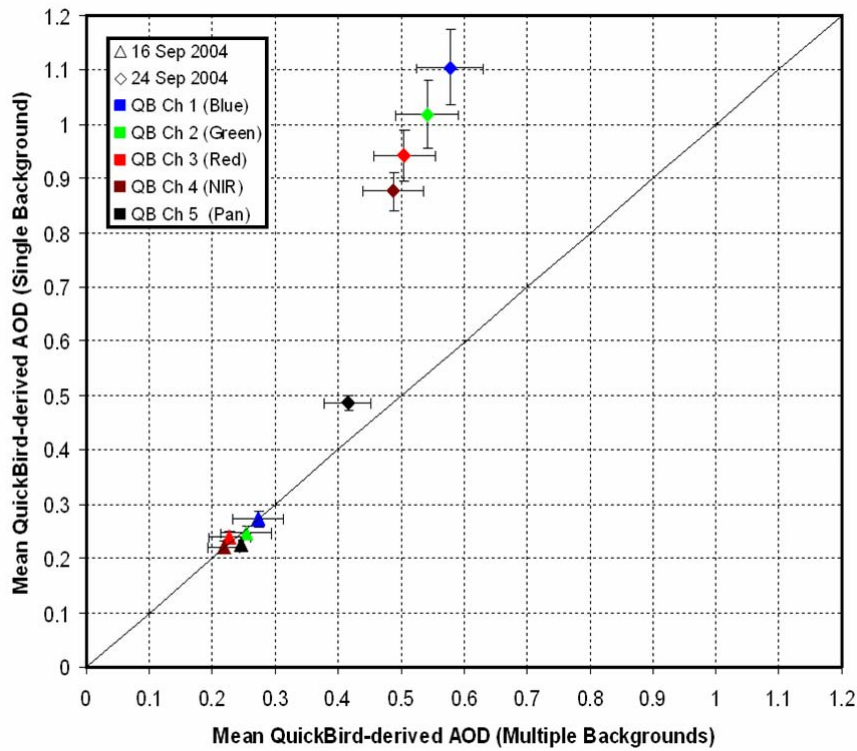
Figure 37.   Comparison of mean QuickBird-derived AOD values determined from multiple background types and mean QuickBird-derived AOD values from single background types with standard error for each denoted by the bars.

F.   SUMMARY OF THE DESERT BACKGROUND INVESTIGATION

Overall, the shadow-based AOD retrieval method performed well in the three cases considered. Large discrepancies were seen in comparisons between QuickBird-derived surface reflectances and surface reflectances consistent with the AERONET AOD retrievals, however, errors were found to be largely balanced between high and low biases of nearly equal magnitude. Sources of error were considered. While definitive statements are not possible without controlled experiments, errors were consistent with the systematic low bias due to surface reflectance that is offset by a high bias in surface reflectance due to image-wide adjacency effects. Ten targets common to both the 16 and 24 September images were examined for consistency in surface reflectance as well as single background bias in target selection. The 16 September case showed almost no difference in area-averaged AOD values based on a single background or multiple backgrounds. The 24 September image showed a significant high bias for mean AOD

based on a single background type. While the biases seen in the 24 September case are consistent with small scale adjacency effects and/or unfavorable solar/sensor geometry, definitive statements about the biases are impossible with more cases under a variety of conditions and geometries. Target selection criteria suggested in Chapter IV were mostly met due to the high surface reflectance and high unshaded/shaded radiance differences. Additional requirements for a minimum relative azimuth would facilitate access to the shadow as well as prevent contamination of the unshaded/shaded radiance difference through small scale adjacency effects.

THIS PAGE INTENTIONALLY LEFT BLANK

IX. URBAN BACKGROUND INVESTIGATION

A. OVERVIEW

The second investigation of the new shadow method for AOD retrieval focused on the applicability of the method to AOD retrievals in urban areas. Urban areas present a unique challenge for AOD retrievals due to complexity and the general absence of large, deep bodies of water or dense, dark vegetation required for the dark object method of AOD retrieval. Current operational satellite AOD retrievals typically have a spatial resolution of approximately ten kilometers, roughly comparable in size to one QuickBird scene. The shadow method, when applied to urban scenes, may allow the user to quantify spatial variations of AOD at higher resolutions. Additionally, the shadow method may allow researchers to monitor the effects of aerosol particle point sources remotely.

B. OBSERVATIONAL DATA

Chapter VII provides thorough descriptions of the QuickBird commercial satellite imagery and AERONET AOD data were used in this investigation. Below is a description of the six individual scenes and their accompanying AERONET data used in the urban background investigation.

1. Beijing, China, 08 July 2003

The QuickBird satellite image of Beijing, China on 08 July 2003 was obtained from the CSIL and consisted of both panchromatic and multi-spectral imagery. Figure 38(a) is a MODIS overview of eastern China. Ten shadow sites, marked with green circles in Fig. 38(b), were chosen in the QuickBird image around the AERONET site located at the Institute of Atmospheric Physics (39.98N-116.38E), marked with a red square. As a part of a mosaic constructed at NGA, the image covers an area approximately 9.6 kilometers by 9.5 kilometers, slightly smaller than the standard QuickBird image. Exact time and solar/viewing geometries are provided in Table 8.
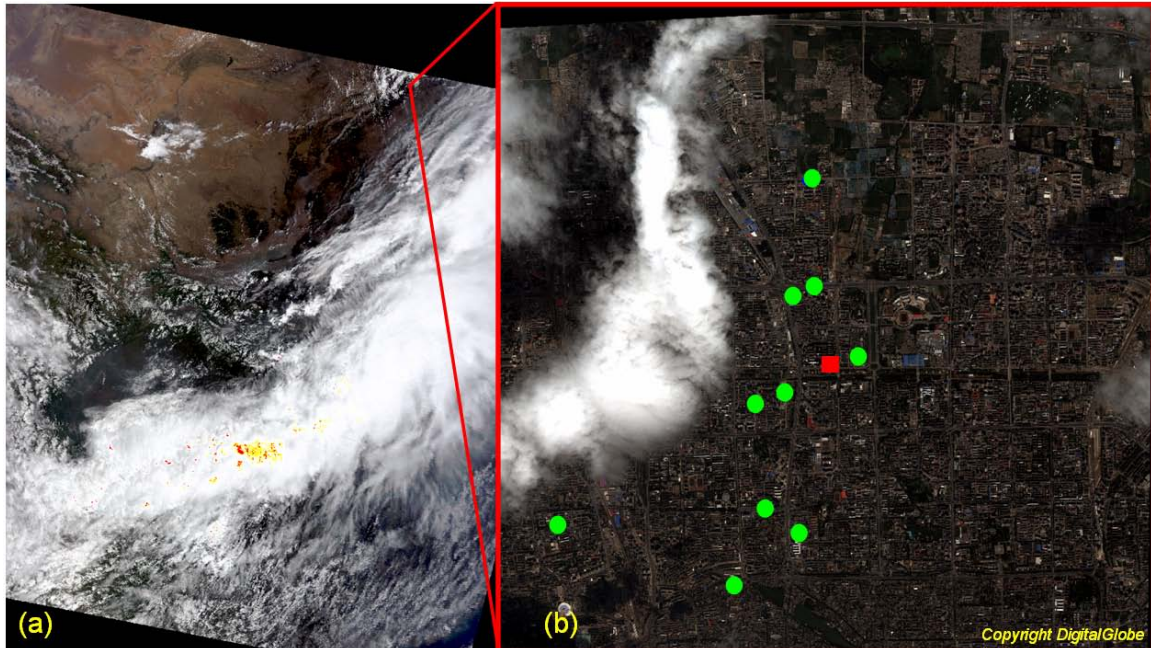
Figure 38.   A MODIS Terra overview (a) of eastern China for 08 July 2003 and (b) the QuickBird RGB image of Beijing for the same day and time with urban background shadow retrieval targets marked with green circles and the AERONET site marked with a red box. Red lines indicate the location of the QuickBird image in the larger MODIS image (QuickBird image courtesy of DigitalGlobe).

AERONET data collected at the Beijing site at 02:50 and 03:05 UTC were averaged and used for comparison with mean QuickBird-derived AOD values. Level 2.0 data were available for only the 440 nm, 675 nm, 870 nm, and 1020 nm channels.

2.   Taipei, Taiwan, 07 November 2003

The QuickBird satellite image of Taipei, Taiwan on 07 November 2003 was also obtained from the CSIL and consisted of both panchromatic and multi-spectral imagery. Figure 39(a) is a MODIS overview of the Taiwan and the East China Sea. Ten shadow sites, marked with green circles, were chosen in the QuickBird image around the AERONET site located at the Central Weather Bureau Headquarters (25.03N-121.50E), marked by the red square in Fig. 39(b). Like the Beijing image, the area covered by this image is slightly smaller than the standard image size at 9.7 kilometers by 9.7. Again, the exact time and solar/viewing geometries are provided in Table 8.
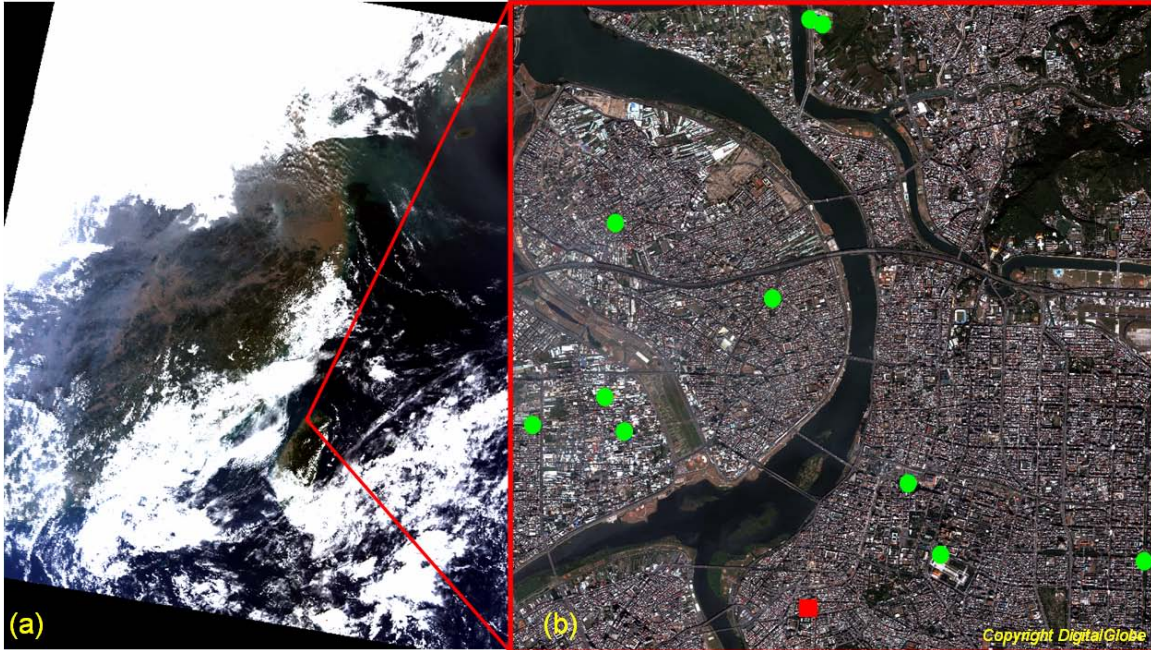
Figure 39.   A MODIS Terra overview (a) of the East China Sea and Taiwan for 07 November 2003 and (b) the QuickBird RGB image of Taipei, Taiwan for the same day and time with urban background shadow retrieval targets marked with green circles and the AERONET site marked with a red box. Red lines indicate the location of the QuickBird image in the larger MODIS image (QuickBird image courtesy of DigitalGlobe).

AERONET data collected at the Taipei site at 02:08 UTC were used for this AOD comparison and consisted of Level 2.0 data for the 340 nm, 380nm, 440 nm, 500 nm, 675 nm, 870 nm, and 1020 nm channels.

3.   New York City, New York, 02 August 2002

The QuickBird satellite image of New York City, New York on 02 August 2002 was obtained from the CSIL and consisted of both panchromatic and multi-spectral imagery covering the AERONET site located at the Engineering Building of the City College of New York City (40.82N-73.95W). Figure 40(a) is the MODIS overview of the northeastern United States. Again, ten shadow targets (green circles) were chosen in the QuickBird image around the AERONET site (red square) as seen in Fig. 40(b). This image covered the standard QuickBird scene area of 16.5 kilometers by 16.5 kilometers. Exact time and solar/viewing geometries are again provided in Table 8.
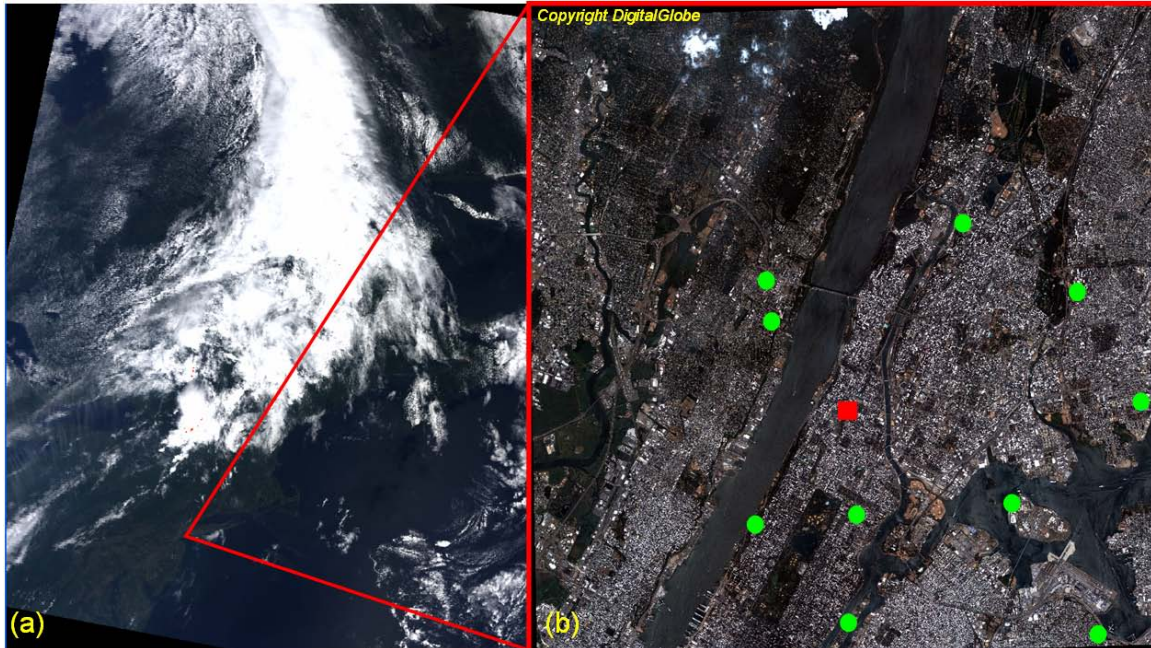
Figure 40.   A MODIS Terra overview (a) of the northeastern United States for 02
August 2002 and (b) the QuickBird RGB image of New York, New York
for the same day and time with urban background shadow retrieval targets
marked with green circles and the AERONET site marked with a red box.
Red lines indicate the location of the QuickBird image in the larger MODIS
image (QuickBird image courtesy of DigitalGlobe).

AERONET data collected at the New York City site at 15:50 UTC were
used for comparison with the mean QuickBird-derived AOD values and consisted of
Level 2.0 data for the 340 nm, 380nm, 440 nm, 500 nm, 675 nm, 870 nm, and 1020 nm
channels.

4.   Buenos Aires, Argentina, 22 February 2002

The QuickBird satellite image of Buenos Aires, Argentina on 22 February 2002
was obtained from the CSIL and consisted of both panchromatic and multi-spectral
imagery.   A MODIS overview of eastern Argentina is shown in Fig. 41(a).   The
QuickBird image, seen in Fig. 41(b), is located approximately one kilometer east of the
AERONET site located at the CEILAP Laboratory approximately 15 km south of central
Buenos Aires (34.57S-58.50W).   The green circles in Fig. 41(b) again mark the shadow
target sites.   Although part of a mosaic, the imagery covered an area approximately 16.5

kilometers by 15 kilometers, close to the standard scene size. Again, exact time and solar/viewing geometries are provided in Table 8.
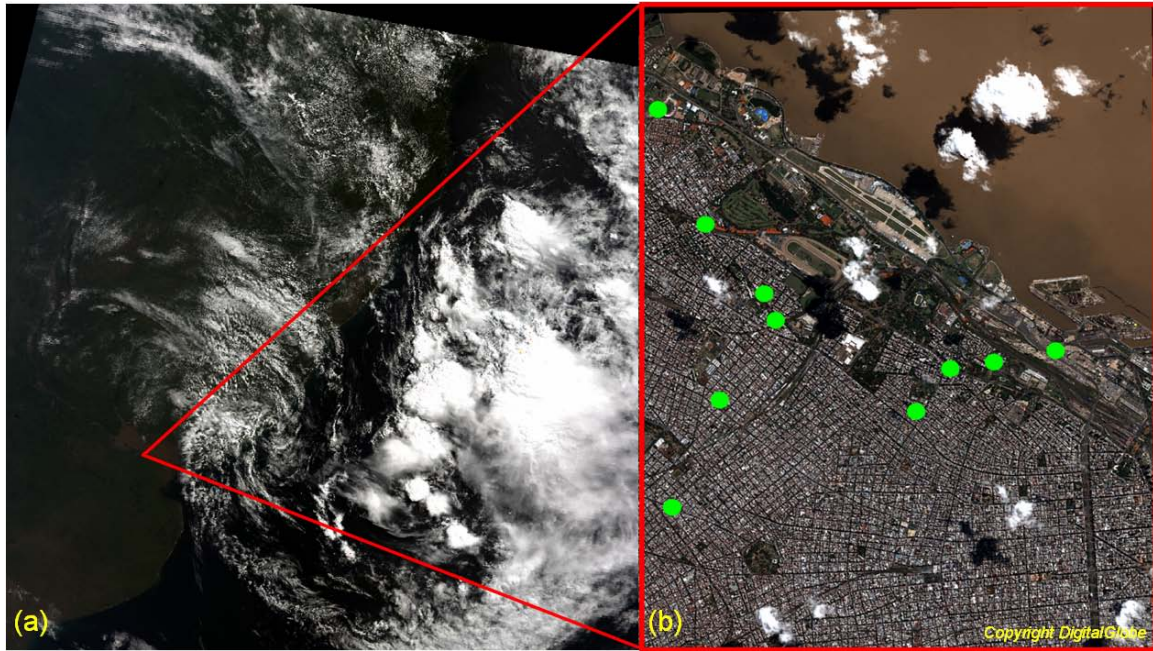
Figure 41.   A MODIS Terra overview (a) of eastern South America for 22 February 2002 and (b) the QuickBird RGB image of coastal Buenos Aires for the same day and time with urban background shadow retrieval targets marked with green circles. Red lines indicate the location of the QuickBird image in the larger MODIS image (QuickBird image courtesy of DigitalGlobe). Note: The AERONET site is approximately one kilometer west of the western edge of the QuickBird image.

AERONET data collected at the Buenos Aires site at 13:54 UTC were used for this comparison and consisted of Level 2.0 data were available for the 340 nm, 380nm, 440 nm, 500 nm, 675 nm, 870 nm, and 1020 nm channels. The 380 nm and 440 nm channels were excluded the data were too low to provide a good spectral fit. Eck (2005) investigated the source of the errors and found that the errors were within the accepted tolerances for AERONET, however, due to the low AOD, the error was of the same magnitude as the measured AOD. This remained a consistent problem with all AERONET data from Buenos Aires.

5.   Buenos Aires, Argentina, 22 March 2004

The QuickBird satellite image of Buenos Aires, Argentina on 22 March 2004 was obtained from the CSIL and consisted of both panchromatic and multi-spectral imagery. Figure 42(a) is a MODIS overview of eastern Argentina. The QuickBird image did cover the AERONET site located at the CEILAP Laboratory (34.57S-58.50W), denoted by the red square in Fig. 42(b) along with ten shadow sites marked by green circles.   The imagery roughly covered the standard scene area of 16.5 km by 16.5 km. Exact time and solar/viewing geometries are provided in Table 8.
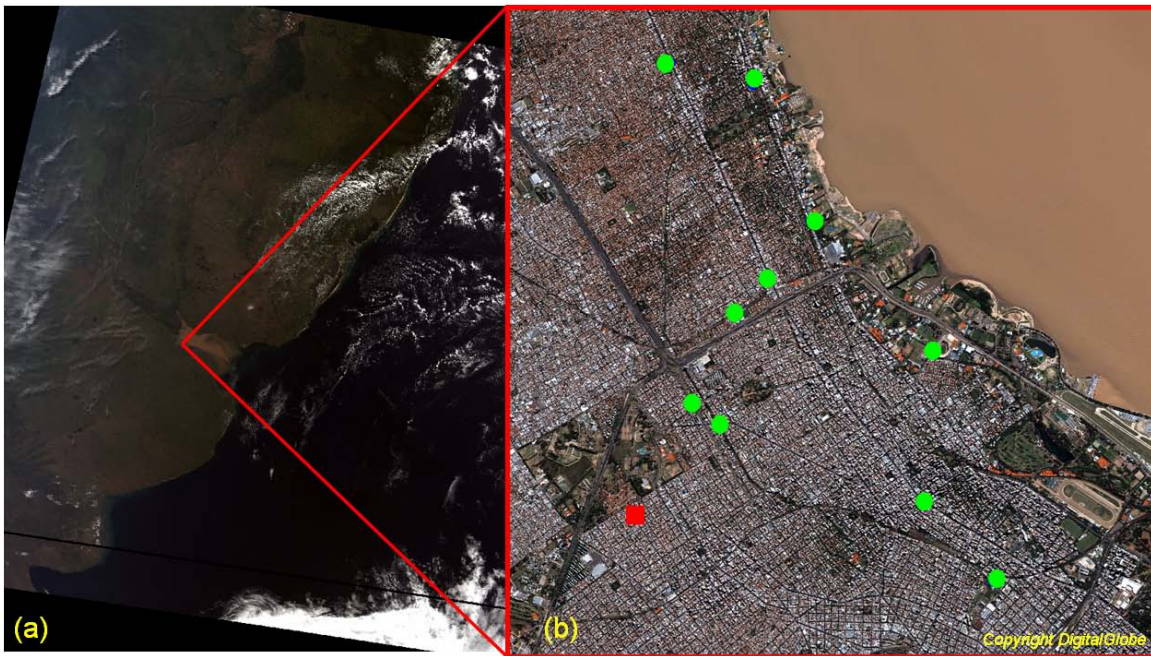
Figure 42.   A MODIS Terra overview (a) of eastern South America for 22 March 2004 and (b) the QuickBird RGB image of coastal Buenos Aires for the same day and time with urban background shadow retrieval targets marked with green circles and the AERONET site marked with a red box. Red lines indicate the location of the QuickBird image in the larger MODIS image (QuickBird image courtesy of DigitalGlobe).

AERONET data collected at the Buenos Aires site at 13:46 UTC were used for this comparison. Level 2.0 data were available for the 340 nm, 380nm, 440 nm, 500 nm, 675 nm, 870 nm, and 1020 nm channels, but, as in the 22 February case, the 380 nm and 440 nm channels were excluded as the data were too low to provide a good spectral fit.

6. Buenos Aires, Argentina, 06 November 2004

The QuickBird satellite image of Buenos Aires, Argentina on 06 November 2004 was obtained from the CSIL and consisted of both panchromatic and multi-spectral imagery. Figure 43(a) is a MODIS overview of eastern Argentina. The QuickBird image again covered the AERONET site located at the CEILAP Laboratory (34.57S-58.50W). The ten shadow sites (green circles) and the AERONET site (red square) are shown in Fig. 43(b). As part of a mosaic, this image covered an area approximately 10 km by 19 km. Again, exact time and solar/viewing geometries are provided in Table 8.
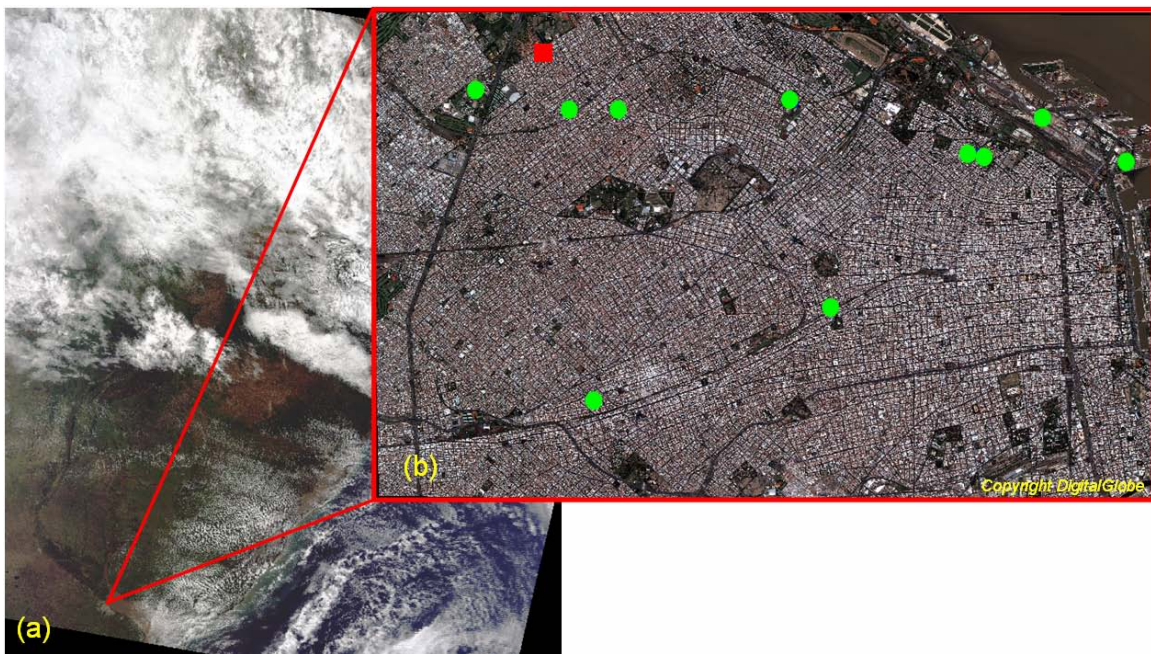
Figure 43.   A MODIS Terra overview (a) of eastern South America for 06 November 2004 and (b) the QuickBird RGB image of coastal Buenos Aires for the same day and time with urban background shadow retrieval targets marked with green circles and the AERONET site marked with a red box. Red lines indicate the location of the QuickBird image in the larger MODIS image (QuickBird image courtesy of DigitalGlobe).

AERONET data collected at the Buenos Aires site at 13:54 UTC were used for this comparison. Level 2.0 data were available for the 340 nm, 380nm, 440 nm, 500 nm, 675 nm, 870 nm, and 1020 nm channels, however, the 380 nm, 440 nm, 500 nm, and 675 nm channels were again excluded from this fit as the data were either too low or too high to provide a good spectral fit.

103

Table 8.   Location, date, time, solar/viewing geometry and cloud cover for the
             QuickBird imagery used in the urban background investigation.

Location	Date	Time (UTC)	Satellite Zenith	Satellite Azimuth	Solar Zenith	Solar Azimuth	Cloud Cover
Beijing	08 Jul 03	02:56	29.3°	008.7°	24.7°	128.1°	20%
Taipei	07 Nov 03	02:16	11.0°	079.5°	45.5°	152.2°	0
New York	02 Aug 02	15:49	22.2°	005.7°	27.8°	140.2°	0
Buenos Aires	22 Feb 02	14:00	10.6°	104.9°	37.8°	057.7°	10%
Buenos Aires	22 Mar 04	13:46	19.2°	098.3°	47.4°	049.0°	0
Buenos Aires	06 Nov 04	03:57	19.1°	102.0°	28.9°	057.2°	0

C.   AEROSOL CHARACTERIZATION

An investigation of the shadow method in the urban environment provided not only a variety of background surface reflectances, but also a variety of potential aerosol particle types. The shadow method is not extremely sensitive to the accuracy of the parameters used to describe the aerosol particles, asymmetry parameter and single scatter albedo. While AERONET inversions for asymmetry parameter and single scatter albedo values were not available for these cases, aerosol climatology for many urban sites suggest values range from approximately 0.60 to 0.70 and 0.90 to 0.97 for these parameters respectively. For this investigation, an asymmetry parameter of 0.65 and a single scatter albedo of 0.95 were used as representative values for all urban cases except Beijing. For the Beijing case, the same asymmetry parameter is used, but a more representative single scatter albedo of 0.88 is used (Xiang-Ao *et al.* 2005). Based on visual inspection of the imagery, none of the cases used are experienced heavy loading of any particular aerosol that would violate the assumptions above.

D.   RESULTS

1.   Mean QuickBird-retrieved Aerosol Optical Depths

The mean of all shadow-based AOD retrievals for the moderate AOD urban cases, annotated by location and QuickBird channel, are shown in Fig. 44. The mean of all shadow-based AOD retrievals for low AOD urban cases (all in Buenos Aires), annotated by date and QuickBird channel, are shown in Fig. 45. As in the previous chapter, the standard error of the mean is annotated by error bars in the y-direction, while the uncertainty of the AERONET data, ± 0.02, is shown in the x-direction. While the spectral distribution of the retrievals for each day follows the expected distribution (decreasing AOD with increasing wavelength), only the green and near-infrared channels for the Taipei case approach the AERONET AOD values within their standard error. For the low AOD cases in Buenos Aires, none of the days shows a good correlation between QuickBird-derived and AERONET AODs. In all low AOD cases, the AERONET AOD is approximately 0.05 or below and is roughly at or below the uncertainty of ± 0.04 for the shadow-based AOD method determined in Chapter V. While AOD retrievals in the urban environment were not as good as those in the desert background investigation, careful target selection can potentially provide a significant improvement. Additionally, an investigation of the possible sources of error can provide clues to additional areas of improvement. Understanding the causes of such large errors can lead to possible corrections, and if corrections are not possible, at least reinforce or add to minimal target criteria necessary for usable AOD retrievals and assist in determining the limitations of the method.
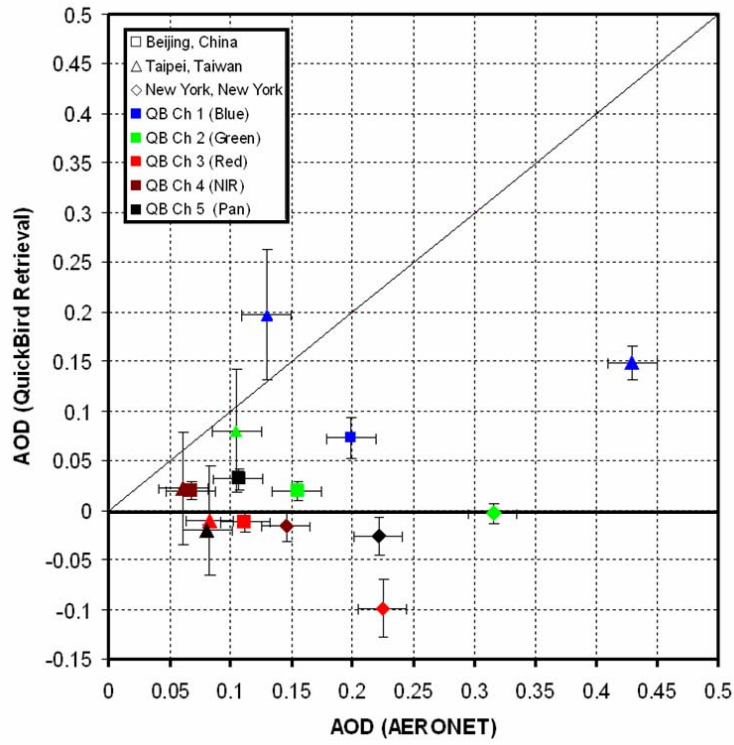
Figure 44.   Mean shadow-based AOD retrievals with associated standard error over urban backgrounds for Beijing, China, Taipei, Taiwan, and New York, New York as compared to collocated AERONET AOD measurements.
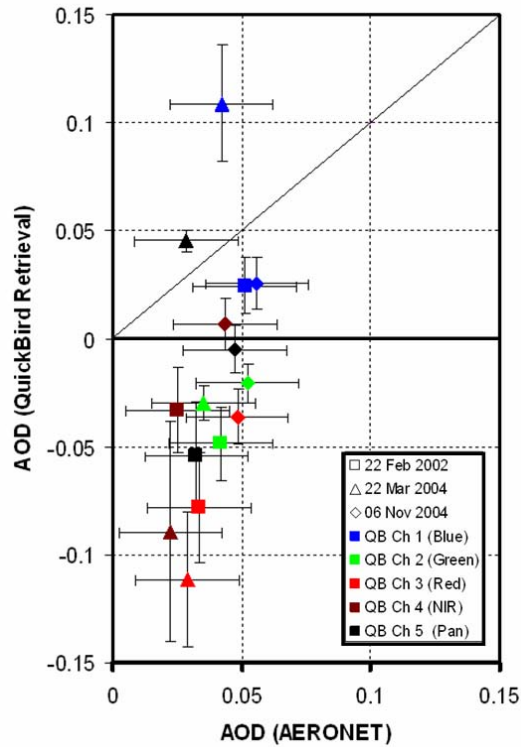
Figure 45.   Mean shadow-based AOD retrievals with associated standard error over urban backgrounds for 22 February 2002, 22 March 2004, and 06 November 2004 for Buenos Aires, Argentina as compared to collocated AERONET measurements.

2.   Surface Reflectance Retrievals

As in Chapter VIII, QuickBird-derived surface reflectances were compared to the surface reflectance determined from the AERONET AOD values, holding all other parameters constant for each site.   Again, mean aerosol reflectance for all surface reflectance retrievals was calculated based on the AERONET AOD.

Originally intended for the highly reflective surfaces of the desert, the highly reflective nature of the concrete, especially in the near-infrared, found in the urban environment was evaluated for its suitability to the shadow-based AOD retrieval method. For the moderate AOD cases, the range of surface reflectances runs from 0.03 to just below 0.3 with most surface reflectances falling well below 0.15 as seen if Fig. 46. These surface reflectances represent a range of concrete and asphalt surfaces typically found in the urban areas.   Comparing the QuickBird-derived surface reflectance to the surface reflectance required by the AERONET-measured AOD, one can see that they are

highly correlated and show that the QuickBird-derived surface reflectances have a consistent low bias of approximately 0.03 to 0.05.
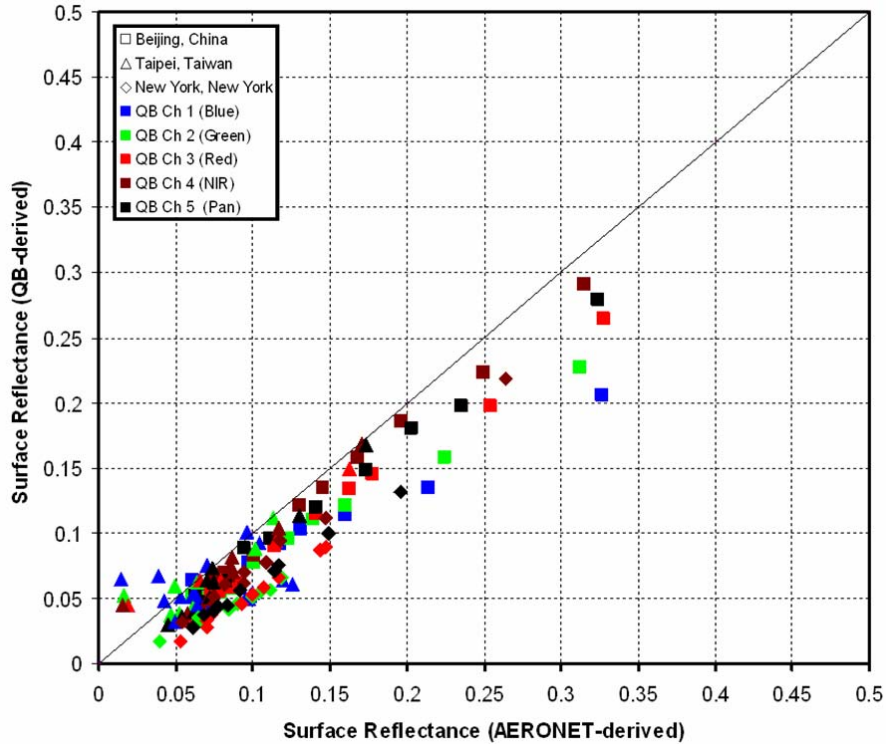
Figure 46.   Comparison of QuickBird-derived surface reflectances as determined from measured unshaded radiance to surface reflectance required to obtain the AERONET-derived AOD for the moderate AOD cases (Beijing, Taipei, and New York).

For the low AOD urban cases shown in Fig. 47, QuickBird-derived surface reflectance values ranged from 0.02 to 0.35, however most values were 0.25 or below. Like the moderate AOD cases, the low AOD cases show excellent correlation with only a low bias of 0.02 to 0.03 seen in the QuickBird-derived surface reflectances. The smaller bias seen in the low AOD cases likely stems from the fact that mean aerosol reflectance is proportional to the aerosol optical depth and therefore less surface reflectance is lost to mean aerosol reflectance in the partitioning of the top of the atmosphere reflectance.
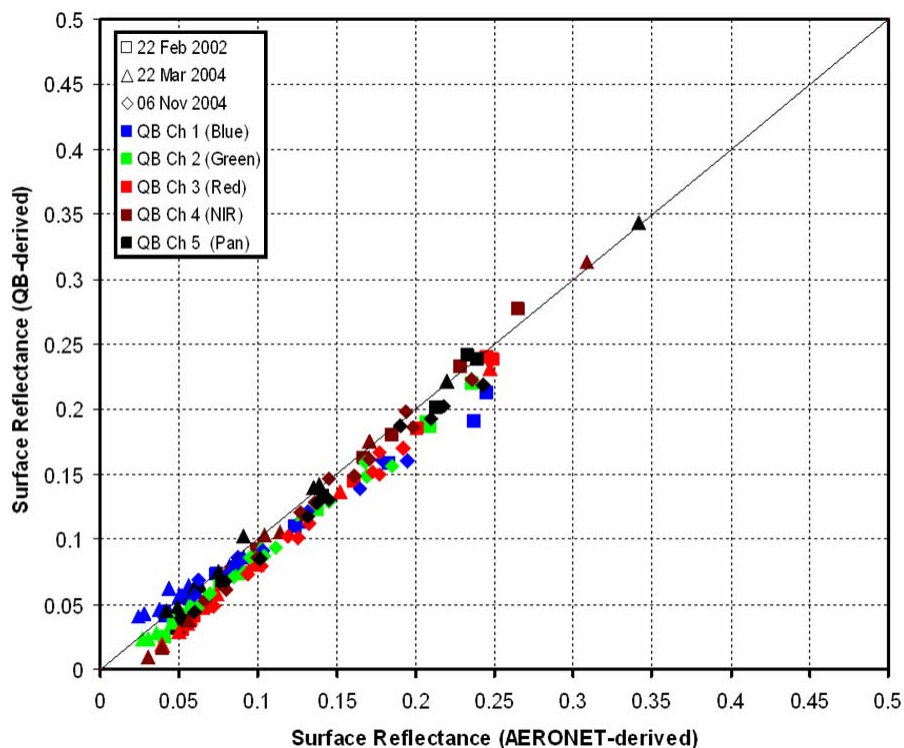
Figure 47.   Comparison of QuickBird-derived surface reflectances as determined from measured unshaded radiance to surface reflectance required to obtain the AERONET-derived AOD for the low AOD cases (Buenos Aires).

3.   Sources of Error

As before, specific sources of error cannot be conclusively identified without further experiments in a controlled environment, yet observed errors can be determined to be consistent or not consistent with known sources of error. Again, factors that are well described and taken as constant, such as solar and satellite zenith angles, will be excluded from this investigation in favor of focusing on surface reflectance and mean aerosol reflectance.

a.   Unshaded/Shaded Radiance Difference

Again, the unshaded/shaded radiance difference is one possible source of error. This is the primary measured signal on which the shadow-based AOD retrieval method is based and the error in the retrieved AOD is expected to decrease as the difference increases. In the moderate AOD cases shown in Fig. 48, the error in retrieved AOD generally decreases up to differences of approximately 40 W m^{-2} sr^{-1} nm^{-1}, however

most errors are negative (low bias) and grouped between differences of 10 and 30 W m^{-2} sr^{-1} nm^{-1}. The largest errors and the only site with a high bias to all multispectral retrievals have unshaded/shaded radiance differences below 10 W m^{-2} sr^{-1} nm^{-1}. Upon inspection, this can be attributed to a small scale adjacency effect due to a highly reflective surface next to the relatively dark background that the shadow falls across. The minimum unshaded/shaded radiance difference of 10 W m^{-2} sr^{-1} nm^{-1} suggested in Chapter IV would do little to remove most of the erroneous retrievals in these cases.
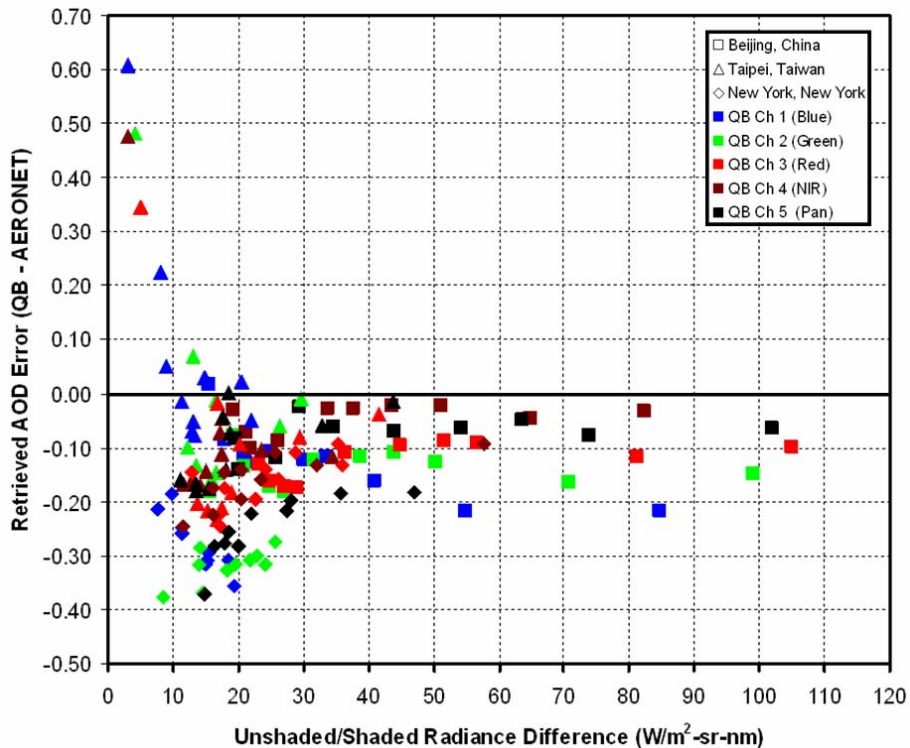
Figure 48.   Shadow-based AOD retrieval error as a function of unshaded/shaded radiance difference for all moderate AOD urban background cases (Beijing, Taipei, and New York).

An additional source of error in the unshaded/shaded radiance difference may be the loss of diffuse irradiance due to structures around the shadowed area. The diffuse sky irradiance blocked by surrounding structures is inversely proportional to the distance from the shadowed area such that closer structures block more of the diffuse field. Therefore, shadows in the "urban canyon" formed by high-rise buildings typical of most urban areas will have less diffuse irradiance causing an artificial increase the

unshaded/shaded radiance difference and a decrease in the retrieved AOD. A minimum-required distance from other structures would provide another targeting constraint in the urban environment. Determining the exact value of this stand-off distance will require further study.

In the low AOD cases, the retrieved AOD error shows more of the expected decrease with increased unshaded/shaded radiance difference as seen in Fig. 49. Again, the largest errors are grouped between difference of 10 and 30 W m^{-2} sr^{-1} nm^{-1} and decrease to a roughly consistent value of 0 to 0.1 for differences greater than 40 W m^{-2} sr^{-1} nm^{-1}. As the AOD is very low, very few of the sites have an unshaded/shaded radiance difference of 10 W m^{-2} sr^{-1} nm^{-1} or less such that minimum target criteria based on radiance difference would do little to improve the final result.
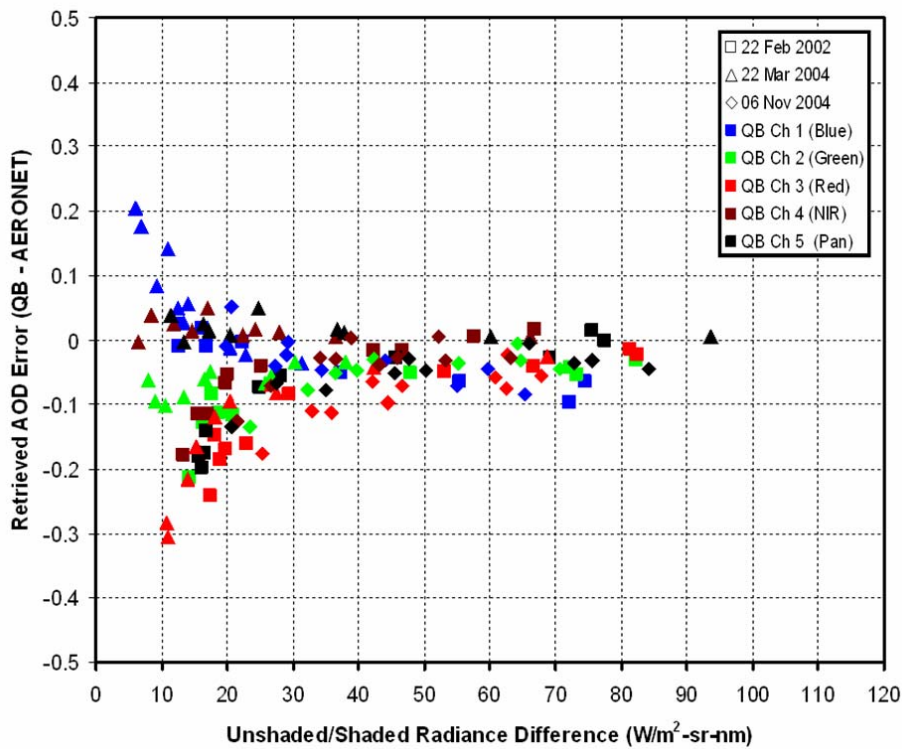
Figure 49.   Shadow-based AOD retrieval error as a function of unshaded/shaded radiance difference for all low AOD urban background cases (Buenos Aires).

As discussed in the previous chapter, the unshaded/shaded radiance difference seems immune to most factors that would affect measured radiance, as both the unshaded and shaded regions are affected equally and the difference is preserved. Again, small scale adjacency effects can cause an unwarranted decrease in the unshaded/shaded radiance difference, however this phenomenon is highly dependent on the solar/sensor geometry and quite obvious upon visual inspection. Guaranteed access to the shaded area based on a minimum allowable relative azimuth difference between solar and satellite viewing geometries can also preclude this contamination.

Error due to sub-pixel illumination or shading as discussed in Chapter VIII remains a potential source of error, but can be mitigated by data collection strategies (e.g., using mode radiance values vice mean radiance values). Another consideration for data collection strategies in urban areas is the proximity of other structures, especially tall ones, in the vicinity of the shadow used. Highly reflective structures, such as glass office buildings, can reflect both diffuse and direct light in to the shaded region and decrease the measured radiance difference. This source of error can be mitigated by using minimum target shadow stand-off distances from other structures as well as by visual inspection.

b.   *Surface Reflectance/Mean Aerosol Reflectance*

Surface reflectance provides the largest potential source of error in the shadow-based AOD retrieval method as the unshaded radiance on which surface reflectance is based is subject to all fluctuations in the diffuse radiance field. The moderate AOD cases shown in Fig. 50 show a rough decrease in the absolute retrieved AOD error with increasing surface reflectance. Points with the largest absolute error have surface reflectance values well below the suggested minimum value of 0.15. The low AOD cases, as shown in Fig. 51, again show the expected decrease in retrieved AOD error with increasing surface reflectance. Here, retrieved AOD error decreases rapidly between surface reflectances of 0.03 and 0.10 and remain consistent at approximately 0 to 0.05 for surface reflectances greater than 0.10. Again, to better explore the sources of error, error in retrieved AOD as a function of error in surface reflectance will be examined.
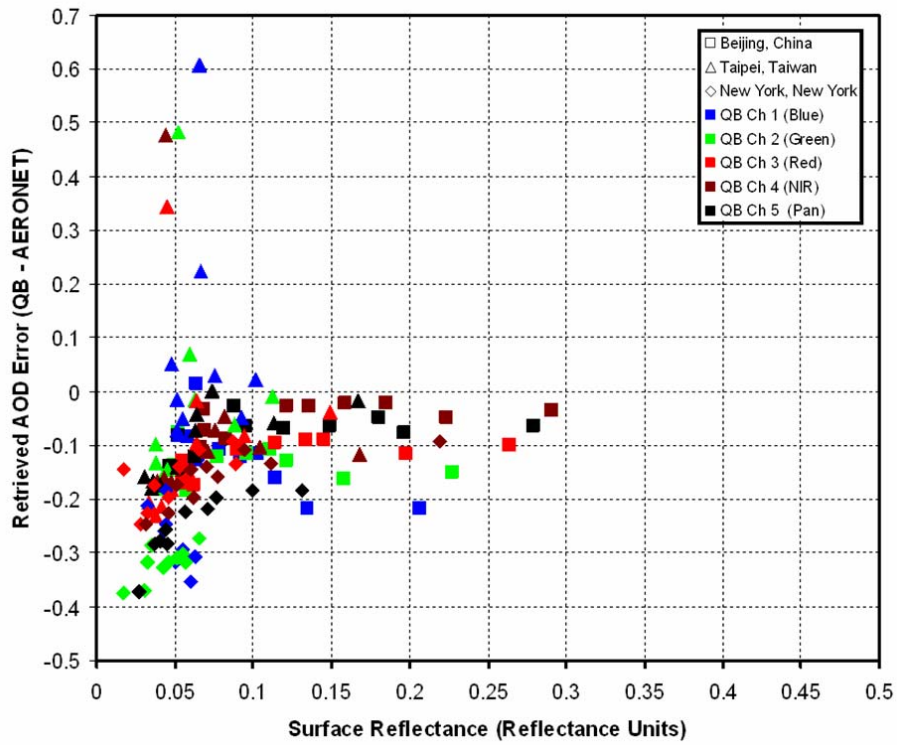
Figure 50.   Shadow-based AOD retrieval error as a function of surface reflectance for all moderate AOD urban background cases (Beijing, Taipei, and New York).
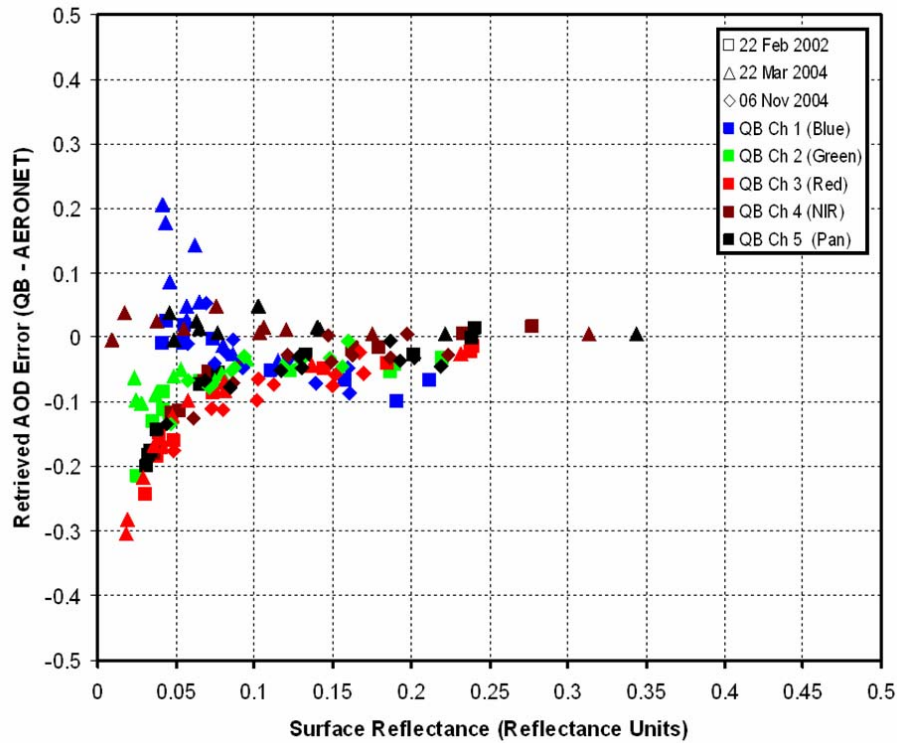
Figure 51. Shadow-based AOD retrieval error as a function of surface reflectance for all low AOD urban background cases (Buenos Aires).

As discussed above, the systematic low bias of surface reflectance due to the overestimation of mean aerosol reflectance based on the initial overestimation of total optical depth will result in a systematic low bias in the final AOD retrieval. Mean aerosol reflectance values tend toward a high bias of 0.01 to 0.1 (1% to 10%) in the moderate AOD cases and 0.01 to 0.03 (1% to 3%) in the low AOD cases resulting in a corresponding low bias to surface reflectance values. The sensitivity of the final shadow-based AOD retrieval to surface reflectance is a 0.04 increase for every 0.01, or 1%, increase in surface reflectance. The sensitivity of the final AOD retrieval to mean aerosol reflectance is a 0.002 decrease for every 0.01, or 1%, increase in mean aerosol reflectance. Therefore, for every 1% error in surface reflectance, there should be a corresponding error in AOD of 0.038 if the error were only due to the overestimation of mean aerosol reflectance and underestimation of surface reflectance. The three moderate AOD urban cases were combined in Fig. 52 and retrieved AOD error was compared to error in surface reflectance as determined above in Section D, subsection 2. The three low AOD urban cases are shown in Fig. 53.

114
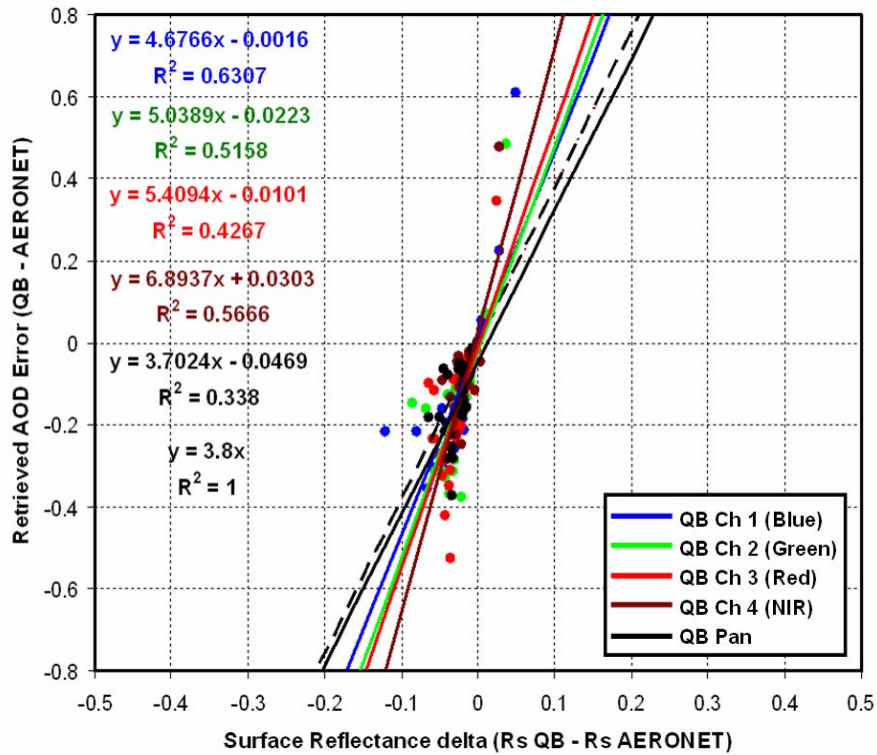
Figure 52.   Retrieved AOD error as a function of surface reflectance error for the three moderate AOD urban cases combined for each QuickBird channel. The dashed line denotes the theoretical error due to overestimation of mean aerosol reflectance and underestimation of surface reflectance combined.
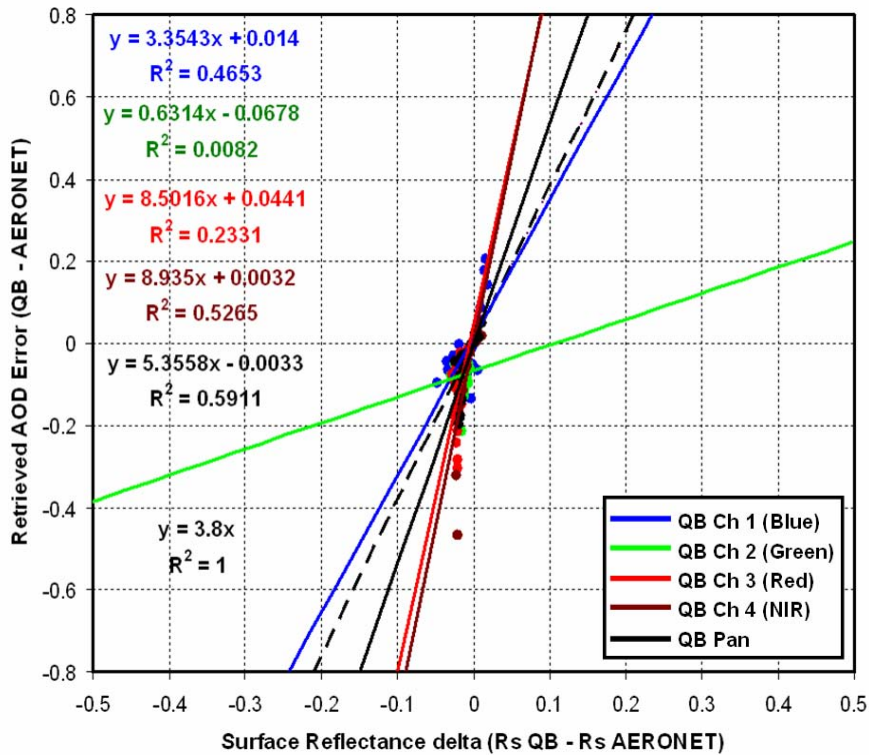
Figure 53.   Retrieved AOD error as a function of surface reflectance error for the three low AOD urban cases combined for each QuickBird channel. The dashed line denotes the theoretical error due to overestimation of mean aerosol reflectance and underestimation of surface reflectance combined.

As in the desert investigation, the relationships seen in Fig. 53 between the error in surface reflectance and the retrieved AOD error for the moderate AOD cases are generally consistent with the sensitivity analyses presented in Chapter IV, but cannot be solely attributed to the systematic underestimation of surface reflectance. One or more other factors appear to increase the retrieved AOD error above what is expected with the accompanying surface reflectance error and the magnitude of the additional error seems to be proportional to the central wavelength of the channel considered (i.e. larger errors for the near-infrared channel versus the blue channel). While some portion of the retrieved AOD error is consistent with the systematic bias of surface reflectance in the procedure, other sources of error in surface reflectance must be investigated.

In the low AOD cases, the relationships between error in retrieved AOD and error in surface reflectance are less clear. The blue channel AOD retrievals appear to agree well with the systematic surface reflectance bias. The red, near-infrared, and

panchromatic channels have error relationships that show additional error resulting in underestimation of surface reflectance, although the panchromatic retrievals are less affected than the red and near-infrared retrievals. Finally, the green channel shows a drastic deviation from the expected relationship. Low optical depths combined with low surface reflectances makes the validity of this relationship suspect at best.   For this reason, sources of error for the low AOD cases will not be explored further.

   As in the desert background investigation, factors affecting the unshaded radiance, and thus the TOA reflectance prior to partitioning, must be considered. Holekamp's (2003) post-launch calibration errors leading to underestimation of QuickBird radiance values could lead to additional errors causing further low bias to surface reflectance. Underestimates by 8.6%, 7.8%, 4.9% and 0.4% for the blue, green, red and near-infrared channels respectively, however, would imply that errors would decrease with increasing wavelength. In the moderate AOD cases, quite the opposite is the case with errors increasing with increasing wavelength. In the low AOD cases, no clear correlation between error and wavelength can be determined. Thus, errors in both cases are not consistent with sensor calibration errors.

   Gaseous absorption in the visible and near-infrared portion of the solar spectrum, while typically considered negligible, must be investigated. Gaseous absorption reduces transmittance and decreases the satellite-observed radiance, decreasing the TOA and surface reflectance and unshaded/shaded radiance difference. With few exceptions, a consistent low bias is seen for all channels. Correction factors were determined for each channel for the combined effects of carbon dioxide, oxygen, ozone, and water vapor using MODTRAN 4 based AERONET-measured precipitable water and an average mid-latitude summer. Water vapor accounted for nearly one-third to one-half of the estimated absorption. Improvements in the moderate AOD mean retrievals can be seen in Fig. 54 after the correction factor was applied to the unshaded radiance prior to the calculation of TOA reflectance. The effects of the same corrections made to the low AOD cases can be seen in Fig. 55. The mean aerosol reflectance calculation and subsequent partitioning of reflectance were carried out normally.
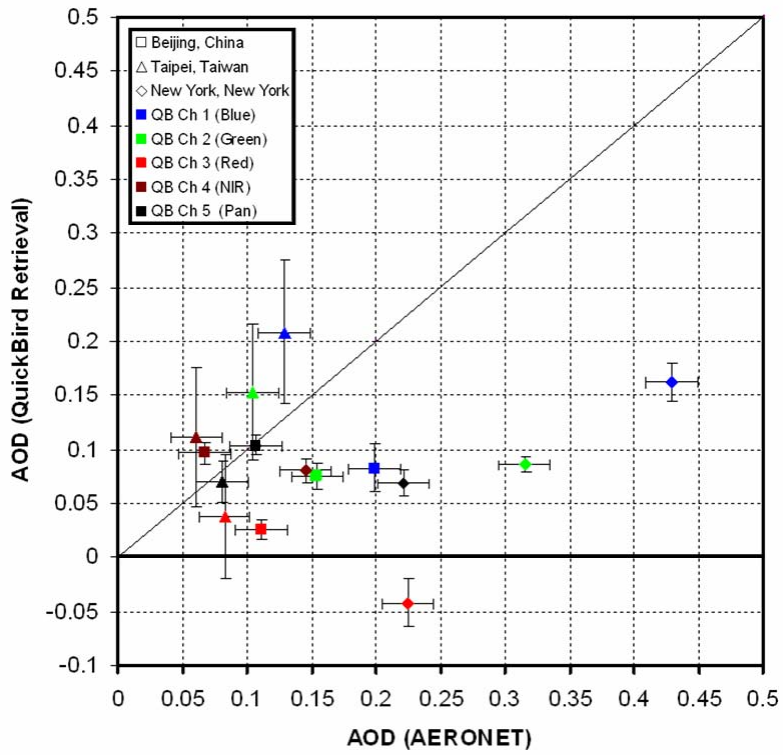
Figure 54.   Mean shadow-based AOD retrievals for moderate AOD urban background cases (Beijing, Taipei, and New York) with gaseous absorption corrections as compared to collocated AERONET AOD measurements.
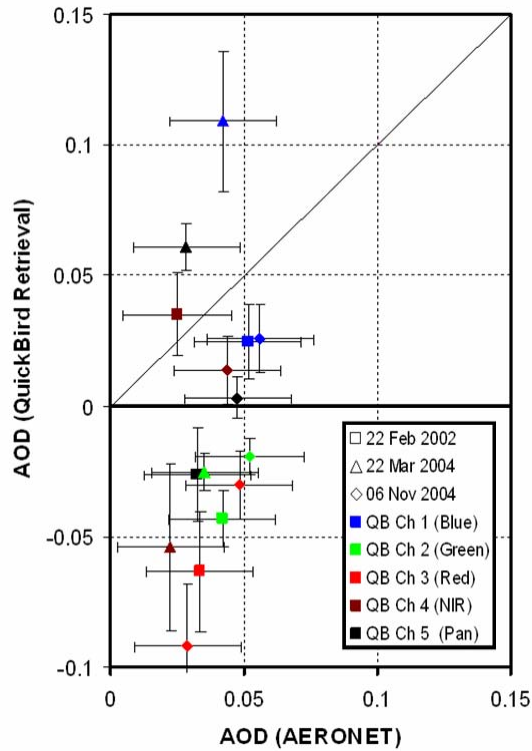
Figure 55.   Mean shadow-based AOD retrievals for low AOD urban background cases
(Buenos Aires) with gaseous absorption corrections as compared to
collocated AERONET AOD measurements.

The gaseous absorption correction had the expected effect in both the low
and moderate AOD cases of shifting the mean retrieved AOD to higher values with the
near-infrared and panchromatic retrievals showing the biggest corrections. At least some
portion of the additional error in surface reflectance beyond the systematic error is
consistent with the effects of gaseous absorption. In the moderate AOD cases, only the
panchromatic retrievals for Beijing and Taipei show good agreement with AERONET
AOD values.   In the low AOD cases, most of the mean AOD values show good
agreement with AERONET values within the bounds of standard error (error bars along
the y-axis), however, almost all retrieval means are of the same magnitude as the
uncertainty in the shadow-based AOD retrieval method (±0.04). Specific sources of error
are impossible to identify at these low AODs, as the errors can be the same magnitude of
or smaller than the uncertainty of the method itself.

119

In the Beijing case, the effects of cloud proximity must be considered as potential sources of error. Retrieved AOD error as a function of mean cloud-free distance along the principle solar plane is shown in Fig. 56. Retrieved AOD error did not decrease as shown by Wen *et al.* (2001), but either showed no change with increased mean cloud-free distance or showed an increase in error with increased distance. Errors seen in the urban cases were not consistent with an increase in scene-wide reflectance and a subsequent increase in QuickBird-derived surface reflectance. No apparent relationship between error in the AOD retrieval and the target's proximity to clouds in the image was found.
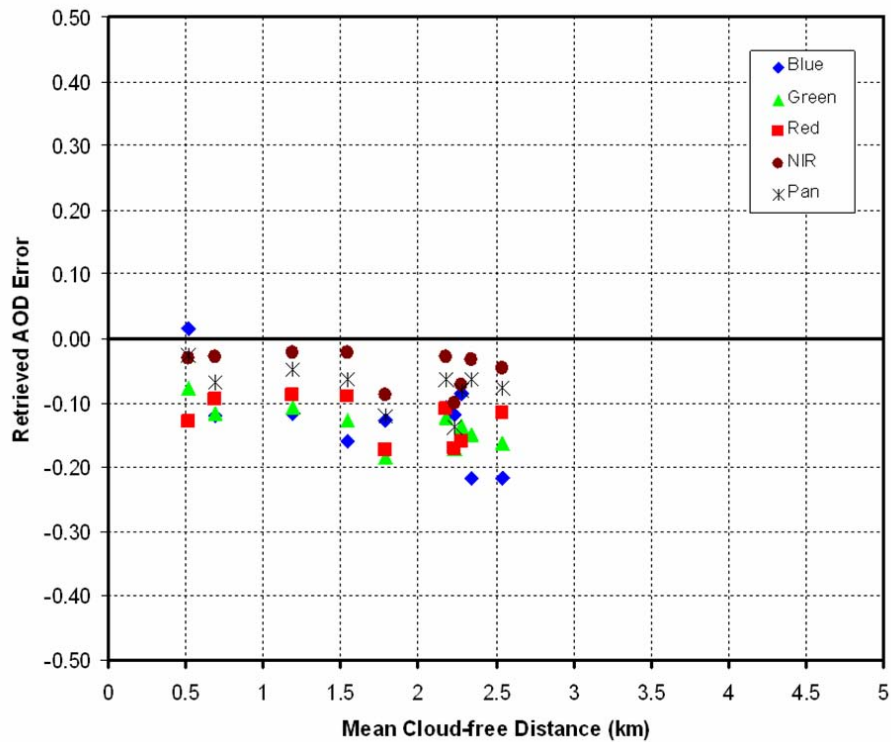
Figure 56.   Retrieved AOD error as a function of mean cloud-free distance along the principle solar plane for the 08 July 2003 Beijing, China case.

The last source of error to be considered is that due to the adjacency effect. Like cloud proximity, adjacency effects work to increase apparent reflectance, offsetting the systematic low bias in surface reflectance or causing a high bias in surface reflectance. While such effects are possible in the near-infrared and panchromatic

channels due to the high reflectance of concrete in the near-infrared region of the spectrum, the errors seen in these cases were not consistent with errors due to the adjacency effect.

E.   SUMMARY OF THE URBAN BACKGROUND INVESTIGATION

The shadow-based AOD retrieval method did not perform well in either the three moderate AOD cases or the three low AOD cases considered. Large discrepancies were seen in comparisons between QuickBird AOD retrievals and AERONET AOD retrievals for all channels and cases. QuickBird-derived surface reflectances correlated well with AERONET-derived surface reflectances for both moderate and low AOD cases with greater low biases in QuickBird-derived surface reflectance seen in the moderate AOD cases. Sources of error were considered. While definitive statements are not possible without controlled experiments, errors were consistent with the systematic low bias to surface reflectance with additional low bias due to the neglect of gaseous absorption. Correction factors for gaseous absorption based on AERONET-measured precipitable water and a mid-latitude summer atmosphere were applied to all channels and cases. Improvements in shadow-based AOD retrievals were seen overall, however, only the panchromatic channel retrievals for the Beijing and Taipei cases showed good agreement with AERONET AOD values after correction. In the low AOD cases, the uncertainty associated with both AERONET AOD values and QuickBird-retrieved AOD values is as large as or larger than the value of the AOD retrievals. For practical applications, any AOD retrieval below 0.15 or 0.1 should be discarded. Target selection criteria suggested in Chapter IV would prove highly restrictive in the urban environment as most surface reflectance and unshaded/shaded radiance difference values fell well below suggested minimums. As in the desert case, additional requirements for a minimum relative azimuth would facilitate access to the shadow as well as prevent contamination of the unshaded/shaded radiance difference through small scale adjacency effects.

THIS PAGE INTENTIONALLY LEFT BLANK

X.   GRASS BACKGROUND INVESTIGATION

A.   OVERVIEW

The third investigation of the new shadow method for AOD retrieval focused on the applicability of the method to AOD retrievals in grass areas typically found in urban and residential areas. Vegetation that is not dark and dense is typically avoided for AOD retrievals; however, the high surface reflectance of grass in the near-infrared region, as seen in Fig. 57, may facilitate AOD retrievals using the shadow method.
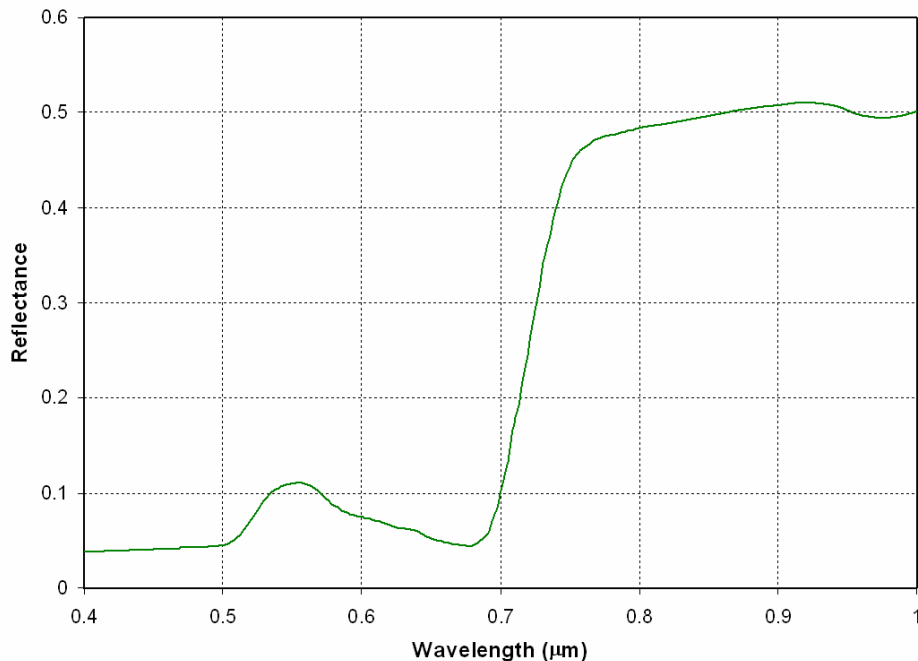
Figure 57.   Spectral reflectance of green grass in the visible and near-infrared region of the solar spectrum (reproduced from the ASTER Spectral Library, courtesy of John Hopkins University).

B.   OBSERVATIONAL DATA

Chapter VII provides thorough descriptions of the QuickBird commercial satellite imagery and AERONET AOD data were used in this investigation. The QuickBird images of Beijing, Taipei, and New York used in the urban background investigation

were again used for this investigation. The AERONET data are also the same data used in the urban investigation and will not be discussed further here. An in-depth discussion of the individual QuickBird images and AERONET data can be found in Chapter IX, Section B. Below is a description of the new locations used for shadow-based AOD retrievals in each image.   Grass surfaces were explicitly avoided in the urban investigation, instead using only man-made surfaces, such as pavement.

1.   Beijing, China, 08 July 2003

The QuickBird satellite image of Beijing, China on 08 July 2003 is the same image used in the urban investigation case. Figure 58(a) is a MODIS overview of eastern China. The ten shadow target sites are identified in the QuickBird image shown in Fig. 58(b) with green circles. Again, shadow-based AOD retrievals are compared to the AOD values obtained from the AERONET site located at the Institute of Atmospheric Physics (39.98N-116.38E).   Exact time and solar/viewing geometries of the Beijing QuickBird image are provided in Table 8 in Chapter IX, Section B.
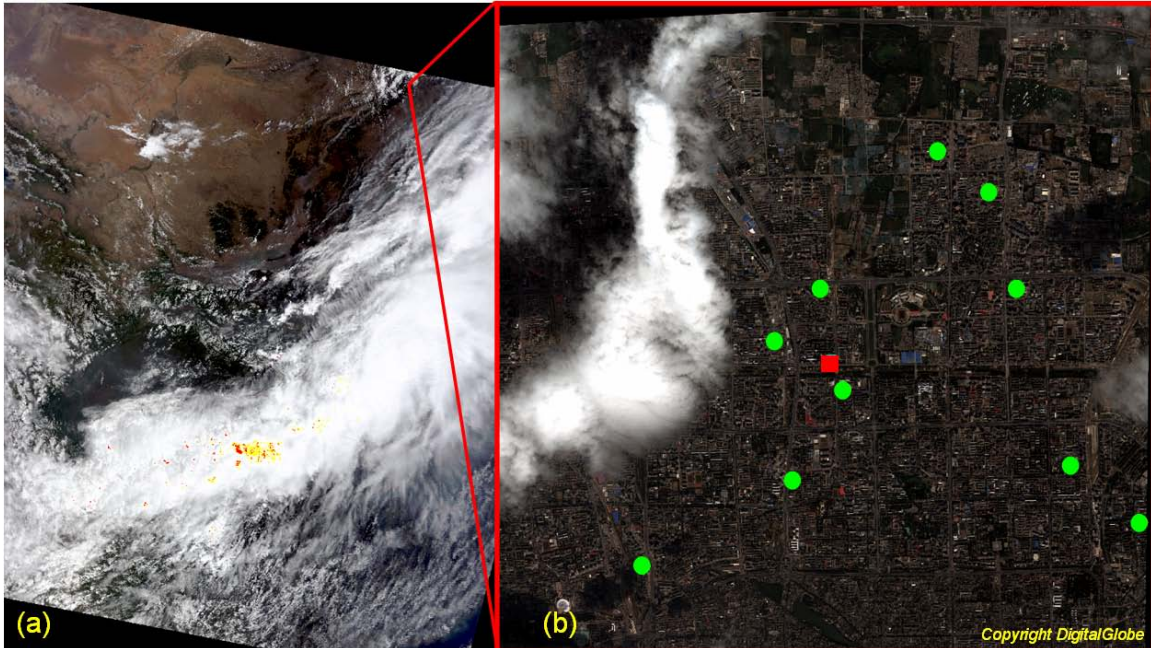
Figure 58.   A MODIS Terra overview (a) of eastern China for 08 July 2003 and (b) the QuickBird RGB image of Beijing for the same day and time with grass background shadow retrieval targets marked with green circles and the AERONET site marked with a red box. Red lines indicate the location of the QuickBird image in the larger MODIS image (QuickBird image courtesy of DigitalGlobe).

2.   Taipei, Taiwan, 07 November 2003

The QuickBird satellite image of Taipei, Taiwan on 07 November 2003 used in the urban investigation is again used in this investigation. Figure 59(a) is the MODIS overview of Taiwan and the East China Sea. Shadow-based AOD retrievals from the ten shadow target sites identified in the QuickBird image shown in Fig. 59(b) (green circles) are again compared to AOD values from the AERONET site located at the Central Weather Bureau Headquarters (25.03N-121.50E). Exact time and solar/viewing geometries of the Taipei QuickBird image are provided in Table 8 in Chapter IX, Section B.
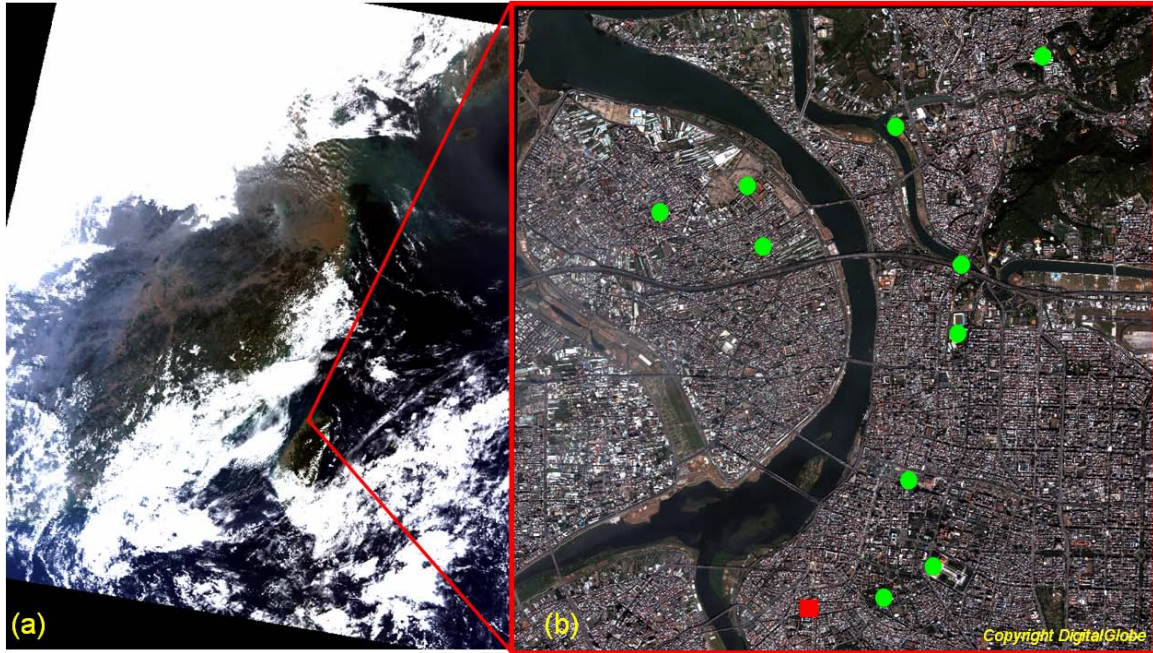
Figure 59.   A MODIS Terra overview (a) of the East China Sea and Taiwan for 07 November 2003 and (b) the QuickBird RGB image of Taipei, Taiwan for the same day and time with grass background shadow retrieval targets marked with green circles and the AERONET site marked with a red box. Red lines indicate the location of the QuickBird image in the larger MODIS image (QuickBird image courtesy of DigitalGlobe).

3.   New York City, New York, 02 August 2002

The QuickBird satellite image of New York City, New York on 02 August 2002 used in the urban investigation was again used in the grass background investigation. Figure 60(a) is a MODIS overview of the northeastern United States. Shadow-based AOD retrievals from the ten shadow target sites identified as green circles in the QuickBird image in Fig. 60(b) are again compared to AOD values from the AERONET site located at the Engineering Building of the City College of New York City (40.82N-73.95W). Exact time and solar/viewing geometries for the New York QuickBird image are provided in Table 8 in Chapter IX, Section B.
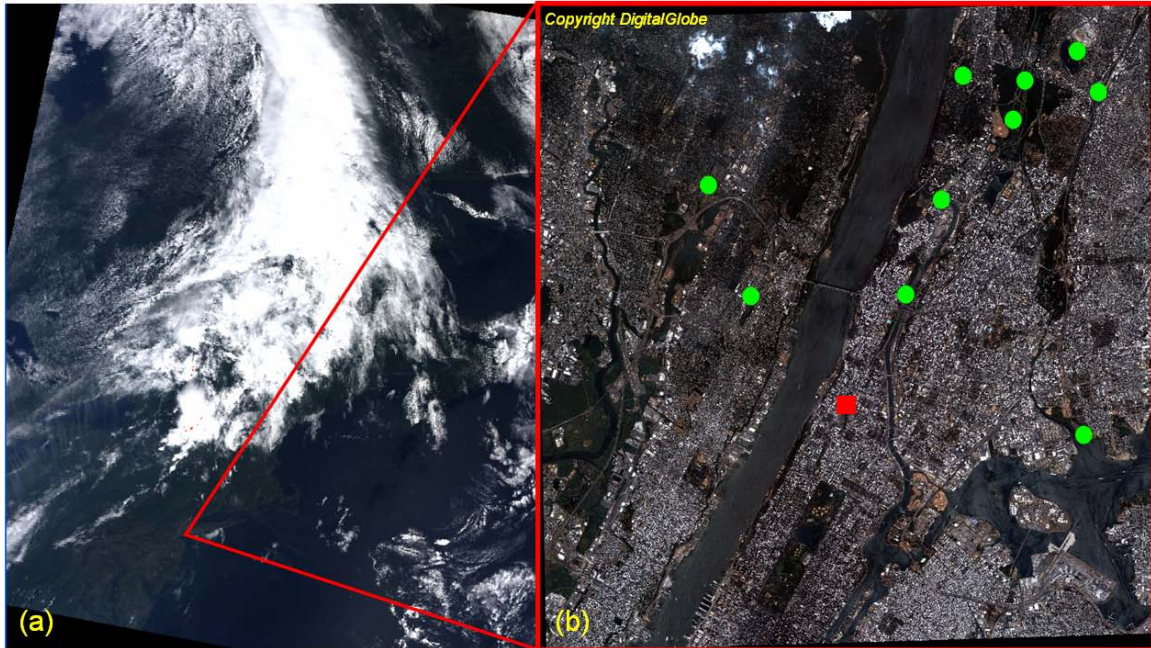
Figure 60.   A MODIS Terra overview (a) of the northeastern United States for 02 August 2002 and (b) the QuickBird RGB image of New York, New York for the same day and time with grass background shadow retrieval targets marked with green circles and the AERONET site marked with a red box. Red lines indicate the location of the QuickBird image in the larger MODIS image (QuickBird image courtesy of DigitalGlobe).

C.   AEROSOL CHARACTERIZATION

The aerosol characterization parameters, single scatter albedo and asymmetry factor used in the urban investigation were retained for the grass background investigation. Again, the shadow method is not extremely sensitive to the accuracy of the parameters used to describe the aerosol particles, asymmetry parameter and single scatter albedo. Mean climatological values for asymmetry parameter and single scatter albedo in urban areas are approximately 0.60 to 0.70 and 0.90 to 0.97. As in the urban investigation, an asymmetry parameter of 0.65 and a single scatter albedo of 0.95 were used as representative values for Taipei and New York. For the Beijing case, the same asymmetry parameter is used, but a more representative single scatter albedo of 0.88 is used bases on Xiang-Ao *et al.* (2005). Again, none of the cases appear to be experiencing heavy loading of any particular aerosol that would violate the assumptions above.

127

D.   RESULTS

1.   Mean QuickBird-retrieved Aerosol Optical Depths

The mean of all shadow-based AOD retrievals for the grass cases, annotated by location and QuickBird channel, are shown in Fig. 61. As in previous chapters, the standard error of the mean is annotated by error bars in y-direction, while the uncertainty of the AERONET data, ±0.02, is shown in the x-direction. It can be readily seen in Fig. 61 that the green and red channels suffer from an extremely low bias on retrieved AOD values, while the blue and near-infrared channels show relatively good agreement with AERONET values. The panchromatic channel again suffers from the chronic low bias seen in previous investigations. Failures of the red and green channels were expected due to extremely low surface reflectance. Success for the near-infrared channel is consistent with enhanced reflectance by vegetation at wavelengths beyond approximately 0.7 µm. It is surprising, however, that the blue channel retrievals performed well. The causes for success in the blue channel are investigated more thoroughly below. As discussed in Chapter IX, caution must be taken with low AOD retrievals as the value of the value of the retrieved AOD may approach the uncertainty in both the AERONET AOD values and the AODs from the shadow-based retrieval method.
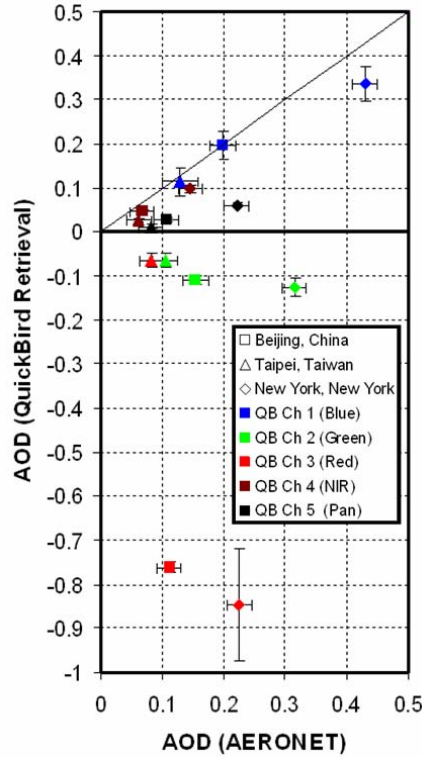
Figure 61.   Mean shadow-based AOD retrievals with associated standard error over grass backgrounds for Beijing, China, Taipei, Taiwan, and New York, New York as compared to collocated AERONET AOD measurements.

2.   Surface Reflectance Retrievals

As in the previous chapters, QuickBird-derived surface reflectances were compared to the surface reflectance determined from the AERONET AOD values, holding all other parameters constant for each site. Again, mean aerosol reflectance for all surface reflectance retrievals was calculated based on the AERONET AOD.

High surface reflectance of vegetation, especially grass, in the near-infrared region of the spectrum and its suitability to the shadow-based AOD retrieval method was the impetus for this investigation. The QuickBird-derived surface reflectances shown in Fig. 62 ranged from 0 to 0.47, however, the blue, green, and red channels show surface reflectances no greater than approximately 0.07 and the panchromatic channel surface reflectances are no greater than 0.15, the suggested minimum surface reflectance for the shadow-based AOD retrieval method. The surface reflectances for the near-infrared channel show values ranging from 0.17 to 0.47 and well exceed the minimum

requirements for the shadow-based retrieval method. Correlation between the QuickBird-derived surface reflectance and the surface reflectance required by the AERONET-measured AOD is high and the QuickBird-derived surface reflectances again show a consistent low bias of approximately 0.02 to 0.05.
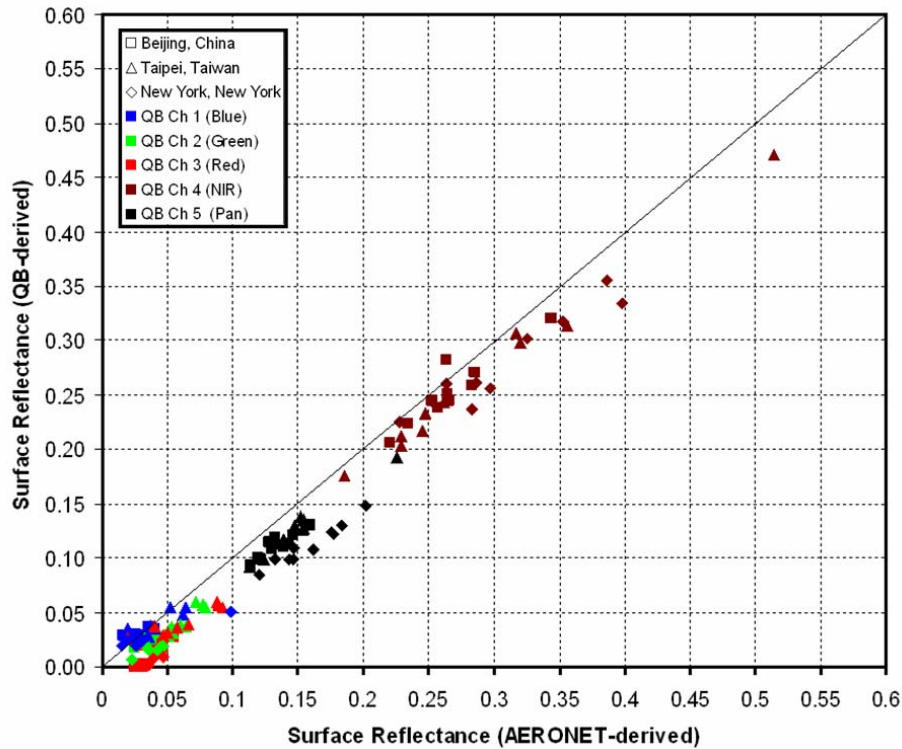
Figure 62. Comparison of QuickBird-derived surface reflectances as determined from measured unshaded radiance to surface reflectance required to obtain the AERONET-derived AOD for the grass background cases (Beijing, Taipei, and New York).

3. Sources of Error

As in the previous investigations, the errors can only be found to be consistent or not consistent with various sources of error without further testing in a more controlled environment. Also, factors that are well described and taken as constant and ignored as sources of error in favor of focusing on surface reflectance and mean aerosol reflectance.

130

a.   *Unshaded/Shaded Radiance Difference*

The unshaded/shaded radiance difference must be considered as one possible source of error. As the primary measured signal on which the shadow-based AOD retrieval method is based, the error in the retrieved AOD is expected to decrease as the difference increases. Two clear groups can be seen in Fig. 63 that shows retrieved AOD error as a function of unshaded/shaded radiance difference. For the blue, green and red channels with unshaded radiance differences of 20 W m^{-2} sr^{-1} nm^{-1} or less, the retrieved AOD error is highly variable and shows no clear relationship with the radiance difference. In the second group, the near-infrared and panchromatic channels show radiance differences ranging from 30 to 105 W m^{-2} sr^{-1} nm^{-1} while retrieved AOD error is approximately 0.05 for the near-infrared and 0.1 for the panchromatic and largely invariant. In both cases, the retrieved AOD error shows no clear relationship with unshaded/shaded radiance difference.   The minimum unshaded/shaded radiance difference of 10 W m^{-2} sr^{-1} nm^{-1} suggested in Chapter IV would do little to improved individual or mean AOD retrievals and would preclude the used of the AOD retrievals from the blue channel which agreed well with AERONET AOD values.
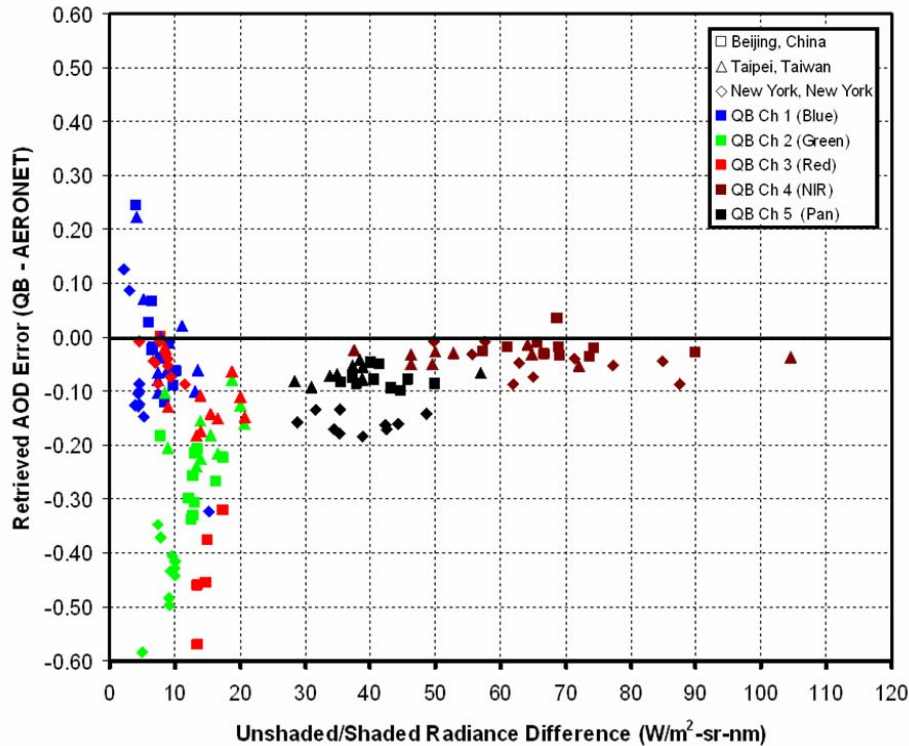
Figure 63.   Shadow-based AOD retrieval error as a function of unshaded/shaded radiance difference for all grass background cases (Beijing, Taipei, and New York).

As discussed in the previous chapters, the unshaded/shaded radiance difference is largely preserved in the presence of fluctuations in the diffuse radiance field, as both the unshaded and shaded regions are affected equally and the difference remains unchanged. Again, small scale adjacency effects can cause an unwarranted decrease in the unshaded/shaded radiance difference. This is a very real possibility if near-infrared channel retrievals are attempted when trees, also highly reflective in the near-infrared, are the shadow-generating object. As above, this phenomenon is highly dependent on the solar/sensor geometry and should be obvious upon visual inspection.

Error due to sub-pixel illumination or shading as discussed in the previous chapters also remains a potential source of error. Again, data collection strategies, such as using mode radiance values vice mean radiance values, can prevent biases from sub-pixel effects at the shadow boundary. Proximity of other structures, especially tall or highly reflective ones, in the vicinity of the shadow must be considered and can often be avoided using of minimum target shadow stand-off distances.

132

b. Surface Reflectance/Mean Aerosol Reflectance

The method used in the shadow-based AOD retrieval to determine surface reflectance is subject to all fluctuations in the diffuse radiance field and therefore presents the largest potential source of error in the shadow-based AOD retrieval. As with retrieved AOD error as a function of unshaded/shaded radiance difference, retrieved AOD error shows no clear variation with surface reflectance as seen in Fig. 64. Both the near-infrared and panchromatic channels show lower overall error in retrieved AOD, as expected from the comparison between QuickBird-derived mean AOD retrievals and AERONET AOD values. Again, error in retrieved AOD as a function of error in surface reflectance may provide more clues to potential sources of error.
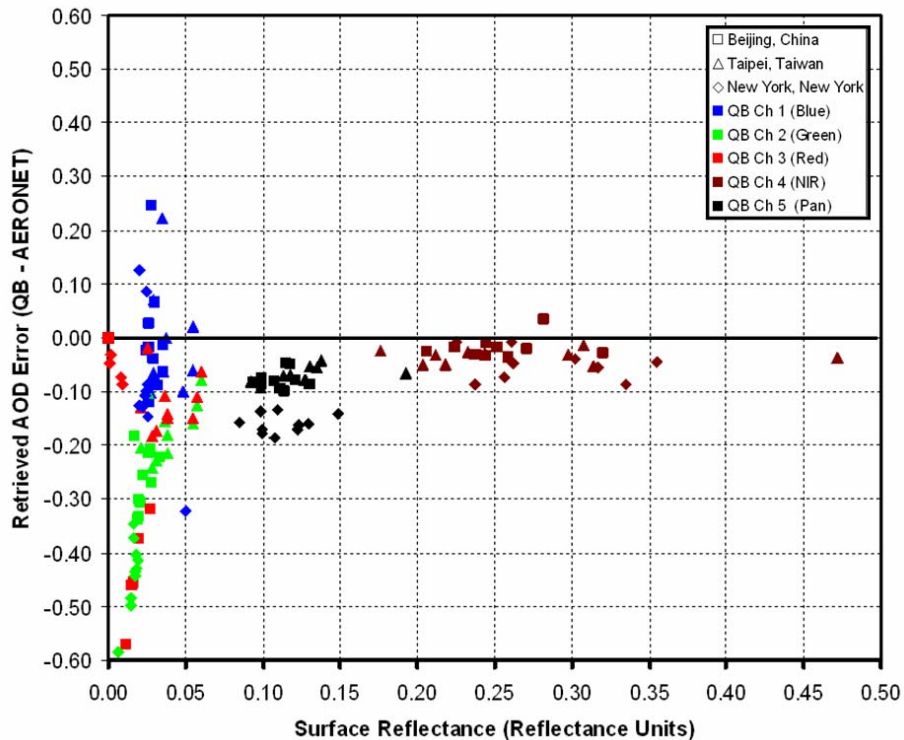
Figure 64.   Shadow-based AOD retrieval error as a function of surface reflectance for all grass background cases (Beijing, Taipei, and New York).

The first source of error in surface reflectance that must be addressed is the systematic low bias due to the overestimation of mean aerosol reflectance based on the initial overestimation of total optical depth. Mean aerosol reflectance values tend toward a high bias of 0.01 to 0.03 resulting in a corresponding low bias to surface reflectance values as seen in Fig. 62. The sensitivity of the final shadow-based AOD retrieval to surface reflectance is a 0.04 increase for every 0.01 increase in surface reflectance with an offset due to mean aerosol reflectance of -0.002 for every 0.01 increase in mean aerosol reflectance. Error in surface reflectance was compared to the error in AOD of 0.038 (dashed line in Fig. 65) to determine errors are consistent with errors in AOD due only to the overestimation of mean aerosol reflectance and underestimation of surface reflectance. All three grass background cases were combined in Fig. 65 and retrieved AOD error was compared to error in surface reflectance.
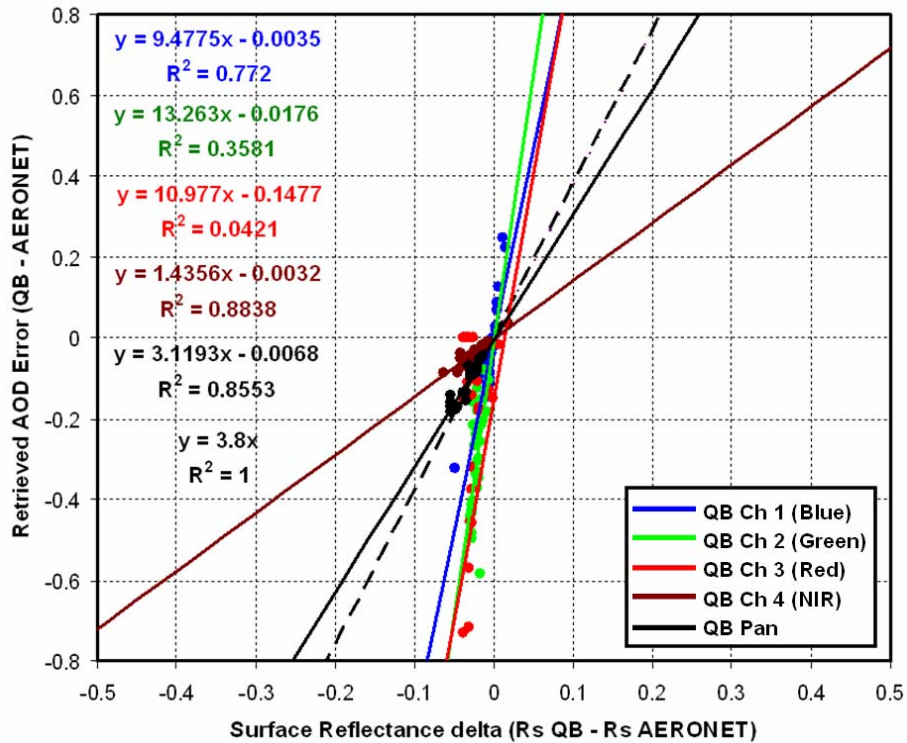
Figure 65.   Retrieved AOD error as a function of surface reflectance error for all grass background cases combined for each QuickBird channel. The dashed line denotes the theoretical error due to overestimation of mean aerosol reflectance and underestimation of surface reflectance combined.

The relationships seen in Fig. 65 between the error in surface reflectance and the retrieved AOD error are generally consistent with the sensitivity analyses presented in Chapter IV, but cannot be solely attributed to the systematic underestimation of surface reflectance. Both the near-infrared and panchromatic channels show that other factors are working to increase apparent surface reflectance and decrease the retrieved AOD error. In the blue, green, and red channels, the relationship between the errors is consistent with additional factors causing further underestimation of surface reflectance, however no clear relationship with wavelength is apparent. While some portion of the retrieved AOD error maybe consistent with the systematic bias of surface reflectance in the procedure, other sources of error in surface reflectance must be investigated.

For the blue, green, and red channels, the underestimation of surface reflectance points to an underestimation of measured unshaded radiance. Holekamp's (2003) post-launch calibration errors leading to underestimation of QuickBird radiance

135

values could account for such a low bias to surface reflectance, however, underestimates of 8.6%, 7.8%, 4.9% and 0.4% for the blue, green, red and near-infrared channels respectively, would imply that errors would decrease as wavelength increases. The error relationships show no such correlation with wavelength and are not consistent with sensor calibration errors.

Gaseous absorption does work to reduce transmittance and decrease the satellite-observed radiance, decreasing the TOA and surface reflectance and unshaded/shaded radiance difference. Corrections for gaseous absorption showed promise for the panchromatic channels in the desert cases and showed marginal improvement for the urban cases. The effect of applying the same gaseous absorption correction factors to the unshaded radiance used in the urban investigation can be seen in Fig. 66.
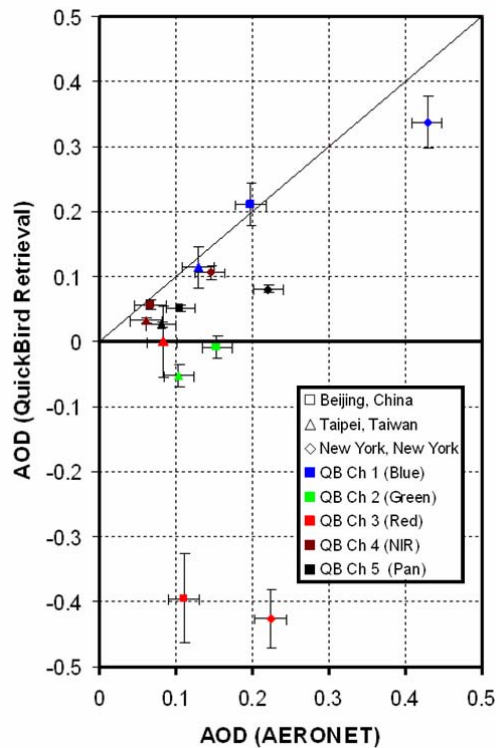
Figure 66.   Mean shadow-based AOD retrievals for all grass background cases (Beijing, Taipei, and New York) with gaseous absorption corrections as compared to collocated AERONET AOD measurements.

The gaseous absorption correction had the expected effect of shifting the mean retrieved AOD to higher values. The largest adjustments were expected in the panchromatic and near-infrared channels due to the large impact water vapor in the near-infrared region of the solar spectrum. The near-infrared channel showed the most improvement, with adjusted mean AOD retrievals agreeing well with AERONET AOD values. The panchromatic retrievals showed an improvement, but were still low as compared to the AERONET AOD values. The green and red channels showed only marginal improvement. Due to the low reflectance of grass in the green and red regions of the solar spectrum, these channels are not suited to the shadow-based AOD retrieval method over grass. The blue channel mean AOD retrievals, being least sensitive to gaseous absorption, showed little change from the mean retrieval values prior to correction.

The success of the blue channel retrievals has yet to be explained through the preceding error analysis. Additionally, AOD retrievals from the blue channel in the urban cases did not show the same success under similar conditions. Suffering from both low unshaded/shaded radiance differences and low surface reflectance over grass backgrounds, the blue channel AOD retrievals still produce realistic values with good agreement with AERONET AOD values while the green channels retrievals with comparable values (and even a higher reflectance) have a significant low bias in all cases. The difference between the blue and green channels responsible for this success is the spectral solar irradiance values used for each band. The Wehrli (1985) spectral solar irradiance curve, gaseous species transmittance curves for a notional mid-latitude summer atmosphere, the spectral reflectance of grass, and the spectral response for each channel are shown in Fig. 67. A spectral solar irradiance of 1973 W m^{-2} nm^{-1} is used for the blue channel, while a value of 1854 W m^{-2} nm^{-1} is used for the green channel. This difference of approximately 120 W m^{-2} nm^{-1}, in the argument of the natural log in the governing equation, Eq. (34), in conjunction with low surface reflectance and radiance difference values, is sufficient to return AOD values four times larger in the blue channel than in the green channel. In cases of higher surface reflectances of approximately 0.2 or greater, the difference in the AOD values returned for the blue and green channels under

equivalent conditions is less than 10%. In the urban case, structures surrounding the shadowed area blocked a significant portion of the diffuse irradiance field causing an increase in the unshaded/shaded radiance difference and a decrease in the final AOD retrieval. The shadow targets over the grass background were largely in open park areas were the nearest structures were at least one-half kilometer away. For this reason, QuickBird-derived AOD values from the blue channel remain a viable option over grass backgrounds in open areas.
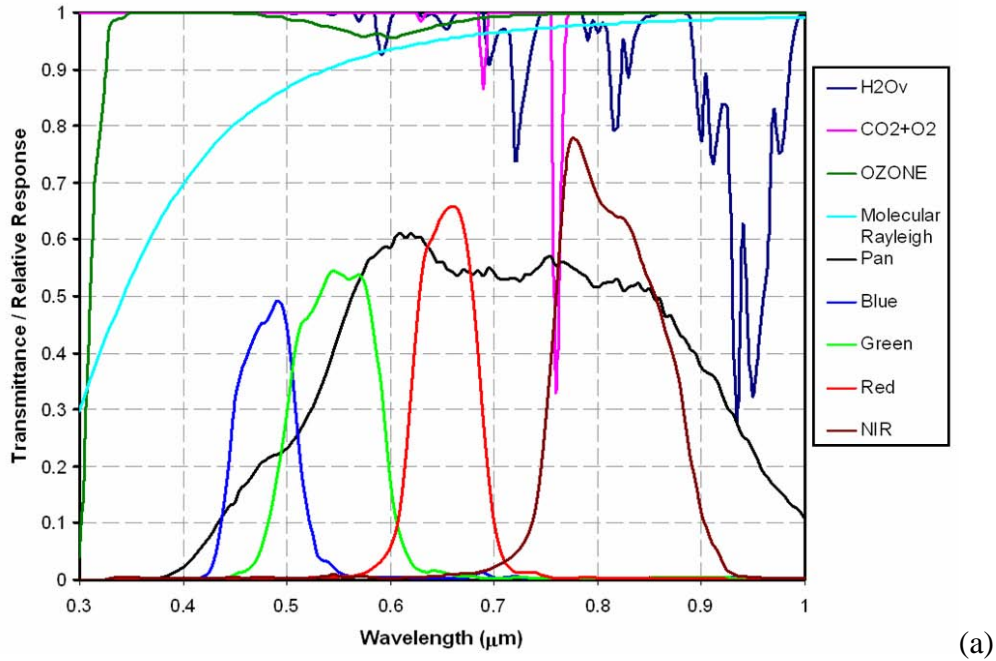
(a)
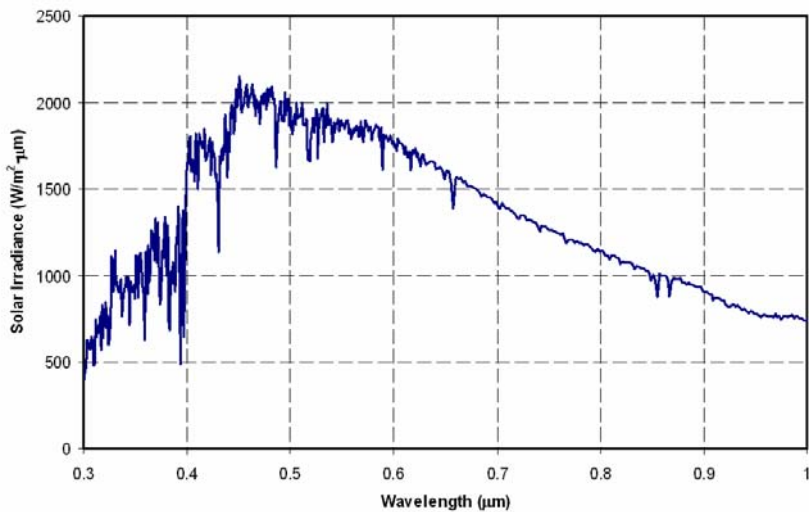
(b)

Figure 67.   Spectral distributions of (a) QuickBird channel relative response, gaseous
species transmittance based on a mid-latitude summer atmosphere, and
reflectance for green gas, as well as (b) spectral solar irradiance based on
Wehrli (1985).

As in the urban investigation, the Beijing case was evaluated for the effects of
cloud proximity on retrieved AOD error. Retrieved AOD error as a function of mean
cloud-free distance along the principle solar plane is shown in Fig. 68. Retrieved AOD
error did not decrease as shown by Wen *et al.* (2001), but instead showed no change with

increased mean cloud-free distance as in the urban background cases. Errors seen in the both the urban background and grass background cases were not consistent with an increase in scene-wide reflectance and a subsequent increase in QuickBird-derived surface reflectance. Wen *et al.* (2001) showed that cloud fractions of 0.2 or less had minimal impact on the apparent reflectance of the scene. Additionally, no apparent relationship between error in the AOD retrieval and the target's proximity to clouds in the image has been found.
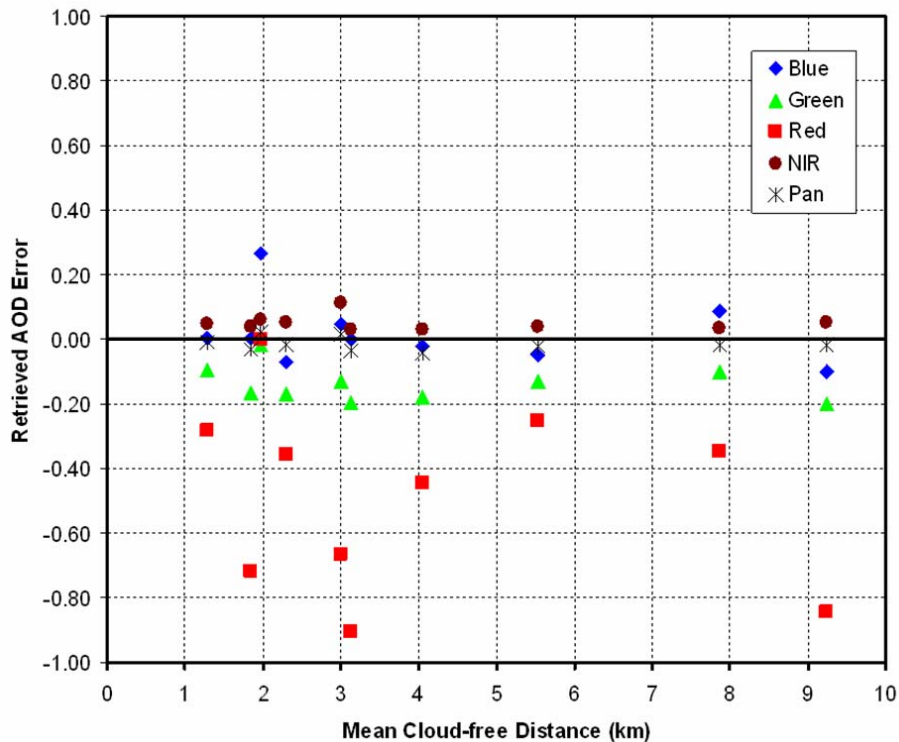
Figure 68.   Retrieved AOD error as a function of mean cloud-free distance along the principle solar plane for the 08 July 2003 Beijing, China grass background case.

The adjacency effect is the last source of error to be considered. Like cloud proximity, adjacency effects work to increase apparent reflectance, offsetting the systematic low bias in surface reflectance or causing a high bias in surface reflectance. Such effects were seen for the near-infrared and panchromatic channels in Fig. 65. While adjacency effects cannot be conclusively shown to cause the error offset from the systematic low bias in surface reflectance, such offsetting errors are consistent with

adjacency effects in the near-infrared region due to large areas of highly reflective grass and trees that would affect both the near-infrared and panchromatic channels.

E.   SUMMARY OF THE GRASS BACKGROUND INVESTIGATION

The shadow-based AOD retrieval method performed well for the blue and near-infrared channels over grass backgrounds. Large discrepancies were seen in comparisons between QuickBird AOD retrievals and AERONET AOD retrievals for the red and green channels in all cases. The panchromatic channel again showed the same low bias seen in previous investigations. QuickBird-derived surface reflectances correlated well with AERONET-derived surface reflectances with QuickBird-derived surface reflectance showing a low bias. Sources of error were considered. As in the urban case, errors were consistent with the systematic low bias to surface reflectance with additional low bias due to the neglect of gaseous absorption. Correction factors for gaseous absorption based on a notional mid-latitude summer atmosphere were applied to all channels and cases. Improvements in shadow-based AOD retrievals were seen overall, however, overcorrection in the near-infrared channel for all cases resulted in a high bias in the mean retrieved AOD. After corrections for gaseous absorption, the blue, near-infrared, and panchromatic channels provided realistic mean AOD retrievals and compared well with AERONET AOD values. Due to exceptionally low reflectance of grass in the green and red regions of the solar spectrum, the green and red channels are not suitable for shadow-based AOD retrievals over grass backgrounds. While the blue channel also experiences the same low surface reflectance values over grass backgrounds, the spectral solar irradiance in the blue channel is sufficiently greater than that in the green or red channel and provides sufficient signal for reasonable shadow-based AOD retrievals. Again, target selection criteria suggested in Chapter IV would prove highly restrictive for grass backgrounds as most surface reflectance and unshaded/shaded radiance difference values fell well below suggested minimums. Such target criteria would completely preclude the use of the blue channel if strictly applied. As in the desert case, additional requirements for a minimum relative azimuth would not only facilitate access to the shadow, but also prevent contamination of the unshaded/shaded radiance difference through small scale adjacency effects from nearby vegetation.

THIS PAGE INTENTIONALLY LEFT BLANK

XI. ADVANTAGES, LIMITATIONS, AND PROSPECTS FOR THE SHADOW-BASED AOD RETRIEVAL METHOD

A. STRENGTHS AND LIMITATIONS OF THE SHADOW-BASED AOD RETRIEVAL METHOD

The shadow-based AOD retrieval method has been shown to perform well for desert surfaces with reflectance values greater than 0.15. In these cases, area-averaged aerosol optical depths for each QuickBird channel compared well with AERONET measurements and the blue, green and red channels showed good spectral consistency with each other. The aerosol is described using only the asymmetry parameter in the Henyey-Greenstein phase function and a single scatter albedo. Comparison of the mean aerosol reflectance based on the Henyey-Greenstein phase function with the mean aerosol reflectance based on actual dust phase functions shows only minor differences. Without the need for look up tables and modeled aerosol parameters, the method is computationally fast and requires little modification to relocate to new areas.

The shadow-based AOD retrieval method has several physical limitations. First, a shadow must be observable before any measurements can be taken and the unshaded/shaded radiance difference must be at least 10 W m^{-2} sr^{-1} nm^{-1}. Second, a minimum surface reflectance of 0.15 is required for reliable AOD retrievals. These limits lead to a practical minimum of retrieved AOD of 0.1. The upper limit of the method is determined by maximizing the cosine of the solar and sensor zenith angles, maximizing surface reflectance, and minimizing mean aerosol reflectance. Based on such parameters, the upper limit of the shadow-based AOD retrieval method is approximately 2.0. At this AOD, the surface is effectively obscured and shadows are not distinguishable.

While the shadow-based AOD retrieval method was compromised in the urban background investigation and only two channels, blue and near-infrared, performed well in the grass background investigation, there is potential for improvement. Reliable AOD retrievals are possible in urban areas with careful target selection. For grass backgrounds, reliable AOD retrievals from two channels can provide a significant amount of information about aerosol size distribution and type.

B.   TARGET SELECTION CRITERIA

Based on the results of the investigations detailed in Chapters VIII, IX, and X, several target selection criteria are suggested. As stated above, a surface reflectance of 0.15 is necessary. Beyond this, large shadows are better as long as they fall across a homogeneous surface. The shadow should be a minimum of four pixels wide and four pixels deep. This allows the user to determine a minimum observed radiance value that is not contaminated by pixels crossing the shadow edge. Target shadows should be at least one to two kilometers away from other structures, especially those with highly reflective surfaces. This is especially important in urban areas where the high density of buildings and reflective nature of some buildings can compromise the AOD retrieval. Finally, shadowing structures that are highly reflective should also be avoided due to potential small-scale adjacency effects for some solar/sensor geometries. Two possible targeting strategies are presented below.

C.   PROSPECTIVE   STRATEGIES   FOR   AUTOMATION   AND   OPERATIONAL IMPLEMENTATION

Manual visual inspection of high-resolution commercial satellite imagery for shadow targets can be tedious and time consuming, often taking a much as eight hours per image to identify shadows and collect the appropriate radiance measurements. If the shadow-based AOD method is to be used in an operational environment, many of the functions, especially target identification and data acquisition and evaluation, must be automated.   Such automation schemes are likely to fall into two main categories: dynamic targeting and fixed targeting.

1.   Dynamic Targeting Strategy

The investigations detailed in this work indicate that the shadow-based AOD retrieval method favors high surface reflectance, especially over broad regions. Shadows in such areas are easily identified by their significantly lower radiance values and the target typically meets the minimum criteria for both surface reflectance and

unshaded/shaded radiance difference. Automating the collection of these shadows of opportunity can provide a large number of individual AOD retrievals on which to base the mean AOD for the image. Using a systems engineering approach, expertise from multiple disciplines can be leveraged to provide an end-to-end strategy to effectively collect targets, evaluate their suitability, retrieve individual AOD values, determine a mean AOD, and convert AOD values to parameters such as visibility for operational use. The panchromatic channel experienced errors consistent with the effects of gaseous absorption, especially water vapor. The QuickBird satellite is not capable of evaluating atmospheric water vapor independently, nor are any of the current commercial high-resolution satellites. Current commercial satellites are also incapable of determining a boundary layer height to which the measured aerosol is confined. Because of this, operational meteorological satellites will be necessary to provide information to the AOD retrieval process. A notional scheme for a dynamic targeting scheme is shown in Fig. 69.
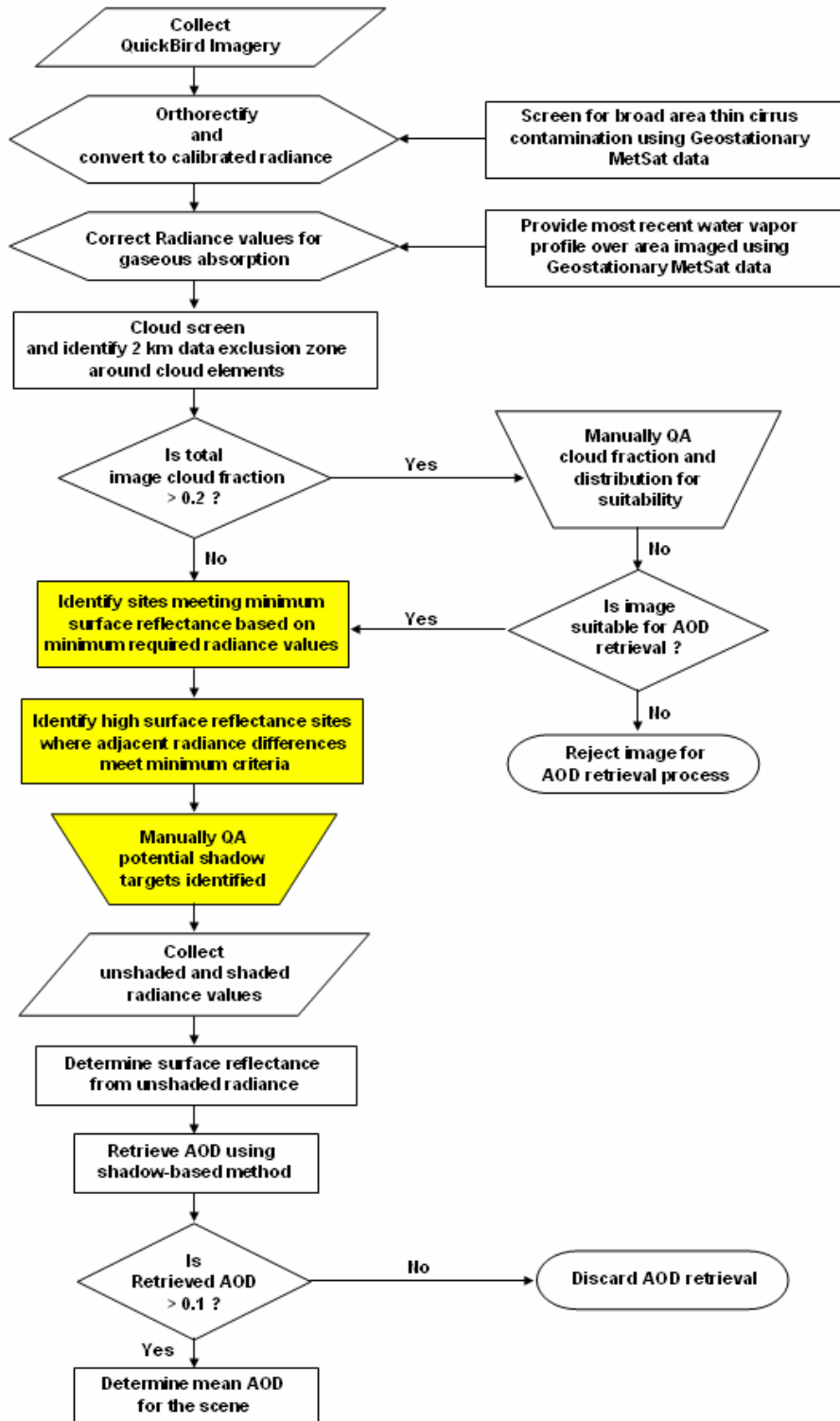
Figure 69.   Notional flowchart for a dynamic targeting scheme applied to the shadow-based AOD retrieval method. Yellow boxes denote steps unique to dynamic targeting scheme.

2.   Fixed Targeting Strategy

Investigations in the urban environment showed a great sensitivity to target selection. Many of the target shadows used in the study failed to meet the minimum target criteria. For this reason, the fixed targeting strategy is proposed. While many target shadows failed to meet minimum criteria, a few targets did meet the minimum criteria and provided individual retrievals in good agreement with AERONET AOD values. If fixed shadowing structures, known to meet minimum target criteria, are identified, these targets can be specifically targeted for repeated AOD retrievals. This strategy, while not quickly relocatable, does cut out the processing burden of target identification and evaluation speeding up the overall retrieval process. As in the dynamic targeting strategy, additional information from operational meteorological satellites such as column water vapor and boundary layer height will be necessary. A notional scheme for a fixed targeting scheme is shown in Fig. 70.
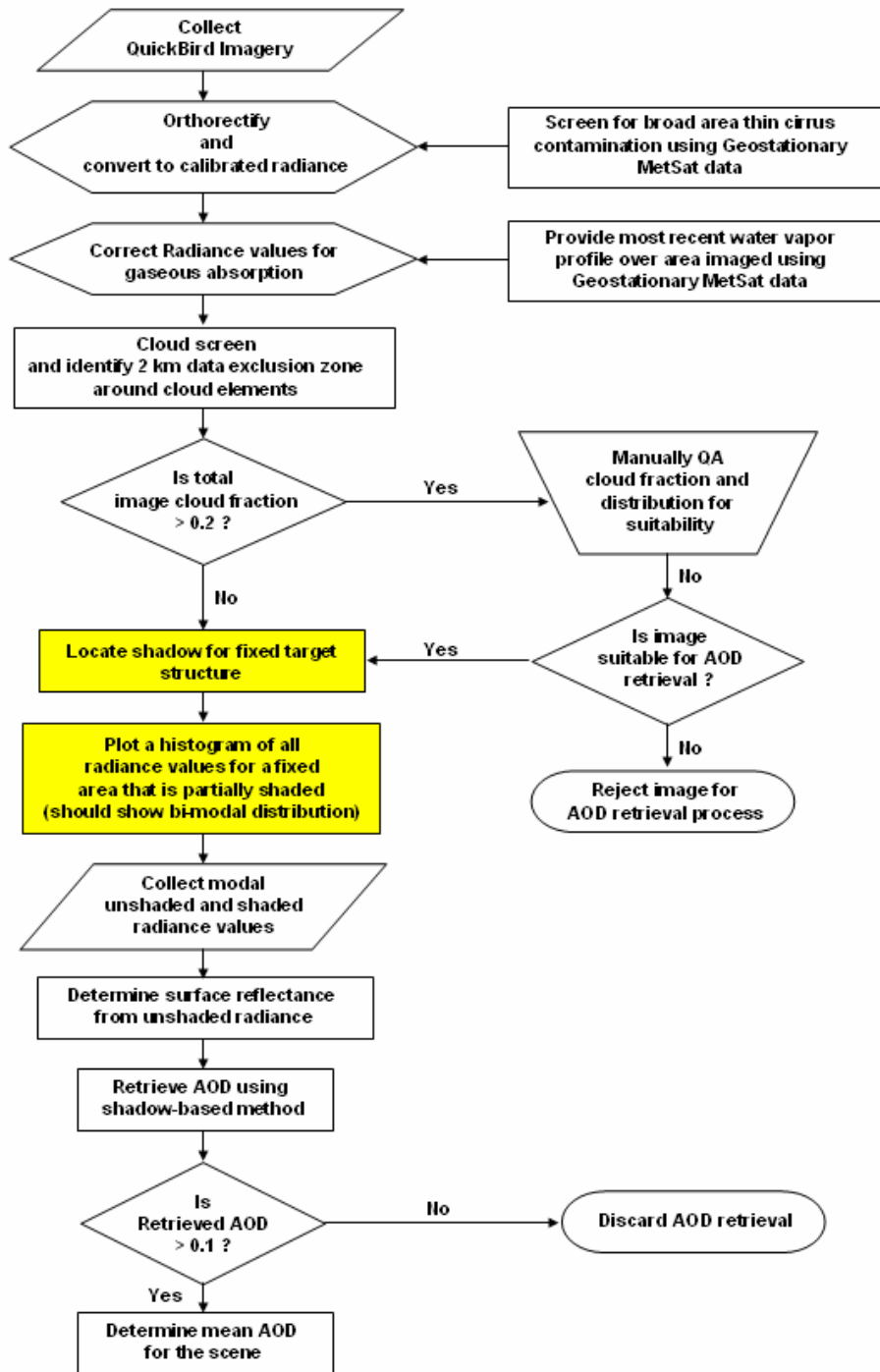
Figure 70.   Notional flowchart for a fixed targeting scheme applied to the shadow-based
              AOD retrieval method. Yellow boxes denote steps unique to dynamic
              targeting scheme.

XII. CONCLUSIONS AND RECOMMENDATIONS

A.   CONCLUSIONS

A new method of satellite-based aerosol optical depth (AOD) retrieval is proposed and investigated.   The proposed method relates the observed radiance difference across shadow boundaries to total optical depth.   The shadowed and unshadowed areas observed must fall across a surface of constant reflectance and, according to sensitivity studies, must have a surface reflectance of at least 0.15 for realistic and consistent results. Current overland satellite AOD retrieval methods are severely limited over areas of high surface reflectance or require a training data set to make empirical adjustments to retrieve AOD. The proposed method requires no training data set and works best for the environment where current overland AOD retrieval methods generally fail.

QuickBird commercial, high-resolution satellite imagery was chosen to test the new AOD retrieval method. Sensitivity and uncertainty analyses were conducted based on the uncertainties inherent in QuickBird measurements. The AOD uncertainty due to each retrieval component is well below the sensitivity of the final AOD retrieval to that component. Therefore, the changes seen in AOD at moderate AODs can be attributed to changes in the components of the governing equation and not to the uncertainty inherent in the method.

The shadow-based AOD retrieval method was tested using QuickBird imagery over desert, urban, and grass backgrounds due to high surface reflectance in some, if not all, channels. Multiple AOD retrievals were made across each scene and averaged to find an overall AOD for the scene. These mean AOD values were compared to temporally and spatially co-located AERONET AOD measurements.

Mean AOD values were found to compare well in the desert background cases for the multi-spectral channels, while the panchromatic channel showed a consistent low bias. Sources of error were investigated. While conclusive statements cannot be made about the sources of error without further testing in a controlled environment, the errors

149

observed were consistent to a systematic low bias in retrieved AOD inherent in the shadow-based AOD methodology offset by adjacency effects due to high surface reflectances across the scene. Corrections for gaseous absorption were examined for all channels and were found to improve the final result. AOD retrievals for the multispectral channels showed a high bias consistent with adjacency effects.

Mean AOD values in the urban cases showed a large, consistent low bias and, in many cases, returned negative mean AOD values. Errors were found to be consistent with the systematic low bias of the shadow-based AOD methodology with additional low bias consistent with the neglect of gaseous absorption and loss of diffuse sky irradiance due to surrounding buildings. Corrections for gaseous absorption resulted in some improvement in the final result, however, most shadow targets failed to meet minimum unshaded/shaded radiance difference and surface reflectance criteria.

Finally, the mean AODs retrieved over grass backgrounds compared well with AERONET AOD values for the blue and near-infrared channels, but showed a large, consistent low bias for the other channels. Errors in the near-infrared and panchromatic channels were consistent with the systematic low bias of the shadow-based retrieval method with offsetting errors due to the adjacency effect. Errors at least partially consistent with the neglect of gaseous absorption were found in the green, red, near-infrared and panchromatic channels. Corrections for gaseous absorption resulted in improvements in the panchromatic retrievals, but the red and green channels suffered from surface reflectances well below the suggested minimum reflectance criteria of 0.15. The grass background provided high surface reflectances in the near-infrared region, allowing consistent retrievals using the near-infrared and panchromatic channels. In the blue region, however, the incoming spectral solar irradiance is sufficiently larger than that in the green and red regions to allow the retrieval of realistic AODs even when both surface reflectance and unshaded/shaded radiance difference are well below suggested minimums.

A limited number of images were available for each investigation. Within each image, retrieval sites were selected as representative of the different structures found in the scene and redundancy was avoided where possible. The results presented here show

150

general biases in the proposed method with respect to different backgrounds but do not have the statistical rigor of a full validation study.

B.   RECOMMENDATIONS

Recommendations from this study fall in to two distinct categories; 1) examining the elements of the governing equations and their determination for possible improvements and 2) the outline of controlled experiments allowing the identification of specific sources of error.

1.   Examination of the Elements of the Governing Equation

The parameters of the governing equation are discussed thoroughly in Chapter III. Many of these parameters are approximations of the actual environment or are based on such approximations. The calculation of mean aerosol reflectance is based on the numerical approximation to the actual quadruple integral defining mean aerosol reflectance. In this same calculation, a one-sided Henyey-Greenstein phase function is used to approximate the aerosol phase function. Investigation into the use of the two-sided Henyey-Greenstein phase function approximation or aerosol-specific phase functions may provide improvements in determining mean aerosol reflectance.

Currently, spectral solar irradiance values are determined for each QuickBird channel based on the Wehrli (1985) annually averaged spectral solar irradiance curves. While seasonal changes in solar irradiance are small, the impact of such changes on the shadow-based AOD retrieval method should be evaluated.

Finally, the determination of surface reflectance from the partitioning of apparent reflectance at the top of the atmosphere based on QuickBird measurements of the unshaded surface should be compared to measured surface reflectance values. Do measured surface reflectance values conform to the Lambertian assumption? If measured surface reflectance values are used in lieu of satellite derived surface reflectances, is partitioning of the top of the atmosphere reflectance improved? Much of the work suggested here would not require extensive field tests under controlled conditions, but could provide much insight into focus areas for improvements.

2. Experiments Designed to Isolate Sources of Error

Experiments in a controlled environment are required to isolate specific sources of AOD retrieval error. Radiometric characterization of commercial high-resolution satellites, such as done by Pagnutti *et al.* (2003) and Holekamp (2003), rely on vicarious calibration sites where multiple coincident satellite measurements of a calibrated target can be made and compared. The calibrated targets are generally large, square, white tarps, generally on the order of 50 meters or larger on each side, with reflectances approaching 0.99. Such tarps would be placed across a shadow boundary and imaged, providing detailed knowledge of the surface characteristics. Coincident atmospheric soundings would be needed to provide detailed knowledge of the atmospheric effects. Multiple geographic locations may be necessary to vary the amount of water vapor and potential aerosol types. Multiple calibrated tarps may be positioned in close proximity to the partially shaded tarps to study adjacency effects. While this is far from a comprehensive outline, it shows the potential for controlled studies using existing vicarious calibration sites and techniques.

APPENDIX A. METEOROLOGICAL OVERVIEW FOR UNITED ARAB EMIRATES

The Southern Arabian Gulf is a complicated region that forms a "meteorological crossroads" of sorts coming under the influence at various times of atmospheric interactions with the Tibetan Plateau, the Indian sub-continent, and Saharan Africa. The overall synoptic pattern of South West Asia and the Arabian Gulf region is dominated by a monsoon regime in which a Northeasterly monsoon sets up in the winter and a Southwesterly monsoon in the summer with transition periods in between. Below is a brief description of these monsoons as outlined in the Science Plan for the UAE[2] campaign (Reid *et al.* 2004) and described in depth by the Forecaster's Handbook (NCMOF Bahrain 1999), with emphasis on the Southwesterly monsoon that dominated during the UAE[2] campaign.

1.   Northeasterly Monsoon (Winter)

As outlined in the Science Plan for the UAE[2] campaign (Reid *et al.* 2004) and described in depth by the Forecaster's Handbook (NCMOF Bahrain 1999), the Northeasterly, or winter, monsoon is found in South West Asia during December, January, February and March and is driven by the cooling of the Tibetan Plateau while the sea surface temperatures are largely constant. This forms a pressure gradient in the lower levels that results in northeasterly offshore winds leaving the Indian sub-continent and a compensating on-shore flow in the upper levels. Cold air from the north is trapped by the Himalayan mountain ranges preventing significant cooling on the Indian sub-continent and moderating the land-ocean temperature gradient. Relatively light winds, typically less than 7 m/s, result from this moderated thermal gradient. While not strong, this northeasterly flow can extend into the southern hemisphere due to differential heating between Saharan Africa and South Africa. It is during the Northeasterly monsoon that the UAE receives most of its precipitation from westerly systems that track south as troughs or depressions. On the rare occasion, strong frontal systems can track far enough

south to bring significant precipitation. Additionally, topographic forcing in the mountain ranges of eastern UAE and Oman enhance precipitation.

2. Southwesterly Monsoon (Summer)

As outlined in the Science Plan for the UAE2 campaign (Reid *et al.* 2004) and described in depth by the Forecaster's Handbook (NCMOF Bahrain 1999), the evolution of the Southwesterly Monsoon and beginning in the spring when differential heating between the ocean and the Tibetan Plateau causes a mid-level thermal low to form over the plateau. Latent heat is released as the result of cumulus convection as moist air is drawn into the low. This latent heat release warms the entire troposphere, increasing the layer thickness over land as compared to that over the ocean. The thickness differential results in a pressure gradient force in the upper levels that drives an off-shore flow at the upper levels.

In the lower levels, a compensating southwesterly on-shore flow develops as the Southwest monsoon. The intense insolation during the spring and continuing into the summer months develops a strong thermal low over Iran/Pakistan that eventually transitions into a thermal trough that extends from stretching from Somalia to Pakistan. The same Himalayan mountain ranges that prevent northern cold air from the reaching the Indian sub-continent during the winter Northeasterly monsoon also prevent the intrusion of relatively colder air during the summer months. Without the modifying influence of the northern cooler air, the thermal trough between Somalia and Pakistan further intensifies the monsoonal flow resulting in stronger on-shore flow in the summer than is seen in the off-shore flow in the winter.

A northwesterly flow is seen across the Arabian Peninsula during the Southwest monsoon due to the structure of the thermal trough (NCMOF Bahrain 1999). Periodically, intense wind storms, known as Shamals, are triggered and constitute an important mechanism in the mobilization of mineral aerosols. At the height of the Southwesterly monsoon, typically in August and September, the upper-level subsidence associated with the downward branch of the monsoonal flow located over Somalia and the Arabian peninsula causes ridging in the upper levels over the Arabian Peninsula and Iran and extremely dry conditions across the United Arab Emirates. Isolated convective

154

cells and associated precipitation can form in the vicinity of the mountains of eastern UAE; however, the effects are localized and bring little relief during the dry season. October and November bring the fall transition period and are marked by a slow flow reversal over a period of 30 to 45 days and a weakening of the northwesterly winds over the Arabian Peninsula (NCMOF Bahrain 1999).

3. Mesoscale Features of the UAE

The Science Plan for the UAE[2] campaign (Reid *et al.* 2004) described the mesoscale land-sea breeze complex that is superimposed on the synoptic Southwesterly monsoon flow along coastal UAE in the southern Arabian Gulf. The predominant northwesterly winds over the Arabian Peninsula tend to reinforce the sea breeze (~ 6 m/s) and oppose the southeasterly land breeze (~ 1-2 m/s). Winds aloft, typically above 700 mb, are dominated by the easterly trade winds south of UAE and westerlies to the north. August and September also mark the hottest time of the year with the highest air temperatures (> 40° C), the highest humidities (> 70%), and the highest sea-surface temperatures (> 33-37° C).

Also of interest during the campaign, Reid *et al.* (2004) discussed the formation and evolution for the boundary layer and internal boundary layers, an important process to the distribution of aerosol particles in the vicinity of UAE. Thermal Internal Boundary Layers (TIBL) form when warm dry air flows out over the relatively cooler water forming a stable layer in the lowest 100 to 300 meters. This combination of warm dry air over slightly cooler water results in a positive latent heat flux that moistens the air and a negative sensible heat flux that cools the air with relative humidities approaching 90%. Above this TIBL, a subsidence inversion is found in the upper levels down to 500 hPa with a well-mixed intermediate layer just below. The evolution of the strong stably stratified boundary layer with a strong subsidence inversion above serve to confine surface aerosol particles to the lowest levels unless ventilated into the mid-levels by the vertical circulations of the land-sea breeze complex.

4. Regional Aerosol Sources

According to Reid *et al.* (2004), airborne dust is the dominant aerosol particle type found throughout South West Asia and the Arabian Gulf region due to the plentiful sources in the region that include UAE, Iraq, Iran, Saudi Arabia, Qatar and Afghanistan. The dust of this region is generally composed of clays, alumina-silicates, and various evaporates, however, unique components such as ocean carbonates from deposits underlying the Arabian peninsula allow some discrimination between source regions. A constant level of background pollution can also be found across the region, composed largely of ammonium sulfate with smaller quantities of black carbon or particulate organic matter. Such a composition points to the petroleum industry, particularly flares and power plants, found throughout the Arabian Gulf as the predominant source for pollution in the region.

5. Weather Analyses for Study Days

a. *Northeast of MAARCO – Taweelah, UAE, 19 August 2004*

On August 19th, 2004, at 0600 UTC, the Arabian Gulf region was dominated by a well-established upper-level ridge of high pressure extending from Egypt across the Red Sea, the Arabian Peninsula, and into Iran in the northeast as depicted in NOGAPS analyses in Fig. 71. In the lower levels, an 850 mb low height center over the southern Arabian Gulf and Straits of Hormuz deepened over the preceding 24 hours as well as the formation of a low height centered over western Saudi Arabia and the Red Sea over the same time period. The flow pattern in the area of interest (MAARCO (24.7N-54.66E)/15 km NW of MAARCO) is generally west-southwest at 5-10 m/s along the coast as the transition from the weak land breeze to the stronger sea breeze reinforced by the northwesterly flow occurs over the next three hours.
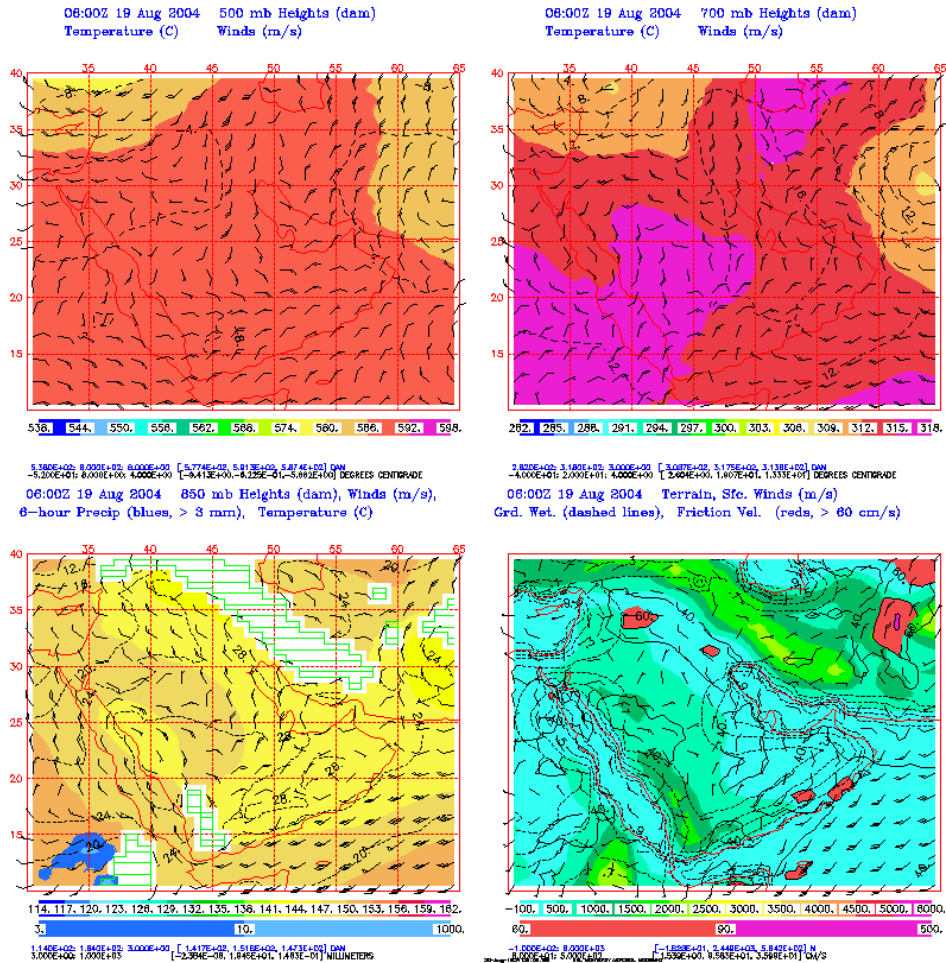
Figure 71.   NOGAPS 500 mb, 700 mb, 850 mb, and surface analyses for Southwest
              Asia valid 0600 UTC 19 August 2004 (courtesy of Naval Research
              Laboratory, Marine Meteorology Division, Monterey).

Figure 72 depicts the NAAPS plots for 0600 UTC and indicates that the dominant aerosol particles over the UAE were dust from Iraq and the UAE/Oman area with increased surface concentrations in eastern and south central Saudi Arabia. The NAAPS analyses also show that surface concentrations of smoke and pollution in the form of sulfates were at normal background concentrations or lower over the eastern UAE. The AERONET Level 2 data from the MAARCO site approximately 15 kilometers southwest of the area of interest measured an aerosol optical depth of 0.75 (at 500 nm) and an Angstrom exponent of 0.95 (440 nm/670 nm). In addition to the background aerosol particles, the image of the area of interest shows approximately 20% cloud cover. The presence of the clouds, in addition to the coastal location, suggest that

157

the aerosol particle size distributions measured at the MAARCO site could be modified by the addition of larger marine and/or hygroscopic growth of non-marine aerosol particles.
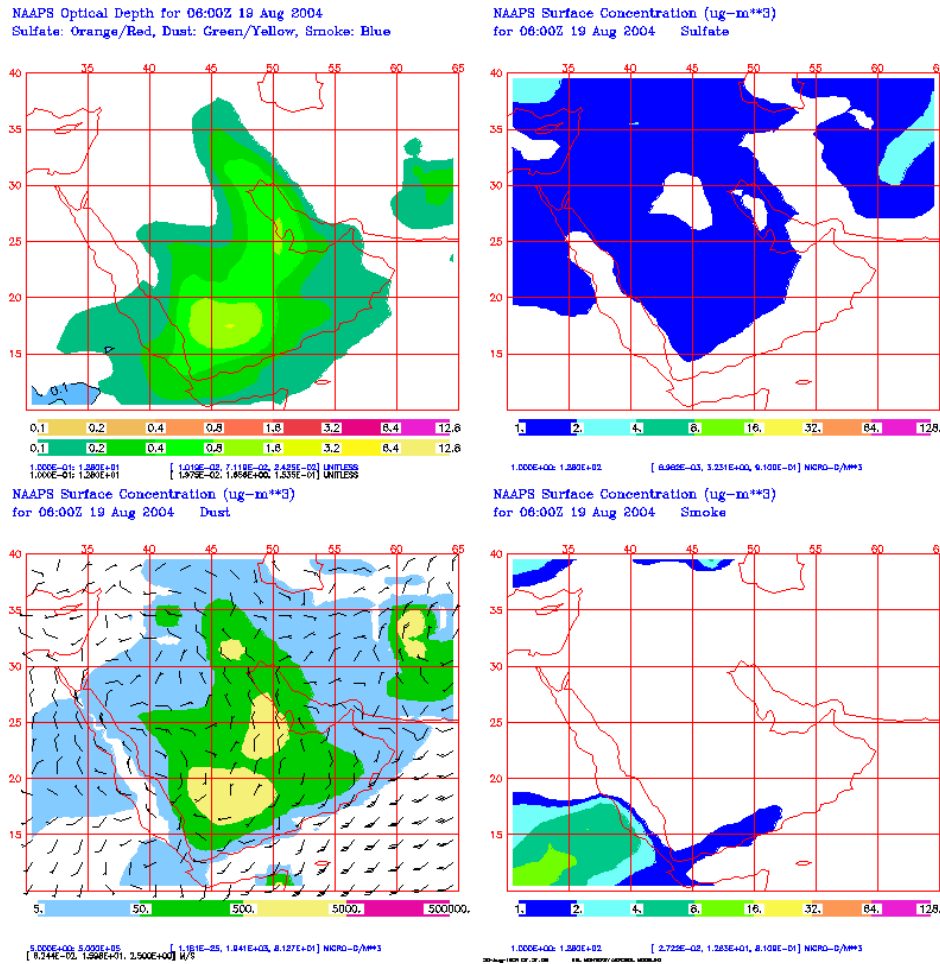
Figure 72.   NAAPS plots for Southwest Asia valid 0600 UTC, 19 August 2004 showing regional optical depth and surface concentrations of sulfates, dust, and smoke (courtesy of Naval Research Laboratory, Marine Meteorology Division, Monterey).

b.   *MAARCO – Northeast of Abu Dhabi, UAE, 16 September 2004*

On September 16th, 2004, at 0600 UTC, an upper-level trough located between the Black Sea and the Caspian Sea weakened the well-established upper-level ridge over the region as depicted in NOGAPS analyses in Fig. 73.   The ridge axis relocated to the Red Sea after a shift to the southwest. Troughing in the mid- and upper-levels reinforced a surface low over the central Arabian Gulf. The synoptic flow in the

area of interest (MAARCO) was generally west-southwest at 0-5 m/s along the coast. At 0655 UTC, the winds at the MAARCO site were west-southwesterly at 1.8 m/s indicating a weakening of the land breeze and the transition to the northwesterly sea breeze over the next three hours.
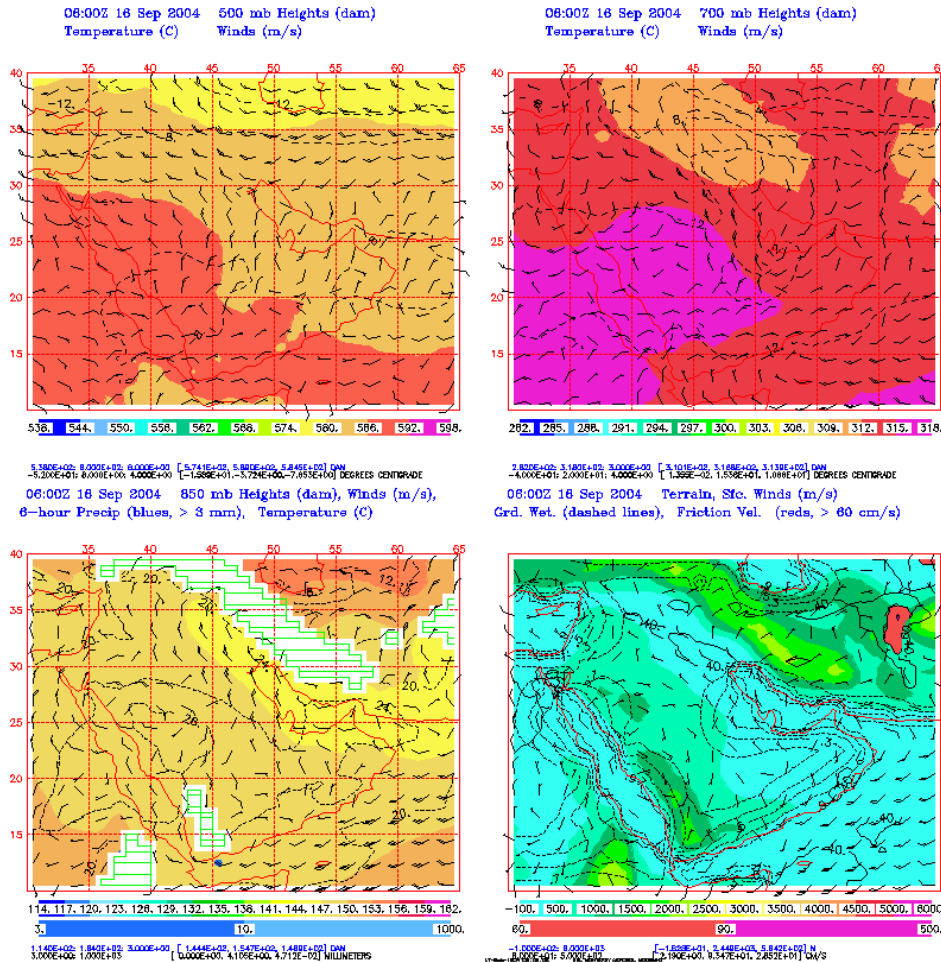

Figure 73.   NOGAPS 500 mb, 700 mb, 850 mb, and surface analyses for Southwest Asia valid 0600 UTC 16 September 2004 (courtesy of Naval Research Laboratory, Marine Meteorology Division, Monterey).

Figure 74 depicts the NAAPS analyses for 0600 UTC and indicates that the dominant aerosol particles over the UAE were dust from Iran and the northern Arabian Gulf as well as sulfates although the concentrations of both are relatively low. The NAAPS analyses also show that surface concentrations of smoke were low and pollution in the form of sulfates was at normal background concentrations or lower across the UAE. The AERONET Level 2 data from the MAARCO site show that an aerosol

159

optical depth of 0.26 (at 500 nm) and an Angstrom exponent of 0.62 (440 nm/670 nm). Although no clouds are present in the immediate vicinity, the coastal location suggests that the aerosol particle size distributions measured at the MAARCO could be influenced by the addition of larger marine aerosol particles and/or hygroscopic growth of non-marine aerosol particles.
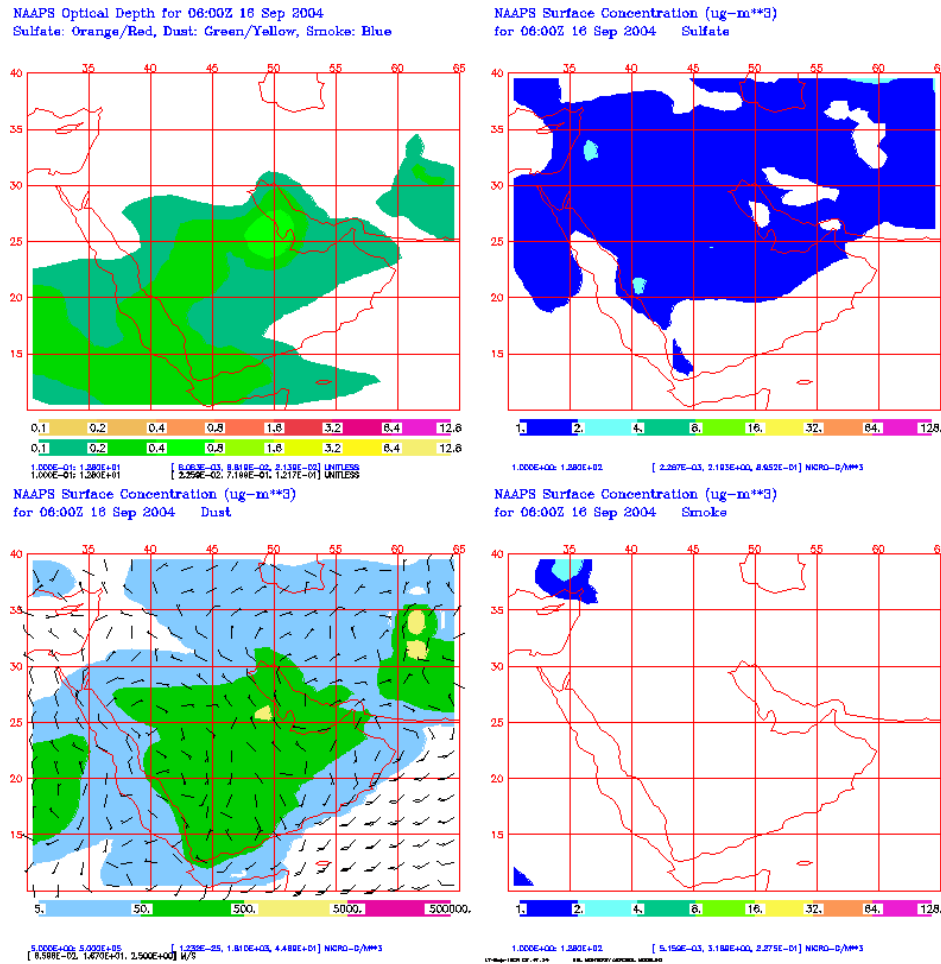
Figure 74.   NAAPS plots for Southwest Asia valid 0600 UTC, 16 September 2004 showing regional optical depth and surface concentrations of sulfates, dust, and smoke (courtesy of Naval Research Laboratory, Marine Meteorology Division, Monterey).

c.   MAARCO – Northeast of Abu Dhabi, UAE, 24 September 2004

On September 24th, 2004, at 0600 UTC, the Arabian Gulf region was dominated by an upper-level ridge extending from Egypt across the Red Sea, the Arabian Peninsula, and into Iran in the northeast as depicted in NOGAPS analyses in Fig. 75.   In

the lower levels, the ridge builds in at 700 mb. A surface low in the Gulf of Aden was apparent up to 700 mb. The synoptic flow in the area of interest (MAARCO) was generally west-southwest at 0-5 m/s along the coast. At 0655 UTC, the winds at the MAARCO site were west-southwesterly at approximately 3.5 m/s maintaining the strength of the land breeze. With the onset of the sea breeze, the winds become north-northwesterly.
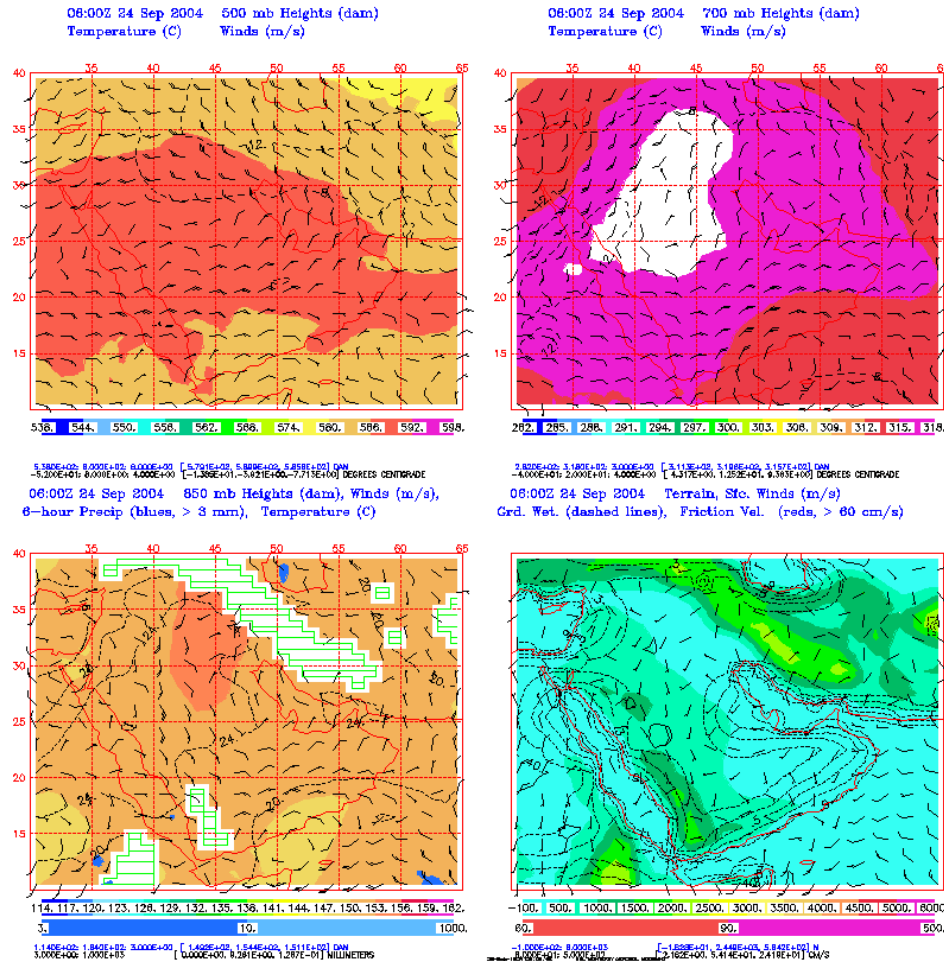
Figure 75.   NOGAPS 500 mb, 700 mb, 850 mb, and surface analyses for Southwest Asia valid 0600 UTC 24 September 2004 (courtesy of Naval Research Laboratory, Marine Meteorology Division, Monterey).

Figure 76 depicts the NAAPS analyses for 0600 UTC and indicates relatively low aerosol optical depths across the region. The NAAPS analyses also show that surface concentrations of smoke were very low and dust and pollution in the form of sulfates were at normal background concentrations or lower across the UAE. The

161

Microtops data from the MAARCO site show an aerosol optical depth of 0.46 (at 500 nm). Although no clouds are present in the immediate vicinity, the coastal location suggests that the aerosol particle size distributions measured at the MAARCO could be influenced by the addition of larger marine aerosol particles and/or hygroscopic growth of non-marine aerosol particles.
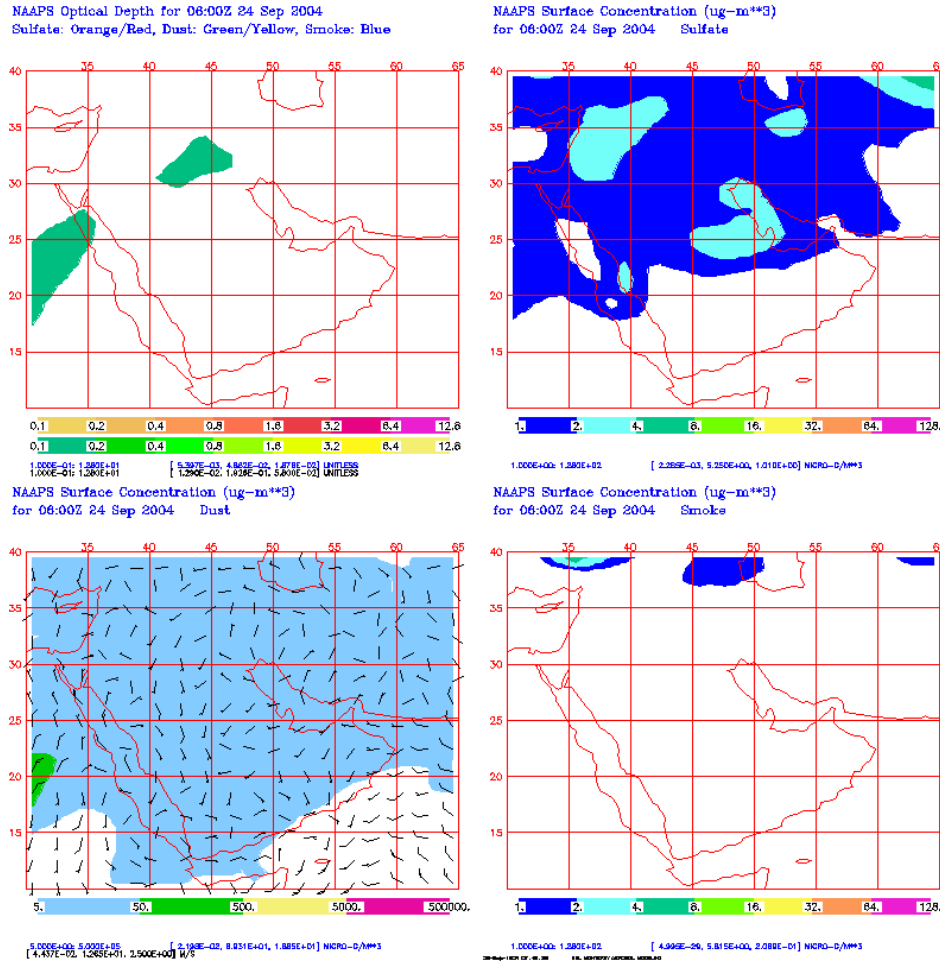

Figure 76.   NAAPS plots for Southwest Asia valid 0600 UTC, 24 September 2004 showing regional optical depth and surface concentrations of sulfates, dust, and smoke (courtesy of Naval Research Laboratory, Marine Meteorology Division, Monterey).

LIST OF REFERENCES

Abdou, W. A., D. J. Diner, J. V. Martonchik, C. J. Bruegge, R. A. Kahn, B. J. Gaitley, and K. A. Crean, 2005: Comparison of coincident Multiangle Imaging Spectroradiometer and Moderate Resolution Imaging Spectroradiometer aerosol optical depths over land and ocean scenes containing Aerosol Robotic Network sites. *J. Geophys. Res.*, **110**, D10S07, doi:10.1029/2004JD004693.

Ambartzumian, V. A., 1958: *Theoretical Astrophysics*. Pergamon, 645 pp.

Brown, B. B., 1997: Remote measurement of aerosol optical properties using NOAA POES AVHRR and GOES Imagery during TARFOX. M. S. Thesis, Department of Meteorology, Naval Postgraduate School, CA, 73 pp.

Cahalan, R. F., L. Oreopoulos, G. Wen, A. Marshak, S.-C. Tsay, and T. DeFelice, 2001: Cloud characterization and clear-sky correction from Landsat-7. *Rem. Sens. Environ.*, **78**, 83-98.

Charlson, R. J., S. E. Swartz, J. M. Hales, R. D. Cess, J. A. Coakley, Jr., J. E. Hansen and D. J. Hoffman, 1992: Climate forcing by anthropogenic aerosols. *Science*, **255**, 423-430.

DigitalGlobe, cited July 2005a: QuickBird technical specifications. [Available online at http://www.digitalglobe.com/about/quickbird.html.]

DigitalGlobe, cited July 2005b: QuickBird Imagery Products FAQ. [Available online at http://www.digitalglobe.com/downloads/QuickBird%20Imagery%20Products%20-%20FAQ.pdf.]

Durkee, P. A., K. E. Nielsen, P. J. Smith, P. B. Russell, B. Schmid, J. M. Livingston, B. N. Holben, C. Tomasi, V. Vitale, D. Collins, R. C. Flagan, J. H. Seinfeld, K. J. Noone, E. Ostrom, S. Gasso, D. Hegg, L. M. Russell, T. S. Bates, and P. K. Quinn, 2000: Region aerosol optical depth characteristics from satellite observations: ACE-1, TARFOX, and ACE-2 results. *Tellus,* **52**(**B**), 484-497.

Eck, T. F., 2005. Personal Communication.

Frolich, C., and G. E. Shaw, 1980: New determination of Rayleigh scattering in the terrestrial atmosphere. *Appl. Opt.*, **19**, 1773-1775.

Goddard Space Flight Center (GSFC), cited 2005: Aerosol robotic network (AERONET). [Available online at http://aeronet.gsfc.nasa.gov/.]

Henyey, L. C. and J. L. Greenstein, 1941: Diffuse radiation in the galaxy. Astrophys. J. **93**, 70-83.

Holben, B. N., T. F. Eck, I. Slutsker, D. Tanre, J. P. Buis, A. Setzer, E. Vermote, J. A. Reagan, Y. J. Kaufman, T. Nakajima, F. Lavenu, I. Jankowski, and A. Smirnov, 1998: AERONET – A federated instrument network and data archive for aerosol characterization. *Rem. Sens. Environ.*, **66**, 1-16.

Holekamp, K., 2003: NASA QuickBird radiometric characterization. *High Spatial Resolution Commercial Imagery Workshop*, Reston, VA. [Available online at http://www.esad.ssc.nasa.gov/vv/documents.]

Hsu, N. C., S. C. Tsay, M. D. King, and J. R. Herman, 2004: Aerosol properties over bright-reflecting source regions. *IEEE Trans. Geosci. Remote Sensing*, **42**, 557-569.

Intergovernmental Panel on Climate Change. *Climate Change 2001 – The Scientific Basis* (contribution of working group I to the Third Assessment Report of the Intergovernmental Panel on Climate Change). Cambridge University Press, Cambridge, 2001.

Kahn, R. A., B. J. Gaitley, J. V. Martonchik, D. J. Diner, and K. A. Crean, 2005: Multiangle Imaging Spectroradiometer (MISR) global aerosol optical depth validation based on 2 years of coincident Aerosol Robotic Network (AERONET) observations. *J. Geophys. Res.*, **110**, D10S04, doi:10.1029/2004JD004706.

Kaufman, Y. J. and R. S. Fraser, 1984: Atmospheric effect on classification of finite fields. *Rem. Sens. Env.*, **15**, 95-118.

Kaufman, Y. J., and J. H. Joseph, 1982: Determination of surface albedos and aerosol extinction characteristics from satellite imagery. *J. Geophys. Res.*, **87**, 1287-1299.

Kaufman, Y. J. and C. Sendra, 1988: Algorithm for automatic atmospheric corrections to visible and near-IR satellite imagery. *Int. J. Remote Sens.*, **9**, 1357-1381.

Kaufman, Y. J., D. Tanre, L. A. Remer, E. F. Vermote, A. Chu, and B. N. Holben, 1997a: Operational remote sensing of tropospheric aerosol over land from EOS moderate resolution imaging spectroradiometer. *J. Geophys. Res.*, **102**, 17051-17067.

Kaufman, Y. J., A. E. Wald, L. A. Remer, B.-C. Gao, R.-R. Li, and L. Flynn, 1997b: The MODIS 2.1-micrometer channel correlation with visible reflectance for use in remote sensing of aerosol. *IEEE Trans. Geosci. Remote Sens.*, **35**, 1286-1298.

Kidder, S. Q. and T. H. Vonder Haar, 1995: *Satellite Meteorology: An Introduction*. Academic Press, pp. 466.

Kiehl, J. T. and B. P. Briegleb, 1993: The relative roles of sulfate aerosols and greenhouse gases in climate forcing. *Science*, **260**, 311-314.

Koelemeijer, R. B. A., P. Stammes, J. W. Hovenier, and J. F. de Haan, 2002: Global distributions of effective cloud fraction and cloud top pressure derived from oxygen A band spectra measured by the Global Ozone Monitoring Experiment: Comparison with ISCCP data. *J. Geophys. Res.*, **107**, 4151, doi:10.1029/2001JD000840.

Kuciauskas, A. P., 2002: Aerosol optical depth analysis with NOAA GOES and POES in the Western Atlantic. M. S. thesis, Dept. of Meteorology, Naval Postgraduate School, Monterey, CA, 101 pp.

Liou, K. N., 2002: *An Introduction to Atmospheric Radiation*. Academic Press, pp. 583.

Martin, J. S., 2004: Aerosol optical depth model assessment with high resolution multiple angle sensors. M. S. thesis, Dept. of Meteorology, Naval Postgraduate School, Monterey, CA, 53 pp.

Mishchenko, M. I., L. D. Travis, R. A. Kahn, and R. A. West, 1997: Modeling phase functions for dustlike tropospheric aerosols using a shape mixture of randomly oriented polydisperse spheroids. *J. Geophys. Res.*, **102**, 16831-16847.

Motta, B., cited April 2006: Thin Cirrus Detection – November 25, 1997. [Available online at http://www.cira.colostate.edu/RAMM/PICODAY/112597.html]

Naval Central Meteorology and Oceanography Facility Bahrain (NCMOF Bahrain), 1999: *Area of Responsibility and Local Area Forecasters Handbook*. Naval Meteorology and Oceanography Command, Stennis Space Center, MS, 34 pp.

Odell, A. P. and J. A. Weinman, 1975: The effect of atmospheric haze on images of the earth's surface. *J. Geophys. Res.*, **80**, 5035-5040.

Pagnutti, M., R. E. Ryan, M. Kelly, K. Holekamp, V. Zanoni, K. Thome, and S. Schiller, 2003: Radiometric characterization of IKONOS multi-spectral imagery. *Rem. Sens. Env.*, **88**, 53-68.

Prather, M. J., 1996: Time scales in atmospheric chemistry: Theory, GWPs for CH4 and CO, and runaway growth. *Geophys. Res. Lett.*, **23**, 2597-2600.

Reid, J. S., 2005: Personal Communication.

Reid, J. S., C. Gatebe, B. N. Holben, M. King, S. Piketh, and D. L. Westphal, 2004: *Science Plan: United Arab Emirates Unified Aerosol Experiment (UAE^2)*. Naval Research Laboratory, Marine Meteorology Division, Monterey, CA, 89 pp.

Remer, L. A., Y. J. Kaufman, D. Tanre, S. Mattoo, D. A. Chu, J. V. Martins, R.-R. Li, C. Ichoku, R. C. Levy, R. G. Kleidman, T. F. Eck, E. Vermote, and B. N. Holben, 2005: The MODIS aerosol algorithm, products, and validation. *J. Atmos. Sci.*, **62**, 947-973.

Russell, P. B., J. M. Livingston, E. G. Dutton, 1993: Pinatubo and pre-Pinatubo optical depth spectra: Mauna Loa measurements, comparisons, inferred particle size distributions, radiative effects, and relationship to lidar data. *J. Geophys. Res.*, **98**, 22969-22985.

Smith, S. J., and T. M. L. Wigley, 2000: Global warming potentials: 1. Climatic implications of emissions reductions. *Climatic Change*, **44**, 445-457.

Tanre, D., M. Herman, and P. Y. Deschamps, 1981: Influence of the background contribution upon space measurements of ground reflectance. *Appl. Opt.*, **20**, 3676-3684.

Tanre, D., P. Y. Deschamps, C. Devaux, and M. Herman, 1988: Estimation of Saharan aerosol optical thickness from blurring effects in Thematic Mapper data. *J. Geophys. Res.*, **93**, 15955-15964.

Tanre, D. and M. Legrand, 1991: On the satellite retrieval of Saharan dust optical thickness over land: Two different approaches. *J. Geophys. Res.*, **96**, 5221-5227.

Taylor, J. R., 1997: *An Introduction to Error Analysis: The Study of Uncertainties in Physical Measurements*. University Science Books, pp. 327.

Thome, K, 2003: Vicarious calibration results for QuickBird-2. *High Spatial Resolution Commercial Imagery Workshop*, Reston, VA. [Available online at http://www.esad.ssc.nasa.gov/vv/documents]

Twomey, S. A., M. Piepgrass, and T. L. Wolfe, 1984: An assessment of the impact of pollution on the global albedo. *Tellus,* **36(B)**, 356-366.

Wang, J., X. Liu, S. A. Christopher, J. S. Reid, E. Reid, and H. Maring, 2003: The effects of non-sphericity on geostationary satellite retrievals of dust aerosols. *Geophys. Res. Lett*., **30**, 2293, doi:10.1029/2003GL018697.

Wen, G., R. F. Cahalan, S.-C. Tsay, and L. Oreopoulos, 2001: Impact of cumulus cloud spacing on Landsat atmospheric correction and aerosol retrieval. *J. Geophys. Res.*, **106**, 12129-12138.

Xiang-Ao, Xia, H. Chen, P. Wang, X. Zong, J. Qui, and P. Gouloub, 2005: Aerosol properties and their spatial and temporal variations over North China in spring 2001. *Tellus,* **57(B)**, 28-39.

Wehrli, C., 1985: *Extraterrestrial Solar Spectrum - Publ. 615.* Physical Meterological Observatory and World Radiation Center, Davos Dorf, Switzerland.

Young, A. T., 1980: Revised depolarization corrections for atmospheric extinction. *Appl. Opt.*, **19**, 3427-3428.

THIS PAGE INTENTIONALLY LEFT BLANK

INITIAL DISTRIBUTION LIST

1. Defense Technical Information Center
    Ft. Belvoir, Virginia

2. Dudley Knox Library
    Naval Postgraduate School
    Monterey, California

3. Chairman, Code MR
    Department of Meteorology
    Naval Postgraduate School
    Monterey, California

4. Professor Philip A. Durkee (Code MR/DE)
    Department of Meteorology
    Naval Postgraduate School
    Monterey, California

5. Professor Carlisle H. Wash (Code MR/WX)
    Department of Meteorology
    Naval Postgraduate School
    Monterey, California

6. LCDR Dominick A. Vincent
    Department of Meteorology
    Naval Postgraduate School
    Monterey, California